AI-Designed Protein Binders Tackle a Century-Old Challenge: Tc24 as a Universal Vaccine Antigen for Chagas Disease

Thesis submitted to the University of Nottingham in part fulfilment

for the degree of Masters of Research

June 2025

Alicia Richardson, BSc

School of Biosciences

University of Nottingham

Supervisors:

Dr Ivan Campeotto – University of Nottingham

Professor Stephen Harding – University of Nottingham

Word count: 6981

Abstract

Chagas disease, caused by the protozoan parasite *Trypanosoma cruzi*, remains one of the most neglected tropical diseases, disproportionately affecting low-income, rural populations across Latin America. Despite over a century since its discovery, there is still no effective vaccine and therapies currently rely on the usage of nifurtimox and benznidazole, which have been linked to severe side effects. This review explores the multifaceted challenges of developing both a therapeutic and prophylactic treatment for Chagas disease. Particular attention is given to the flagellar calcium-binding protein Tc24, a highly conserved, immunogen expressed across all morphological stages of *T. cruzi*.

In parallel, this review examines how artificial intelligence (AI) and deep learning (DL) platforms are revolutionising structural prediction and binder design. These technologies enable the in silico development of both high-affinity and target-specific binders at low cost.

In summary, this review proposes the integration of conserved antigen targets, with AI-guided binder design presents a novel framework for overcoming current barriers in vaccine development, offering renewed hope for the prevention and management of Chagas disease.

Table of Contents

1. Introduction

Identified in 1909 by Carlos Ribeiro Justiniano Chagas, *Trypanosoma cruzi* is a hemoflagellate protozoan parasite responsible for Chagas disease (Chagas, 1909). This devastating and often life-threatening disease is endemic to 21 Latin American countries. It is particularly prevalent in low-income, rural areas; where inadequate housing conditions facilitate the colonisation of the parasitic vector, the triatomine bug. Alarmingly, due to increasing global migration, cases of Chagas disease are now being reported more frequently in non-endemic regions, including parts of North America and Europe.

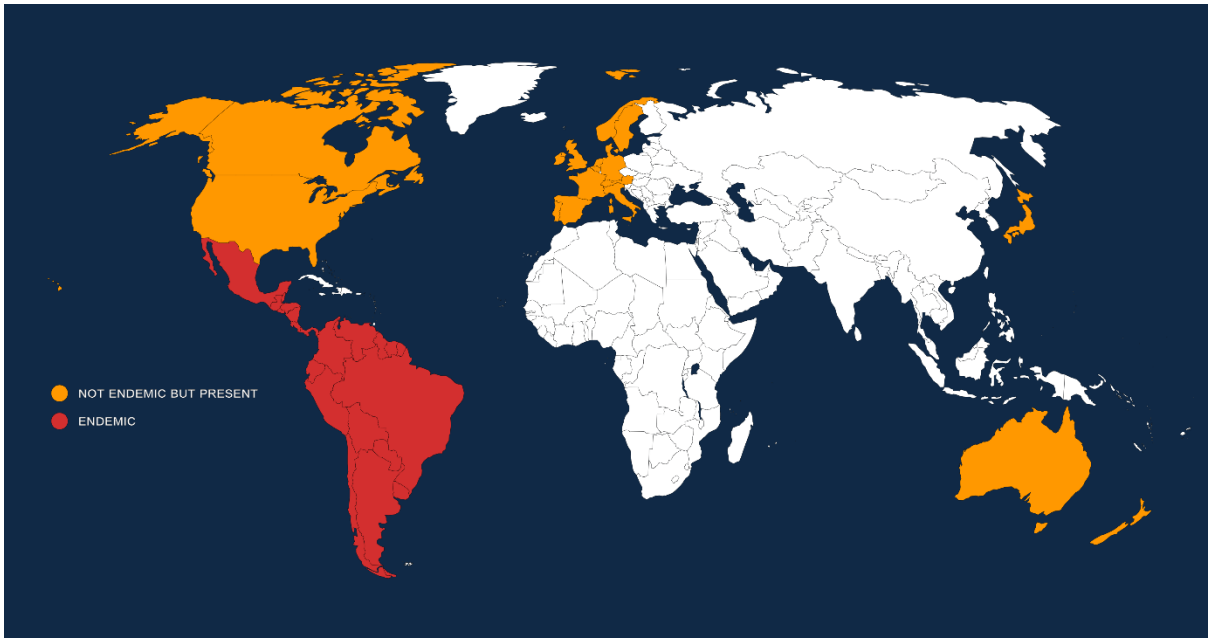

Figure 1. Global distribution of Chagas Disease. Adapted from (DNDi, 2025)

With an estimated 6 – 8 million people affected, 30,000 new infections and 12,000 deaths reported annually (PAHO, 2025), this neglected disease poses significant health concerns. The World Health Organisation (WHO) has classified Chagas disease as the most prevalent poverty-related neglected tropical disease. In response to this public health crisis, the Pan American Health Organisation (PAHO) has included Chagas disease in its *Diseases Elimination Initiative,* which aims to accelerate the elimination of over 30 communicable diseases in the Americas by 2030 (PAHO, 2023).

However, despite such international recognition, Chagas disease remains critically underdiagnosed and undertreated. The non-specificity of symptoms during the early stages of infection, coupled with limited access to healthcare, leaves many infected individuals unaware of their condition; estimates suggest that only a mere 10% know they have been infected, revealing a shocking gap in both diagnosis and public awareness (Lopez-Albizu et al., 2023). As a result, most cases are only identified during the chronic phase; by this time, irreversible cardiac and/or gastrointestinal damage may have occurred.

Furthermore, treatment options remain woefully inadequate, relying solely on two drugs, benznidazole and nifurtimox, both of which are most effective during the acute phase and are associated with severe side effects (Bern, 2011). The lack of safe and effective therapies for chronic Chagas disease, combined with diagnostic limitations and the expanding global distribution of *T. cruzi*, underscores the urgent need for improved preventative and therapeutic treatments. These shortcomings in diagnostic and therapeutic treatments highlight the urgent need for a vaccine that provides both prophylactic and therapeutic benefits.

This review delves into key challenges that have impeded vaccine development for *T. cruzi*. It highlights the parasite's intricate immune evasion mechanisms while evaluating the most promising vaccine candidates, including highly conserved antigens such as Tc24 (Villanueva-Lizama et al., 2018). Additionally, this review introduces a groundbreaking technological advancement in vaccine development: AI-assisted binder design. This innovative approach enables the development of highly specific, computationally engineered protein binders, aimed at improving antigen targeting.

This review asks whether the conserved flagellar antigen Tc24, paired with de-novo-designed binders, can overcome factors such as DTU diversity and immune evasion to achieve lineage-wide protection

2. Background

2.1. Lifecycle and Transmission

Infection of a mammalian host with *Trypanosoma cruzi* begins when an infected triatomine bug feeds on the blood of its host. This parasitic transmission can occur through both domestic and sylvatic cycles (*Figure 2)*.

In the sylvatic cycle, the parasite exists amongst a wide range of wild mammals. These animals act as reservoir hosts, sustaining *T. cruzi* amongst wild animal populations. Occasionally, sylvatic triatomine bugs may encounter humans, resulting in spillover infections. This typically occurs when humans enter forested areas for activities such as farming or hunting, though this route of transmission is less common than domestic transmission.

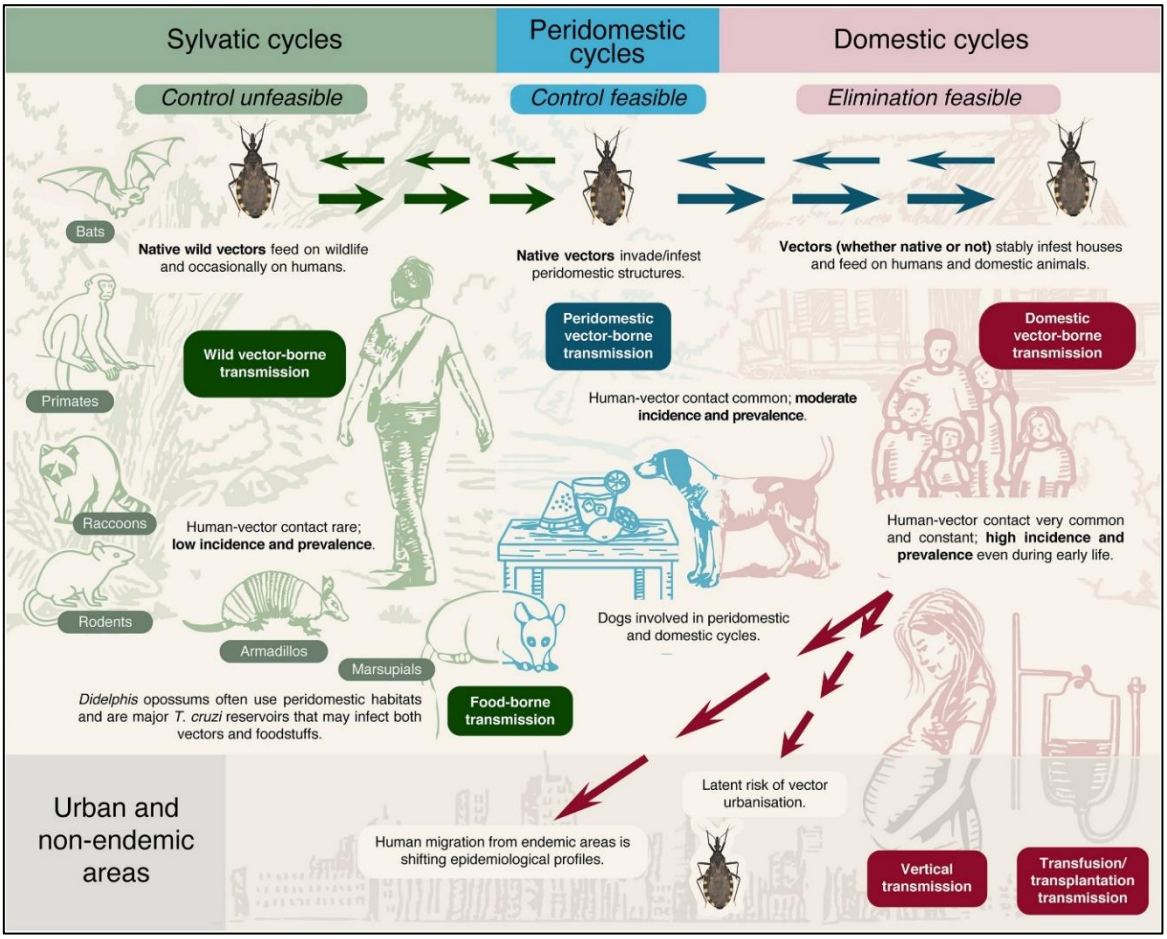

Figure 2 . Transmission routes of *Trypanosoma cruzi* across sylvatic, peridomestic and domestic cycles (Cucunubá et al., 2024)

The more common mechanism of human infection occurs through the domestic cycle, in which triatomine bugs inhabit human dwellings. After feeding on infected domestic animals, they can then transmit *Trypanosoma cruzi* to humans. During or shortly after feeding, the bug defecates near the site of the wound, releasing excreta containing infective metacyclic trypomastigotes (*Figure 3, Stage 1*) These trypomastigotes are introduced into the host through either mucosal membranes or via skin abrasions when the host scratches the irritated wound site. Once in the bloodstream, the trypomastigotes, characterised by a long motile flagellum, propel the parasite towards both phagocytic and non-phagocytic nucleated cells.

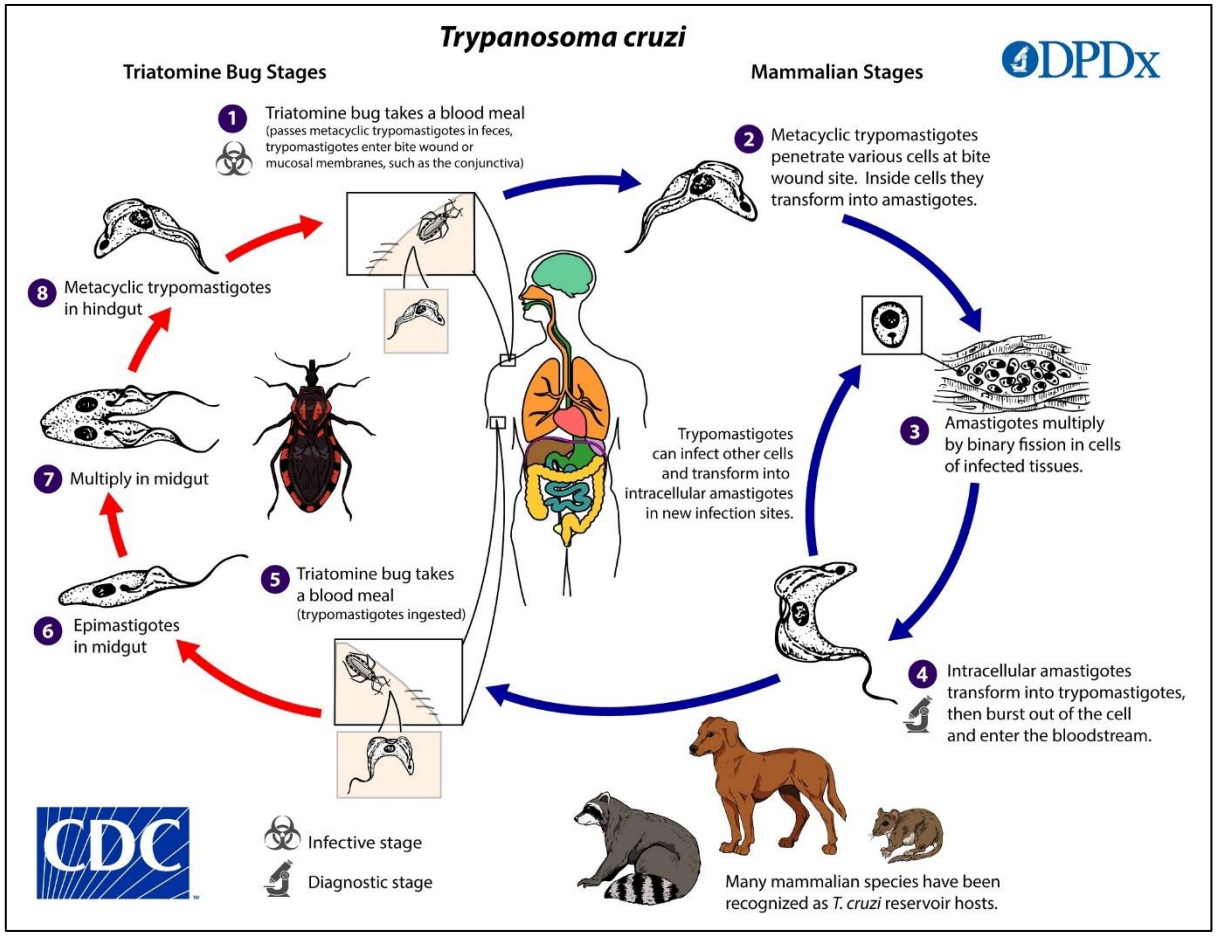

Figure 3. A complete overview of the *T. cruzi* transmission cycle from vector to humans. *Image source: CDC, DPDx, (2021).*

Depending on the host cell type, the parasite can be internalised through phagocytosis or active invasion. Host cell recognition and adhesion are mediated by the parasite's Gp35/50 mucins, a

family of highly sialylated surface glycoproteins. These mucins bind specifically to Annexin A2 receptors on non-immune host cell membranes, facilitating adhesion to the cell surface and enabling active invasion (Onofre et al., 2022, Teixeira et al., 2015, Barrias et al., 2019). Once inside the host cell, a parasitophorous vacuole (PV) forms around the trypomastigote. Inside the vacuole, the trypomastigote begins to differentiate into smaller, rounder, intracellular amastigotes which rupture and escape the PV into the host cell cytoplasm.

The amastigotes replicate via binary fission, often occupying the entire cytoplasm of the host cell (*Figure 3, Stage 3*). Following division, the amastigotes transform into bloodstream trypomastigotes. These highly motile forms, display intense and constant movement while lysing the host cell membrane. The intracellular replicative cycle takes 3–5 days to complete and culminates in the trypomastigotes bursting out of the host cell into the extracellular space (*Stage 4*), where they can invade new cells or be taken up by a feeding triatomine bug (*Stage 5*) (Martín-Escolano et al., 2022). *Figure 4* provides a detailed view of the intracellular steps of host cell invasion and replication by *T. cruzi*, expanding on the mammalian stages illustrated in *Figure 3, Stages*

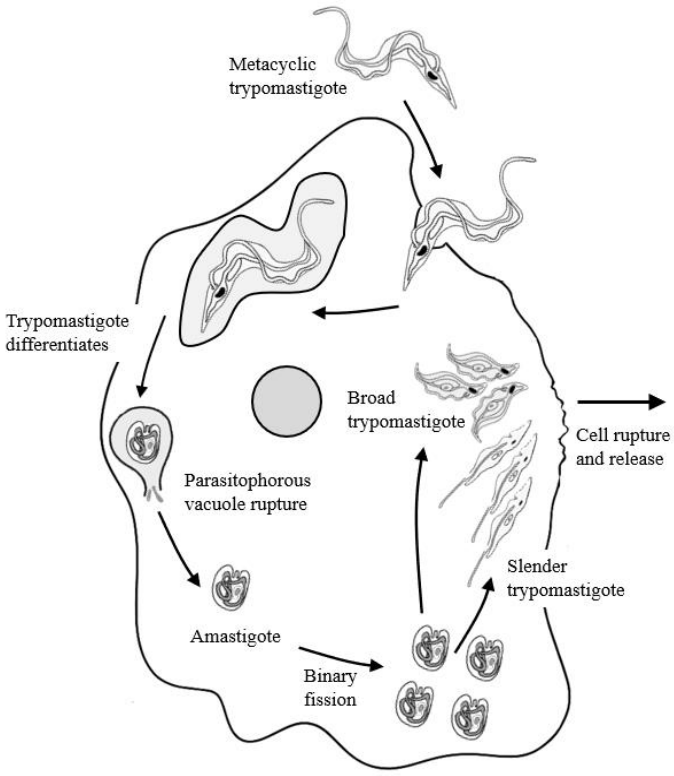

Figure 4. Host cell invasion and intracellular development of *Trypanosoma cruzi*. *Figure drawn by the author.*

Within the triatomine's midgut, the ingested trypomastigotes transform into epimastigotes (*Stage 6*). These proliferate and migrate towards the hindgut (*Stage 7*), where they undergo metacyclogenesis back into infective metacyclic trypomastigotes (*Stage 8*).

2.2. Pathogenesis and Disease Progression

Chagas disease is classed into two clinical stages: acute and chronic. During the initial acute stage of infection, many patients, despite exhibiting patent parasitaemia, are often asymptomatic. At this stage, parasitological tests can detect the parasite, and individuals are typically more responsive to treatment (Ávila-Santos et al., 2025). However, because symptoms are mild or absent, most remain unaware they are infected. One of the few recognisable clinical signs, although rarely reported during the acute phase (PAHO, 2025) is Romaña's sign *Figure 5.* This is a painless, unilateral periorbital swelling that occurs when faeces from an infected triatomine are rubbed into the conjunctival mucosa.

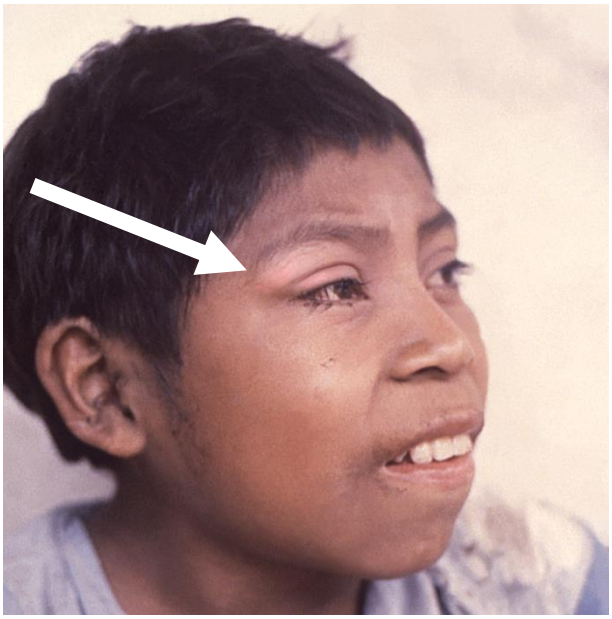

Figure 5. A young child suffering from Chagas disease and presenting with Romaña's sign (indicated by arrow) a clinical indication of an acute stage *Trypanosoma cruzi* infection. (Image source: Melvin, 1962; CDC Public Health Image Library, Image ID 15815)

If left untreated, the disease gradually progresses to the indeterminate chronic stage, typically 4 – 8 weeks post initial infection (Bern, 2011). Characterised by positive serological tests for anti – *T. cruzi* antibodies and the absence of clinical symptoms, this stage can persist indefinitely.

However, in 30 – 40% of cases, patients progress to the determinate chronic stage after 10 – 30 years, where severe cardiac or gastrointestinal symptoms begin to manifest (PAHO, 2025).

Over time, chronic inflammation and tissue damage are triggered as the parasite invades host cell tissues. This can lead to serious complications, such as cardiomyopathy, the most common and life-threatening manifestation of chronic Chagas disease (Laranja et al., 1956). At this stage, therapeutic efficacy is significantly reduced .

Despite the importance of early diagnosis for effective treatment and disease control, access to healthcare remains a challenge in low-income environments. This is due to a limited availability of reliable diagnostic tools and a shortage of trained healthcare professionals, all of soma

Exaggerating these challenges is the lack of an effective vaccine for *T. cruzi*. Treatment options are currently limited to two drugs, benznidazole and nifurtimox. While these drugs are most effective during the acute phase, they are also associated with severe side effects (Laboratorios Liconsa, S.A, 2021; Bayer HealthCare Pharmaceuticals Inc., 2023; Torrico et al., 2021). This further emphasises the urgency for improved diagnostic tools and the development of vaccines that are both prophylactic and therapeutic.

3. *T. cruzi* genetic diversity and geographical distribution

3.1. Genetic diversity

The development of vaccines for *Trypanosoma cruzi* has been complicated by its genomic plasticity. To better characterise the diversity of *T. cruzi,* strains have been categorised into discrete typing units (DTUs). These are identified as genetically distinct evolutionary lineages, based on a combination of common molecular markers: mini-exon, 24Sα rRNA, cytochrome B (Brisse et al., 2001). While no single marker serves as a "gold-standard" approach for distinguishing DTUs, a multilocus approach has been widely regarded as the most reliable method (Schijman, 2018).

As of 2025, six genetically distinct discrete typing units (DTUs) have been identified, all of which are known to infect humans (TcI—TcVI). A seventh DTU, (TcBat) has been discovered, which predominantly exists in bat lifecycles (Marcili et al., 2009). Although in literature, TcBat isn't widely recognised as a human-infective lineage, a single case involving a 5-year-old child in northwestern Colombia has been documented by Ramírez et al. (2014).

Phylogenetic analysis based on cytochrome B sequences (*Figure 6)* constructed as part of this review, indicate that TcBat is most closely related to TcI. This close evolutionary relationship may suggest that human TcBat infections are underreported or misidentified as TcI due to their genetic similarity. Moreover, the phylogenetic tree also reveals that TcIII, TcV, and TcVI are closely related. This aligns with reports suggesting that TcV and TcVI are hybrid lineages which have formed from a mix of TcII and TcIII ancestors (Lewis et al., 2011).

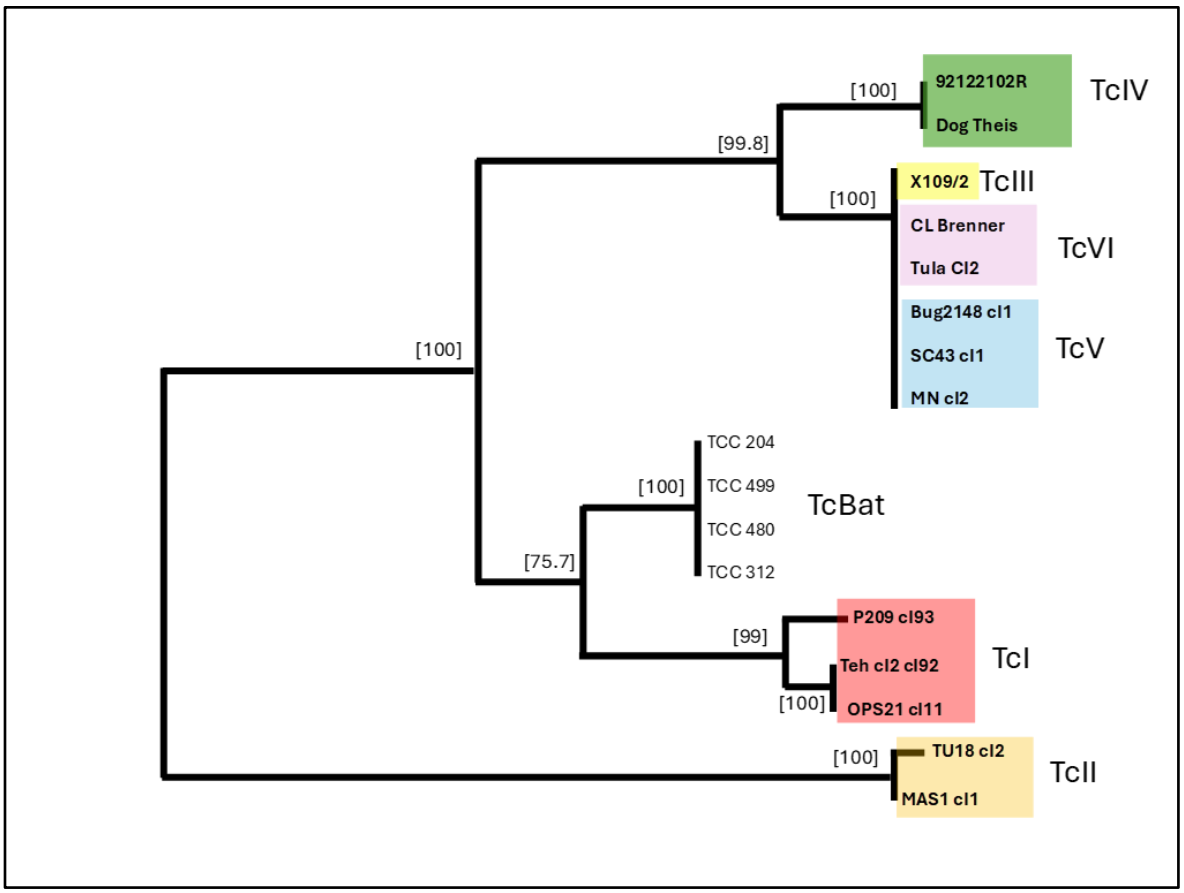

Figure 6. Phylogenetic tree of *Trypanosoma cruzi* based on cytochrome B sequences from 17 isolates (TcI – TcVI, and TcBat).

The tree was constructed using the ETE3 phylogenetic analysis pipeline (Huerta-Cepas et al., 2016). The tree is midpoint-rooted, and isolates are colour-coded by DTU. TcI (red), TcII (orange), TcIII (yellow), TcIV (green), TcV (blue), TcVI (pink), and TcBat (black text). Full metadata and GenBank accession numbers for all strains are listed in *Appendix I*.

The genetic diversity observed among the different DTUs is not solely taxonomic, as each DTU exhibits different transmission routes and varying severity of clinical symptoms. *T. cruzi* DTUs TcIII and TcIV predominantly circulate within the sylvatic transmission cycle and are most frequently reported in cases of acute Chagas disease (Freitas, 2023; Zingales et al., 2012)

In contrast, TcII, TcV, and TcVI are largely linked to domestic transmission cycles and chronic Chagas disease, often manifesting as cardiomyopathy and digestive megasyndromes such as megaoesophagus and megacolon (Messenger et al., 2015). Notably, TcI stands out as the most widespread and genetically diverse DTU, participating in both sylvatic and domestic cycles

throughout the Americas. It is predominantly associated with chronic cardiac Chagas disease, particularly chagasic cardiomyopathy, although it is rarely connected to digestive manifestations (Ramírez et al., 2010).

Ongoing efforts to sequence diverse strains of *T. cruzi* and establish a link between genotype and the most severe clinical manifestations will help to inform vaccine design strategies aimed at targeting conserved, immunogenic antigens present across multiple DTUs. However, a significant challenge arises from the low levels of peripheral parasitaemia seen in chronic infections.

3.2. Geographical distribution

A study conducted by Brenière et al. (2016), aimed to generate an inventory of all *T. cruzi* strains reported within current literature and classify them according to their DTU. As part of this review, the compiled dataset was filtered to include only isolates derived from *Homo sapiens*. A reference map showing the regional classification of the Americas used in this analysis is provided in *Figure 8.*

Figure 7. Regional Classification of the Americas . The map depicts five eco-epidemiological regions: Southern Cone (green), Northern South America (red), Central America (yellow), Caribbean (orange), and Northern America (blue).

The distribution of those isolates were mapped across the Americas as illustrated in *Figure 8***Figure 8**. A total of 1,848 human isolates were included, with the majority belonging to TcV (n = 656) and TcI (n = 597), followed by TcII (n = 377), TcVI (n = 75), TcIV (n = 114), and TcIII (n = 29). The resulting distribution map was generated using Datawrapper GmbH, (2025), providing a clear visual representation of regional variation in DTU prevalence.

These distribution maps highlight the broad spread of *T. cruzi* DTU strains across the Americas, with TcI and TcII being the most prevalent. Distinct geographic patterns can be observed for each of the DTUs, TcV and TcVI are more prevalent in the Southern Cone, while TcIII is more region-specific to Brazil.

Notably, the highest levels of DTU diversity were observed in the Southern Cone, particularly in Argentina and Bolivia, where TcI, TcII, TcV, and TcVI frequently co-circulate. It is important to note that these maps represent the number of genetically typed *T. cruzi* strains isolated from humans rather than reported clinical cases. As such distribution of DTUs may be influenced by sampling bias due to overrepresentation of certain regions.

Nevertheless, these patterns offer valuable insights for developing region-specific vaccines and for understanding the ecological and epidemiological factors that contribute to high genetic diversity in certain areas. Additionally, DTU diversity and geographical distributions are key considerations in vaccine development, as antigenic variability can compromise treatment efficacy.

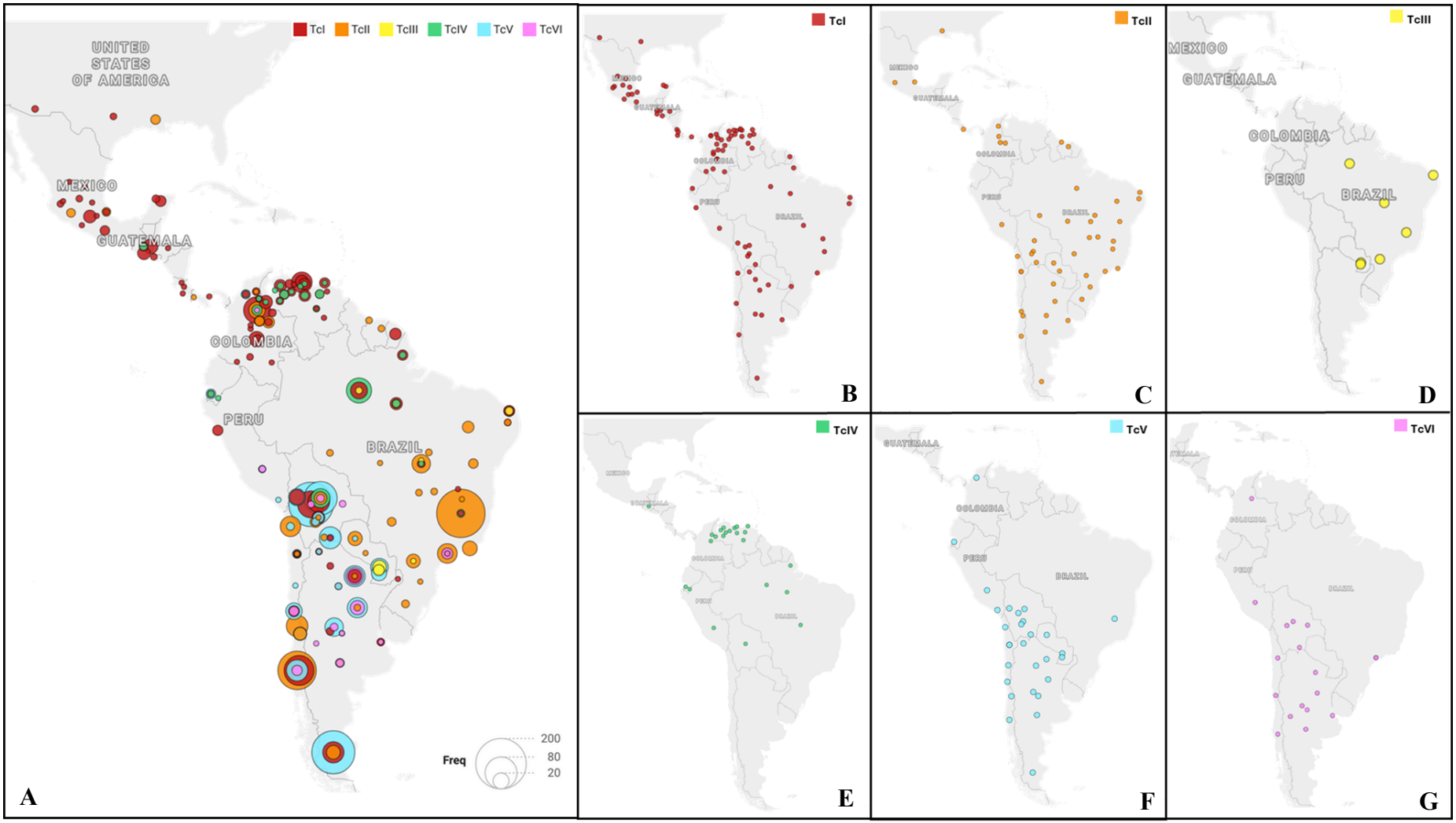

Figure 8. Geographic distribution and frequency of human-infective *Trypanosoma cruzi* discrete typing units (DTUs) across the Americas. (A) Composite map showing all DTUs, with circle size scaled to the frequency of *T. cruzi* strains reported from human isolates at each location. **(B–G)** Showing the geographic distribution of individual DTUs: TcI **(B)**, TcII **(C)**, TcIII **(D)**, TcIV **(E)**, TcV **(F)**, and TcVI **(G)**. Each dot represents at least one *T. cruzi* strain identified in a human isolate at that site. TcI (red) and TcII (orange), are broadly distributed across South America and Central America, while hybrid DTUs TcV (cyan) and TcVI (magenta) are concentrated in the Southern Cone. TcIII (yellow) shows more restricted, region-specific distributions primarily in Brazil, and TcIV (green) is concentrated more in northern South America. Maps were created using Datawrapper (https://app.datawrapper.de).

4. Current Diagnostics and Treatments

4.1. Acute Phase Diagnosis

The acute phase of Chagas disease is characterised by high levels of parasitaemia and is often asymptomatic. Diagnosis at this stage primarily relies on parasitological methods, which allow for direct observation of *Trypanosoma cruzi* trypomastigotes in peripheral blood samples (Ballesteros-Rodea et al., 2018).

These samples are typically stained using Giemsa staining techniques and visualised under a microscope (Krafts et al., 2011). However, when parasitaemia levels are low the Strout technique is often employed (Strout, 1962). This involves allowing a blood sample to coagulate and pelleting the sample. The resulting pellet is then examined under a microscope to confirm the presence of the parasite. This method is particularly useful during the later stages of the acute phase, when parasitaemia is beginning to decline but remains within the detectable range. However, it becomes ineffective in the indeterminate chronic stage, where parasite levels are typically too low for direct detection.

Characteristic features of the trypomastigote which aid in identification are its distinct kinetoplast, a C- or S-shaped body and a fin-like undulating membrane, which extends along the length of the parasite to its flagellum, as illustrated by the Giemsa-stained preparation in *Figure 9.*

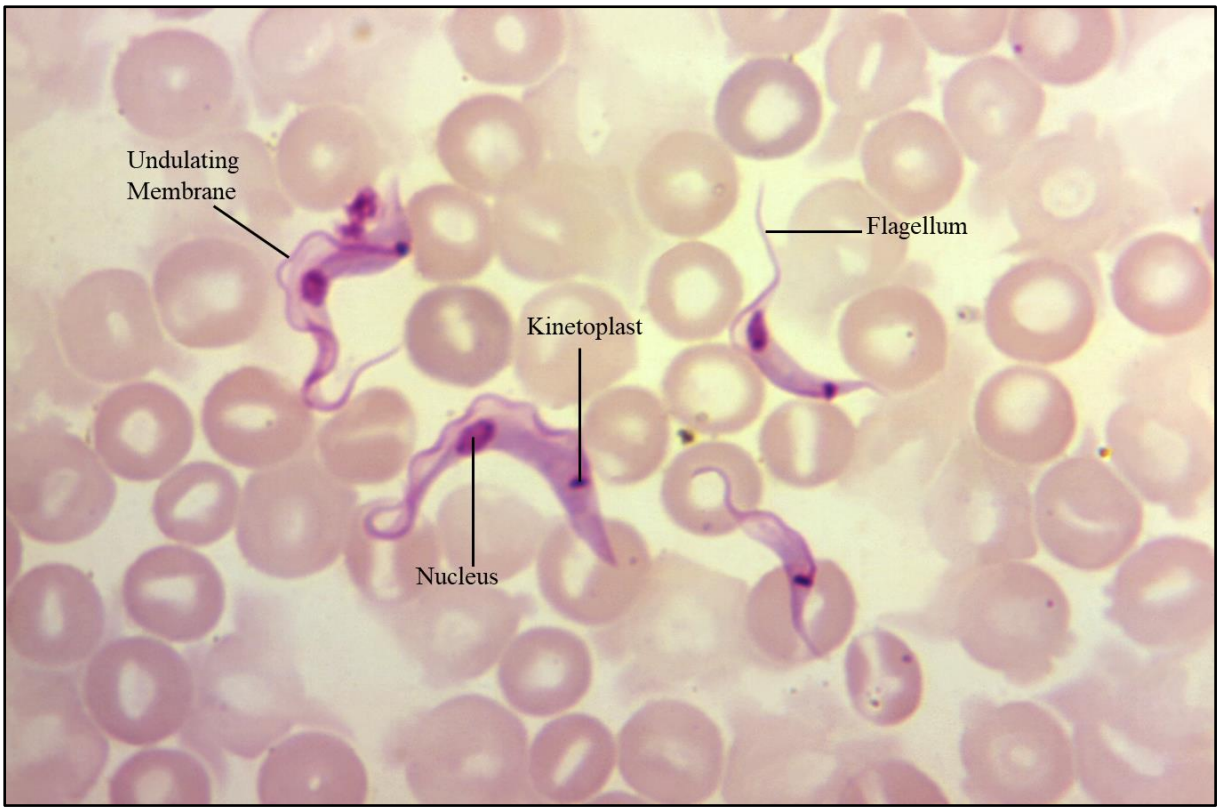

Figure 9: Four *Trypanosoma cruzi* trypomastigotes in a Giemsa stained blood smear. The image illustrates key morphological features including the nucleus, kinetoplast, undulating membrane, and anterior flagellum. Adapted from CDC Public Health Image Library, Image: 21029 (1968)

While these features are indicative of *T. cruzi*, they are also shared by another *Trypanosoma* species, *T. rangeli,* an entirely non-pathogenic parasite which is co-endemic with *T. cruzi.* These morphological similarities often make it difficult, even for a trained professional, to reliably distinguish between the two parasites. This challenge is well illustrated in comparative images presented in the study by Oliveira et al. (2017) and given these limitations, microscopic observation alone is insufficient for reliable diagnosis of Chagas disease and often needs to be supplemented with molecular methods such as PCR (Afonso et al., 2012).

4.2. Chronic Phase Diagnosis

In the chronic stage of Chagas disease, diagnosis becomes increasingly challenging due to low and intermittent levels of circulating parasites. Diagnosis typically relies on serological tests to detect anti-*T. cruzi* IgG antibodies. While these antibodies confirm prior exposure to *T. cruzi*,

they do not indicate when the infection occurred as IgG levels can remain elevated for several years. This presents challenges in diagnosing congenital cases, maternal IgG antibodies can cross the placenta and persist in the infant's circulation for up to 9 months, potentially leading to a false-positive diagnosis (Bern et al., 2019).

For diagnosis Chagas in chronic cases, the CDC, (2023) advises that two distinct serological assays be used to confirm infection due to the antigenic variability of *T. cruzi*. Commonly used assays include: enzyme-linked immunosorbent assay (ELISA), indirect immunofluorescence assay (IFA), and indirect haemagglutination assay (IHA) (Alonso-Padilla et al., 2020). This dual-testing strategy helps to mitigate false positives, particularly in endemic regions where *T. rangeli* is also prevalent (Ballesteros-Rodea et al., 2018).

While these immunoassays are theoretically affordable (Ascanio et al., 2024), they remain underused in endemic regions due to several financial challenges. These include limited laboratory infrastructure, trained personnel, inadequate refrigeration and a lack of sample transport logistics, which are often lacking in Chagas-endemic countries.

4.3. Treatment Options

4.3.1. Mechanism of Action

Treatment for Chagas disease is currently limited to two nitroheterocyclic drugs: nifurtimox (NFX), launched in 1967 by Bayer (*Lampit®)* followed by benznidazole (BZN) in 1972 by Roche (*Rochagan®/ Radanil®*) *Figure 10*. Both treatments act as prodrugs that require bioactivation to exert their trypanocidal effects. Despite the introduction of these drugs more than 50 years ago, the development of alternative treatments has progressed slowly.

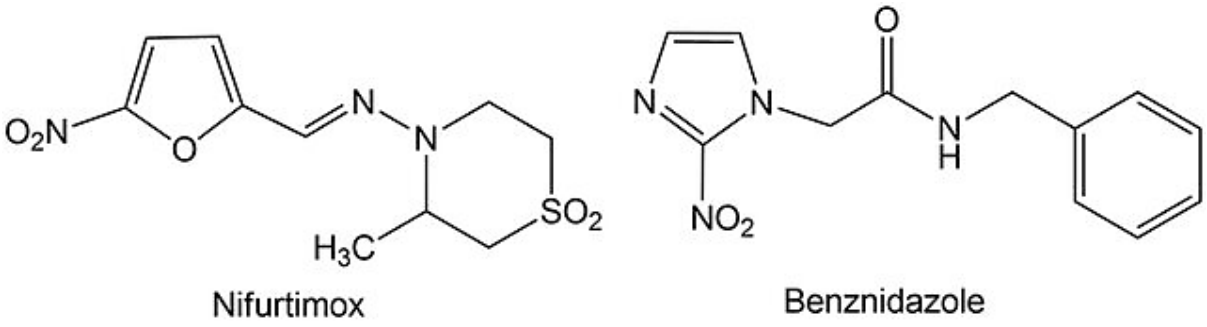

Figure 10. Chemical structures of nifurtimox (NFX) and benznidazole (BZN), the two nitroheterocyclic drugs currently used in the treatment of Chagas disease.

Benznidazole (BZN) is a nitroimidazole compound that is activated within *T. cruzi* by trypanosomal type I nitroreductase (TcNTR), an enzyme in most protozoan parasites, although absent in humans. The TcNTR reduces the nitro group of BZN to form reactive intermediates (Hall & Wilkinson, 2012), which are unstable and form covalent adducts with nucleic acids and proteins causing cellular damage and ultimately parasite death (Rajão et al., 2014; Laboratorios Liconsa S.A., 2021).

Nifurtimox (NFX), is a nitrofuran derivative which similarly undergoes nitroreductase-mediated activation, within *T. cruzi*. The reduction of NFX leads to the formation of superoxide radicals (O_2^-) and hydrogen peroxide (H_2O_2), which induce extensive oxidative damage to the parasite, which lacks antioxidant defences.

4.3.2. Side Effects

These antiparasitic drugs while most effective during the acute stage of infection, have severe side effects and limited treatment efficacy in chronic Chagas. BZN has a high rate of adverse reactions which often leads to the discontinuation of treatment in 15 - 20% of patients (Torrico et al., 2021). Common side effects include dermatological reactions and gastrointestinal symptoms (Aldasoro et al., 2018).

Furthermore, treatment regimens are lengthy; typically lasting 60 days (de Andrade et al., 1996), and the risk of reinfection remains, particularly in endemic areas. This is largely due to the quiescent nature of the intracellular amastigote form of *T. cruzi*, which can persist indefinitely in a dormant state within host tissues, evading treatment and potentially re-establishing replication later (Jayawardhana et al., 2023).

Animal studies have raised concerns about potential reversible impairment of male fertility, and embryotoxicity studies have revealed that BZN exposure during pregnancy can result in foetal malformations. Although, such effects have not been conclusively demonstrated in humans, patients are advised about the risks prior to starting treatment (U.S. Food and Drug Administration; Pharmacology, 2017).

In addition to tolerability concerns, doubts have also emerged regarding the long-term effectiveness of BZN in patients with established cardiomyopathy The landmark BENEFIT (Benznidazole Evaluation for Interrupting Trypanosomiasis) trial conducted by Morillo et al. (2015), demonstrated that while benznidazole reduces parasite load in the blood, it does not improve survival or halt cardiac disease progression in patients with established cardiomyopathy. These findings stress the importance of treating patients earlier, before irreversible tissue damage occurs and highlights the importance of early detection and treatment.

4.3.3. Regulatory Status

BZN and NFX remain first-line therapies endorsed by the World Health Organisation (WHO, however, they lack widespread regulatory approval (World Health Organization, 2023). In many regions, treatment is administered on a compassionate use basis. Despite being on the market for over 50 years, the U.S. Food and Drug Administration (FDA) did not approve BZN until 2017 for children aged 2 to 12 years; and NFX in 2020 for paediatric patients under 18

years. In Europe, regulatory approval has been slower, with paediatric use of NFX only authorised for use as of 2022 through a Paediatric Investigation Plan (PIP) (European Medicines Agency (EMA), 2022).

As of 2025, neither drug has been approved for adult-use by the FDA or the EMA. The timeline of major regulatory milestones for BZN and NFX are summarised in *Figure 11*.

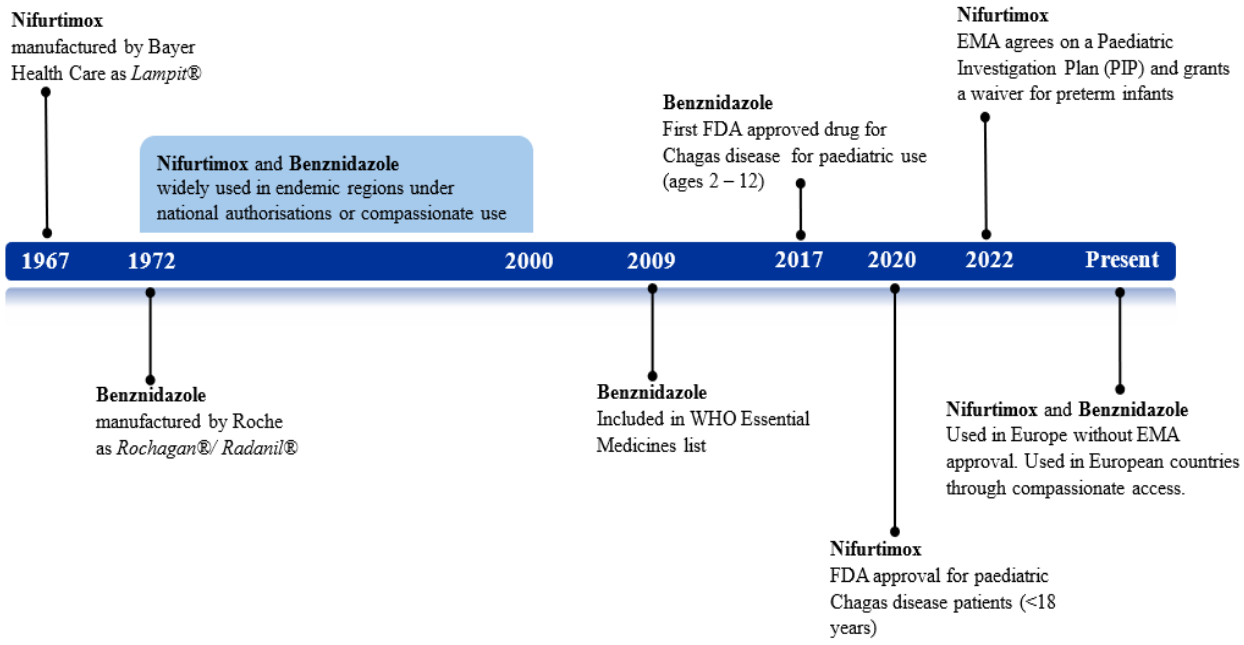

Figure 11. Timeline of major regulatory milestones for benznidazole and nifurtimox in Europe and the United States of America. Timeline created by author, summarising the key developments in the approval and use of benznidazole and nifurtimox for the treatment of Chagas disease

5. Immune Evasion and Survival of *Trypanosoma cruzi* Within Host Cells

Despite triggering several components of the innate immune system, *T. cruzi* has developed sophisticated strategies to evade immune-mediated responses. This allows the parasite to persist and replicate within the host for years or even decades which drives the progression to chronic Chagas disease. By understanding how *T. cruzi* invades host cells and avoids immune detection, researchers may reveal vulnerabilities that can be exploited for therapeutic development.

5.1. Host Immune Recognition and Parasite Entry

Trypanosoma cruzi metacyclic trypomastigotes are extensively glycosylated with O-linked mucins, which are anchored to the parasite's surface via glycosylphosphatidylinositol (GPI) anchors (Pech-Canul et al., 2017). These GPIs are expressed in all developmental stages of *T. cruzi* and consist of a conserved hydrophilic glycan core linked to a lipid moiety (Borges et al., 2021). The structural composition of GPI-anchored mucins in different life stages was first comparatively characterised by Acosta-Serrano et al. (1995), highlighting that while the glycan core is conserved across all developmental stages, the lipid moiety exhibits greater variability.

5.1.1. Invasion of Immune Cells

The innate immune response against *T. cruzi* is initiated by pattern recognition receptors (PRR) such as Toll-like receptors (TLRs), which detect highly conserved pathogen-associated molecular patterns (PAMPs). Among them, TLR2 is the most potently activated (Rodrigues et al., 2012; Almeida et al., 2000) recognising an alkylacylglycerolipid residue at the sn-2 position of the GPI lipid tail. In addition, trypomastigotes also express glycoinositolphospholipids (GIPL) on their surface which activate TLR4, while TLR9 (which is expressed intracellularly

within endosomal compartments), recognises *T. cruzi* DNA when internalised by the host cell (Koo et al., 2018).

Activation of these receptors triggers the TIR (Toll/ Interleukin-1 Receptor) intracellular signalling cascades for the release of pro-inflammatory cytokines; interleukin-12 (IL-12) and tumour necrosis factor alpha (TNFα). IL-12 promotes the differentiation of CD4+ T cells into Th1 cells and IFN-γ production, while TNFα enhances the microbicidal activity of macrophages and further amplifies inflammation, through further cytokine release (Wu et al., 2025).

5.1.2. Invasion of Non-Phagocytic Cells

Unlike phagocytic cells, which recognise and engulf *T. cruzi* through phagocytosis, non-phagocytic host cells such as cardiomyocytes and epithelial cells, are actively through a parasite driven mechanism. This process is mediated by the parasite's Gp35/50 mucins, a family of highly sialylated surface glycoproteins that bind Annexin A2 receptors on non-immune host cell membranes, facilitating adhesion to the cell surface and enabling active invasion.

Following adhesion, a rapid increase in intracellular calcium (Ca^{2+}) triggers lysosome recruitment (Yoshida & Cortez, 2008) and fusion with the plasma membrane, a process that mimics the host's natural plasma membrane repair response (Tardieux et al., 1992). This process 'tricks' the host cell into interpreting the Ca^{2+} influx as extracellular, as if the membrane had been compromised (Idone et al., 2008).

Acid sphingomyelinase (ASM) secreted from lysosomes into the extracellular space hydrolyses lipid components of the outer membrane, into ceramide, which promote membrane curvature and increased flexibility. The inward bending of the membrane envelops *T. cruzi* and forms the

parasitophorous vacuole (*Figure 4)*, thereby bypassing the need for classical phagocytosis (Fernandes & Andrews, 2012; Burleigh & Woolsey, 2002).

5.1.3. DTU-Specific Variability in Mucin-Mediated Entry

Recent studies suggest that the pathogenicity may vary across DTUs. Soares et al. (2012) demonstrated that while all strains express Gp35/50 mucins, different DTUs had varying glycosylation patterns of a terminal α-galactopyranosyl. This polymorphism could partly explain differences in infectivity, tissue tropism, and immune evasion across DTUs, warranting further investigation into how mucin composition shapes parasite-host interactions.

5.2. Immune Evasion

5.2.1. Immunometabolism and Macrophage Dysfunction

While much remains to be understood about the precise mechanisms by which *Trypanosoma cruzi* infects and evades host immune responses, growing evidence highlights the role of metabolic reprogramming in immune evasion. A study conducted by Koo et al. (2018), demonstrated that although *T. cruzi*-infected murine and human macrophages produced cytokine responses at levels comparable to those in classically activated macrophages, neither however, were able to effectively eradicate the parasite. In essence, host cells infected with *T. cruzi* can ‘sound the alarm but lack the weapons to act on it’. This failure was linked to the macrophages’ continued reliance on oxidative metabolism regulated by Peroxisome Proliferator-Activated Receptor Alpha (PPAR-α), rather than shifting to Warburg glycolysis and the pentose phosphate pathway (PPP), which are needed for producing reactive oxygen (ROS) and nitrogen species (NO) to kill intracellular *T. cruzi*.

Notably, IFN-γ treatment was shown to reprogram macrophage metabolism in favour of glycolysis and PPP, restoring their ability to elicit a potent NO/ROS response and gain control

of *T. cruzi* replication. Additionally, inhibition of PPP enzyme, phosphogluconate dehydrogenase (PGD), led to decreased ROS and NO production, further confirming that these pathways are crucial for macrophage antimicrobial activity.

This metabolic dysfunction likely supports long-term parasite persistence, allowing Tc24-expressing amastigotes to survive and replicate within immunologically compromised macrophage populations. As Tc24 is expressed throughout the intracellular stages of *T. cruzi*, its sustained presence within metabolically dysregulated cells may represent a key mechanism of immune evasion and contribute to the parasite's ability to establish chronic infection.

6. Novel Vaccine Candidates

Despite the discovery of Chagas disease more than a century ago, no effective vaccine has of yet been developed. This is in part due to the complexity of targeting the chronic stage of infection. During which the parasite persists intracellularly and evades immune detection. The quiescent nature of intracellular amastigotes further complicates vaccine design. The forms can remain metabolically inactive, and undetected for extended periods, potentially allowing for reinfection post treatment. In addition to the molecular challenges, there are also significant logistical challenges of developing a vaccine that is cost effective, orally administrable, thermostable, and does not rely on cold-chain transport (IQVIA, 2025).

Other factors that have influenced the development of new treatments is a lack of financial incentive from the private sector. Chagas disease predominantly affects socioeconomically disadvantaged regions of Latin America, which offer limited commercial return. Consequently, Chagas disease has been largely overlooked by the biopharmaceutical industry, current progress is predominantly driven by academic institutions and non-profit organisations (Farani et al., 2024).

6.1. Tc24 Flagellar Calcium Binding Protein (FCaBP)

A promising vaccine candidate is the 24 kDa flagellar calcium-binding protein (FCaBP), also known as Tc24. Structurally, Tc24 is composed of four EF-hand motifs as displayed in *Figure 12,* characterised by helix–loop–helix structures, with EF3 and EF4 capable of binding calcium (Wingard et al., 2008). Although the function of Tc24 remains to be elucidated, it is believed to contribute to calcium-dependent processes such as parasite motility via the flagellar (Versteeg et al., 2021).

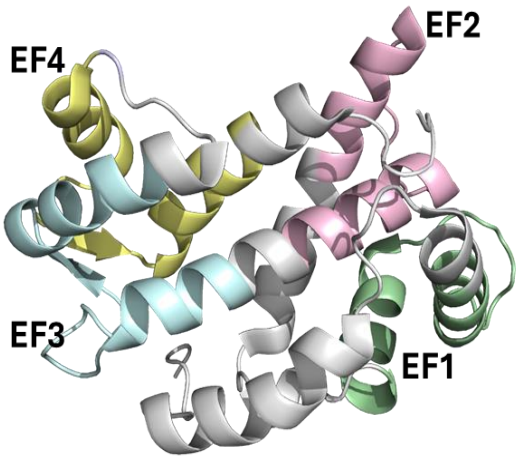

Figure 12. PDB 3CS1: Closed crystal structure of Tc24 in its calcium-free state. The EF-hand motifs, individually colour coded to distinguish each motif, facilitate calcium binding and are characterised by helix–loop–helix structures. In the absence of calcium, they adopt a "closed" conformation, resulting in a more globular overall structure.

Tc24 has been described as a B-cell superantigen that may facilitate immune evasion by non-specifically binding to naïve B cells and triggering their inactivation or deletion. This phenomenon results in the deletion of entire populations of B cells from the immune repertoire, creating "holes" in the host's antibody response and consequently, facilitating immune evasion (Gunter et al., 2016).

Paradoxically, despite Tc24 involvement in immune evasion, it remains an attractive vaccine candidate. Its expression across all morphological stages of the parasite, enhances its appeal for targeting both the acute and chronic stages of infection (Garg & Tarleton, 1998; Versteeg et al., 2021). Furthermore, Tc24 is also a highly conserved protein across DTUs, with sequence percent identity exceeding 98%, as displayed in *Table 1*. To evaluate this conservation, Tc24 nucleotide sequences from representative strains of TcI–TcVI were retrieved from GenBank and aligned using MUSCLE (Potter et al., 2024), a widely used multiple sequence alignment algorithm that applies iterative refinement to improve accuracy. This high level of conservation is crucial for the development of a universally effective vaccine, particularly given the wide geographical distribution of DTUs across the Americas (*Figure 8*).

Table 1. Muscle multiple sequence alignment of *T. cruzi* DTUs TcI - TcVI

DTU	Strain	GenBank accession	TcI	TcII	TcIII	TcIV	TcV	TcVI
			% Homology					
TcI	NAYARIT	OL781152	100.00	98.83	98.83	99.53	99.53	99.30
TcII	000Y	OL781170	98.83	100.00	100.00	99.30	99.30	99.53
TcIII	3663	OL781171	99.53	99.30	99.30	100.00	100.00	99.77
TcIV	4167	OL781172	99.53	99.30	99.30	100.00	100.00	99.77
TcV	LL014	OL781173	99.30	99.53	99.53	99.77	99.77	100.00
TcVI	CLBRENER	AF192980.2	98.83	100.00	100.00	99.30	99.30	99.53

Historically, Tc24 has been long considered to be a surface exposed flagellar protein, localised to the flagellar pocket, according to early literature (Engman et al., 1989; Martinez-Campos et al., 2015). However, subsequent studies have suggested that Tc24 instead anchors to the inner leaflet of the flagellar membrane via N-terminal myristoylation and palmitoylation (Wingard et al., 2008; Maric et al., 2011; Godsel & Engman, 1999). These assumptions were definitively resolved by Versteeg et al., (2021), who demonstrated that Tc24 is not accessible on the external surface of *T. cruzi* trypomastigotes, as antibody binding was only observed following parasite permeabilisation. This indicated that Tc24 is internally situated in the inner leaflet of the flagellar membrane rather than being surface-exposed. As a result, this suggests that vaccine protection conferred by Tc24 is unlikely to stem from antibody mediated phagocytosis and may instead come from T-cell mediated immunity.

Supporting this, research conducted by Villanueva-Lizama et al., (2018) demonstrated that Tc24 is highly immunogenic and capable of inducing strong memory T-cell responses in chronically infected individuals. This is particularly significant given the quiescent nature of intracellular *T. cruzi* amastigotes, which can persist in a dormant state within host tissues for

years without triggering a strong immune response, thereby evading immune-mediated clearance and drug treatment (Sánchez-Valdéz et al., 2018).

A vaccine incorporating Tc24 antigens could therefore promote long-term immune surveillance by generating $CD4^+$ and $CD8^+$ memory T cells. Upon reactivation of dormant amastigotes, the immune system would be capable of mounting a rapid response by targeting and impairing the parasite before it can establish high levels of parasitaemia.

6.2. TcPOP

While Tc24 remains one of the most extensively studied vaccine candidates for *T. cruzi*, a growing body of research has identified additional antigens that may contribute to a multivalent vaccine strategy. Among these, *T. cruzi* 80 kDa prolyl oligopeptidase (TcPOP, also known as Tc80) has emerged as a compelling candidate and is one of several antigens highlighted in the Vaccine Investigation and Online Information Network (VIOLIN) for its vaccine relevance (He et al., 2014). It is a large serine hydrolase expressed in the intracellular amastigote and blood trypomastigote stages. It is believed to facilitate non-immune host cell entry by degrading extracellular matrix (ECM) components such as fibronectin and collagen (Bastos et al., 2005; Grellier et al., 2001)

In the pivotal study by Bivona et al. (2018), it was shown that anti-TcPOP antibodies were able to inhibit TcPOP enzymatic activity and consequently prevented *T. cruzi* trypomastigotes from invading non-phagocytic cells. Furthermore, mice immunised with TcPOP showed reduced parasitaemia and increased survival when infected with *T. cruzi*. Encouragingly, these findings support TcPOP as a potential vaccine. However, the most effective protection came from a heterologous prime-boost strategy (Lu, 2009). Given that Chagas disease predominantly affects a low-income, resource limited demographic, this approach may not be the most feasible.

Recent studies by Campeotto et al. (2024) indicate that while anti-TcPOP antibodies do not cross-react with human POP homologs, they do show cross-reactivity with other kinetoplastid parasites, such as *Leishmania infantum* and *T. brucei*. Given that *Leishmania infantum* co-occurs with *T. cruzi* in several endemic regions (Rosypal et al., 2007), this could potentially lead to false positives in serological testing, thereby limiting the effectiveness of TcPOP as a diagnostic tool for Chagas disease.

7. New Emerging Technologies Using Artificial Intelligence

Advances in deep learning (DL) platforms, accelerated by the exponential growth in computational power and coupled with the decreasing cost of gene synthesis, have significantly expedited progress in vaccine design and binder engineering (Hederman & Ackerman, 2023). To appreciate the enormous scale these platforms can navigate, consider that the average protein sequence is 200 residues in length and is composed of 20 naturally occurring amino acids. The number of possible protein sequence combinations totals 20^{200}, far exceeding the number of proteins currently characterised (Huang et al., 2016).

Now, with the integration of AI, researchers can explore novel proteins that are not found in nature, thus enabling, rapid, in silico development of more diverse, cost-effective, and potentially more potent vaccines (Olawade et al., 2024). This is especially valuable for neglected diseases like Chagas disease, where conventional targets are often poorly characterised (Bravi, 2024). Cutting-edge DL platforms, such as RoseTTAFold, developed by the Baker Lab and AlphaFold2 created by the company DeepMind, now offer the ability to accurately predict the structure from its amino acid sequence (Jumper et al., 2021; Baek et al., 2021). This circumvents the need for experimentally solved structures, obtained through time-consuming and costly methods such as nuclear magnetic resonance (NMR) spectroscopy and X-ray crystallography (Meng et al., 2025). This development opens new possibilities for targeting proteins like Tc24, where only the partial crystal structure has been resolved (PDB: 3CS1; Wingard et al., 2008).

7.1. Structural Prediction as a Foundation for AI-Driven Vaccine Design

Prior to the development of DL platforms, protein structure prediction primarily relied on traditional template-based approaches such as homology modelling. Commonly used tools included PHYRE2 and Modeller. These methods used multiple sequence alignments (MSAs)

to align the unknown protein sequence with homologous sequences with known structures (typically requiring ≥ 50% sequence similarity), and generate a predicted model based on conserved regions (Hasani & Barakat, 2017). However, this approach cannot be extended to larger or multi-domain proteins due to computational constraints (Gupta et al., 2014).

A case study by Lee, Su & Tseng, (2022) compared traditional methods (PHYRE2 and Modeller) to novel DL-based models such as AlphaFold2 and RoseTTAFold and found that while template-based tools produced more accurate predictions when high-quality structural templates were available, AlphaFold2 and RoseTTAFold significantly outperformed them when predicting novel structures in the absence of a suitable homologous template.

The effectiveness of both traditional and DL approaches has been systematically evaluated through the Critical Assessment of protein Structure Prediction (CASP). This is a community-led, biennial experiment, where protein prediction models are blindly tasked with resolving protein structures that have been experimentally solved, but not yet published (Kryshtafovych et al., 2021). Results from CASP14 and CASP15 series clearly demonstrate that AlphaFold2 significantly outperformed all other models, with RoseTTAFold ranking closely behind in CASP15 (Kryshtafovych et al., 2023).

The advancement of AI models, now approaching the accuracy of experimentally derived structures as shown in the latest CASP series, offers a novel and promising strategy for vaccine development.

7.2. RoseTTAFold Diffusion

RoseTTAFold Diffusion (RF diffusion) is a diffusion-based generative model developed by Prof. Baker's laboratory at the University of Washington (USA). This DL model is founded on the RoseTTAFold architecture. During its training, experimentally solved PDB (Protein Data Bank) structures were distorted by adding Gaussian noise to each residue's Cα coordinates and

introducing Brownian rotational noise to the residue's orientation. RF diffusion learnt how to revert these distortions to regenerate the original PDB structure (Watson et al., 2023). This learning process is analogous to presenting the model with a distorted photograph and teaching it how to reverse these distortions to restore the original, clear image.

RF diffusion has a multitude of uses; however, for this review we will focus on the targeted design of de novo protein binders. The model begins with an input target protein. A cloud of random, unstructured residues is dispersed near the epitope, simulating noise. The backbone model gradually refines itself through a series of iterative denoising steps, leading to a more compact and physically realistic structure that specifically docks to the target epitope (*Figure 13)*.

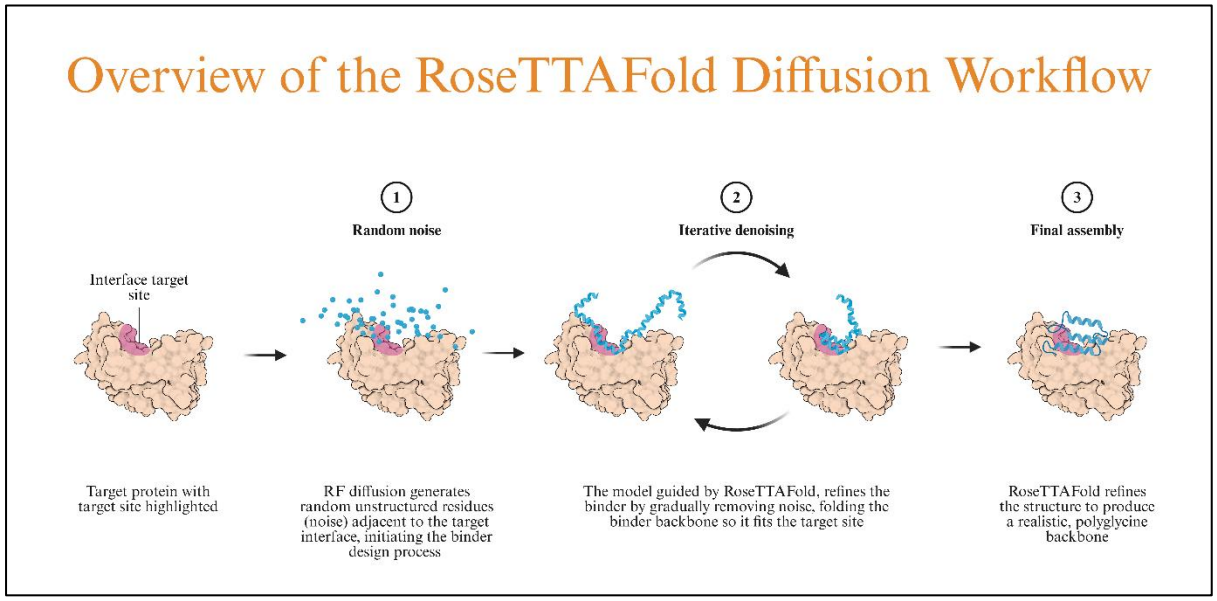

Figure 13. A schematic of the RF diffusion process to design de novo binders to a target protein. *Figure generated using* (BioRender, 2024)

When the resulting polyglycine backbone is combined with other sequence–design models like ProteinMPNN, the polyglycine backbone can be replaced with amino acid residues compatible with the generated backbone model.

Recent proof-of-concept studies conducted by Vázquez Torres et al. (2025) displayed the therapeutic potential of RF diffusion-designed protein binders for neutralising snake venom toxins. The two de novo neurotoxin binders exhibited remarkable stability and potency, while the experimentally determined structures closely aligned with the computationally designed models. Encouragingly, both binders were able to achieve 100% survival in animal studies post-envenomation, confirming that RF diffusion designs can function in vivo.

7.3. Alternatives to RF diffusion: BindCraft and Boltz-1

In addition to RF diffusion, new models like BindCraft are emerging (Pacesa et al., 2024). BindCraft, developed through a collaboration between the Correia Lab (EPFL) and the Ovchinnikov Lab (MIT), employs a hallucination-based approach, where the model starts with a random amino acid sequence and 'hallucinates' a potential structure that it could fold into, while simultaneously adjusting the sequence to improve structural stability (Anishchenko et al., 2021). Unlike RF diffusion, which begins with a random spatial distribution of residues, BindCraft starts with a random sequence and utilises backpropagation to assess how much its predictions differ from the intended structure.

Similar to RF diffusion, BindCraft has numerous applications, including the design of de novo binders that can be targeted to specific receptors. While in vivo assessments are yet to be published, the group who designed BindCraft have claimed that through *in vitro* tests their binders have a nanomolar affinity to their target which has been achieved by facilitating the flexible docking of the generated binder to the target, which is an attribute not used by many other models, thereby exploring novel and uncharacterised binding sites.

Building on these innovations, researchers at the Massachusetts Institute of Technology (MIT) Jameel Clinic for Machine Learning in Health, have recently introduced Boltz-1, a model their developers have described as performing at a level comparable to AlphaFold3 (Wohlwend et

al., 2024). This model adopts a fundamentally different strategy compared to RF diffusion and BindCraft. Rather than relying on diffusion or hallucination-based generative designs, Boltz-1 employs a Boltzmann distribution framework. This allows Boltz-1 to favour protein structures with the lowest free energy that correspond to the most thermodynamically stable conformations (Aranganathan et al., 2025). By prioritising energetically favourable structures, Boltz-1 offers an advantage over other models in generating stable conformations that are more likely to exist in nature.

Although still in the early stages, Boltz-1 has shown promise, as indicated in the CASP15 series (MIT, 2024). As with BindCraft, further validation studies both in animals and in vitro, are required to confirm the applicability of Boltz-1 to real-world therapeutic development. Collectively, the emergence of these next-generation AI platforms represents a rapidly growing toolbox for designing protein-based vaccines and diagnostics, particularly for diseases like Chagas disease, where traditional strategies have consistently fallen short (de la Torre et al., 2021).

7.4. How AI is emerging in diagnostic applications

Not only is AI emerging in vaccine development, but it is also making strides in clinical diagnosis. A paper by Muzammil et al. (2024) describes a new AI-enhanced ECG model for diagnosing cardiovascular diseases where data interpretation is challenging (ref).

This suggests that AI could also be applied to the diagnosis of chronic Chagas in patients whose hearts are subtly deteriorating prior to developing chronic cardiomyopathy. This approach would be beneficial, as early ventricular impairment is still reversible, and if treated early with vaccine targets such as Tc24, prognosis greatly improves.

8. Conclusion

Over a century after its discovery, Chagas disease remains without an effective vaccine. This review highlights how *Trypanosoma cruzi's* immune evasion tactics and genetic variability have obstructed traditional vaccine strategies. Among promising candidates, Tc24, a flagellar calcium binding protein, has stood out for its high conservation and ability to elicit potent T-cell responses.

The emergence of Deep Learning protein prediction platforms; RF diffusion, BindCraft, and Boltz-1, offer new opportunities to engineer highly precise protein binders that can enhance vaccine efficacy and potentially improve diagnostics. While still in early development, these tools represent a significant shift towards rational vaccine design. If successfully validated in preclinical models, the convergence of conserved antigens like Tc24 and next-generation AI binders could finally make lineage-wide protection against Chagas disease a realistic goal.

9. Appendices

9.1. Appendix I

Strain	Country	Region/ State	Host	DTU	GenBank Accession number
OPS21 cl11	Venezuela	Cojedes	*Homo sapiens*	TcI	OR513529.1
P209 cI93	Bolivia	Chuquisaca, Sucre	*Homo sapiens*	TcI	OR513530.1
Teh cI2 cI92	Mexico	Jalisco, Tehuantepec	*Triatoma sp.*	TcI	OR513532.1
MAS1 cl1	Brazil	Brasilia	*Homo sapiens*	TcII	OR513527.1
TU18 cl2	Bolivia	Potosi, Tupiza	*Triatoma infestans*	TcII	OR513533.1
X109/2	Paraguay	Makthlawaiya	*Canis familiaris*	TcIII	OR513535.1
92122102R	USA	Georgia, Statesboro	*Procyon lotor*	TcIV	OR513523.1
DogTheis	USA	Unknown	*Canis familiaris*	TcIV	OR513526.1
Bug2148 cI1	Brazil	Rio Grande do Sul	*Triatoma infestans*	TcV	OR513524.1
MN cl2	Chile	Coquimbo, Illapel	*Homo sapiens*	TcV	OR513528.1
SC43 cl1	Bolivia	Andres Ibañez, Santra Cruz	*Triatoma infestans*	TcV	OR513531.1
CL Brener	Brazil	Rio Grande do Sul	*Triatoma infestans*	TcVI	OR513525.1
Tula cl2	Chile	Coquimbo, Tulahuen	*Homo sapiens*	TcVI	OR513534.1
TCC 204	Brazil	São Paulo	*Myotis ruber*	TcBat	KT305778.1
TCC 312	Brazil	Mato Grosso do sul	*Noctilio albiventris*	TcBat	KT305779.1
TCC 480	Brazil	Mato Grosso do sul	*Noctilio albiventris*	TcBat	KT305780.1
TCC 499	Brazil	Mato Grosso do sul	*Myotis nigricans*	TcBat	KT305781.1

10. References

Acosta-Serrano, A. et al., 1995. The lipid structure of the glycosylphosphatidylinositol-anchored mucin-like sialic acid acceptors of *Trypanosoma cruzi* changes during parasite differentiation from epimastigotes to infective metacyclic trypomastigote forms. *Journal of Biological Chemistry,* 270(44), p. 27244–27253.

Afonso, A. M., Ebell, M. H. & Tarleton, R. L., 2012. A Systematic Review of High Quality Diagnostic Tests for Chagas Disease. *PLOS Neglected Tropical Diseases,* 6(11).

Aldasoro, E. et al., 2018. What to expect and when: benznidazole toxicity in chronic Chagas' disease treatment. *Journal of Antimicrobial Chemotherapy,* 73(4), pp. 1060-1067.

Almeida, I. et al., 2000. Activation of TLR2 by *Trypanosoma cruzi* glycosylphosphatidylinositol anchors containing ether lipids. *Journal of Immunology,* 165(1), pp. 183-191.

Alonso-Padilla, J. et al., 2020. Target product profile for a test for the early assessment of treatment efficacy in Chagas disease patients: An expert consensus. *PLOS Neglected Tropical Diseases,* 14(4).

Anishchenko, I. et al., 2021. De novo protein design by deep network hallucination. *Nature,* 600(7889), pp. 547-552.

Apt, W. & Zulantay, I., 2013. Xeno-diagnosis in the evaluation of chronic Chagas disease patients: experience in Chile. *Biological Research,* 46(3), pp. 219-222.

Aranganathan, A. et al., 2025. Modeling Boltzmann-weighted structural ensembles of proteins using artificial intelligence–based methods. *Current Opinion in Structural Biology,* p. 91.

Ascanio, L., Carroll, S., Paniz-Mondolfi, A. & Ramírez, J., 2024. In vitro diagnostic methods of Chagas disease in the clinical laboratory: a scoping review. *Frontiers in Microbiology,* Volume 15.

Ávila-Santos, E. et al., 2025. Vaccines against Chagas' disease: a synthetized up-to-date review.. *Revista DELOS – Desarrollo Local Sostenible,* 18(54).

Baek, M. et al., 2021. Accurate prediction of protein structures and interactions using a three-track neural network. *Science,* 373(6557), pp. 871-876.

Ballesteros-Rodea, G., Martínez Cuevas, T., Jiménez-Ramos, B. & Antonio-Campos, A., 2018. Chagas disease: an overview of diagnosis. *Journal of Microbiology & Experimentation,* 6(3), pp. 151-157.

Barrias, E., Reignault, L. C. & De Souza, W., 2019. How Does the Main Infective Stage of *T. cruzi* Enter and Avoid Degradation in Host Cells?. In: *Biology of Trypanosoma cruzi.* s.l.:IntechOpen, pp. 1 - 12.

Bastos, I. et al., 2005. Molecular, functional and structural properties of the prolyl oligopeptidase of *Trypanosoma cruzi* (POP Tc80), which is required for parasite entry into mammalian cells. *Biochemical Journal,* Volume 388, pp. 29-38.

Bayer HealthCare Pharmaceuticals Inc., 2023. *Lampit (nifurtimox) tablets – Prescribing Information,* s.l.: FDA.

Bern, C., 2011. Antitrypanosomal Therapy for Chronic Chagas' Disease. *New England Journal of Medicine,* 364(26), pp. 2527-2534.

Bern, C., Messenger, L., Whitman, J. & Maguire, J., 2019. Chagas Disease in the United States: A Public Health Approach. *Clinical Microbiology Reviews,* Volume 33.

BioRender, 2024. *BioRender – Science Illustration Tool.* [Online]
Available at: https://BioRender.com

Bivona, A. et al., 2018. *Trypanosoma cruzi* 80 kDa prolyl oligopeptidase (Tc80) as a novel immunogen for Chagas disease vaccine. *PLoS Neglected Tropical Diseases,* 12(12).

Borges, A., Link, F., Engstler, M. & Jones, N., 2021. The Glycosylphosphatidylinositol Anchor: A Linchpin for Cell Surface Versatility of Trypanosomatids. *Frontiers in Cell and Developmental Biology,* Volume 9.

Bravi, B., 2024. Development and use of machine learning algorithms in vaccine target selection. *npj Vaccines,* 9(1), p. 15.

Brenière, S., Waleckx, E. & Barnabé, C., 2016. Over six thousand *Trypanosoma cruzi* strains classified into Discrete Typing Units (DTUs): Attempt at an inventory. *PLOS Neglected Tropical Diseases,* 10(8).

Brisse, S., Verhoef, J. & Tibayrenc, M., 2001. Characterisation of large and small subunit rRNA and mini-exon genes further supports the distinction of six *Trypanosoma cruzi* lineages. *International Journal of Parasitology,* 31(11), pp. 1218-1226.

Burleigh, B. & Woolsey, A., 2002. Cell signalling and *Trypanosoma cruzi* invasion. *Cellular Microbiology,* 4(11), pp. 701-711.

Campeotto, I. et al., 2024. Resolving multiple conformations of a sub-80 kDa Chagas vaccine candidate by cryo-EM led integrative approach.. *Research Square.*

CDC Public Health Image Library (PHIL), 1968. *Photomicrograph of Trypanosoma cruzi trypomastigotes in a blood smear (ID: 21029),* s.l.: s.n.

CDC, 2023. *Chagas disease- Diagnosis and Testing.* [Online]
Available at: https://www.cdc.gov/chagas/hcp/diagnosis-testing/index.html
[Accessed 10 June 2025].

Centers for Disease Control and Prevention (CDC), DPDx, 2021. *American Trypanosomiasis (also known as Chagas Disease).* [Online]
Available at: https://www.cdc.gov/dpdx/trypanosomiasisamerican/index.html
[Accessed 09 June 2025].

Chagas, C., 1909. Nova tripanozomiaze humana: Estudos sobre a morfolojia e o ciclo evolutivo do Schizotrypanum cruzi n. gen., n. sp., ajente etiolojico de nova entidade morbida do homem. *Memorias Do Instituo Oswaldo Cruz,* Volume 1, pp. 159-218.

Cucunubá, Z. et al., 2024. The epidemiology of Chagas disease in the Americas. *The Lancet Regional Health – Americas,* Volume 37.

Datawrapper GmbH, 2025. *Datawrapper: Create charts, maps, and tables,* s.l.: s.n.

de Andrade, A. et al., 1996. Randomised trial of efficacy of benznidazole in treatment of early *Trypanosoma cruzi* infection. *Lancet,* 348(9039), pp. 1407-1413.

de la Torre, L. et al., 2021. Recent Advances in the Diagnosis and Treatment of Chagas Disease: A Review. *Tropical Medicine,* 6(1), p. 16.

DNDi, 2025. *Chagas Disease: Facts.* [Online]
Available at: https://dndi.org/diseases/chagas/facts/
[Accessed 12 May 2025].

Engman, D. et al., 1989. A novel Ca^{2+}-binding protein complex located in the flagellar membrane of *Trypanosoma cruzi*. *Journal of Biological Chemistry,* 264(15), pp. 8537-8542.

European Medicines Agency, 2022. *EMA Decision of 11 March 2022 on the agreement of a Paediatric Investigation Plan and granting of a waiver for nifurtimox (EMEA-003134-PIP01-21),* s.l.: European Medicines Agency.

Farani, P., Jones, K. & Poveda, C., 2024. Treatments and the Perspectives of Developing a Vaccine for Chagas Disease. *Vaccines,* 12(5), p. 577.

Fernandes, M. & Andrews, N., 2012. Host Cell Invasion by *Trypanosoma cruzi*: A Unique Strategy that Promotes Persistence. *FEMS Microbiology Reviews,* 36(3), pp. 734-747.

Freitas, V. et al., 2023. Detection of *Trypanosoma cruzi* DTUs TcI and TcIV in two outbreaks of orally-transmitted Chagas disease in the Northern region of Brazil. *Revista do Instituto de Medicina Tropical de São Paulo,* Volume 65.

Garg, N. & Tarleton, R. L., 1998. Characterization of immunodominant antigens of *Trypanosoma cruzi* identified by human immune sera. *Immunology,* 93(4), pp. 511-520.

Godsel, L. & Engman, D., 1999. Flagellar protein localization mediated by a calcium–myristoyl/palmitoyl switch mechanism. *The EMBO Journal,* 18(9), pp. 2057-2065.

Grellier, P. et al., 2001. *Trypanosoma cruzi* prolyl oligopeptidase Tc80 is involved in nonphagocytic mammalian cell invasion by trypomastigotes. *Journal of Biological Chemistry,* 276(50), pp. 47078-47086.

Gunter, S. et al., 2016. Identification and Characterization of the *Trypanosoma cruzi* B-cell Superantigen Tc24. *American Journal of Tropical Medicine and Hygiene,* 94(1), pp. 114-121.

Hall, B. S. & Wilkinson, S. R., 2012. Activation of Benznidazole by Trypanosomal Type I Nitroreductases Results in Glyoxal Formation. *Antimicrobial Agents Chemotherapy,* 56(1), pp. 115-123.

Hasani, H. & Barakat, K., 2017. Homology Modeling: an Overview of Fundamentals and Tools. *International Review on Modelling and Simulations (IREMOS),* 10(2), pp. 61-78.

Hederman, A. & Ackerman, M., 2023. Leveraging deep learning to improve vaccine design. *Trends in Immunology,* 44(5), pp. 333-344.

He, Y. et al., 2014. Updates on the web-based VIOLIN vaccine database and analysis system. *Nucleic Acids Research,* 41(D1), pp. D1124-D1132.

Hotez, P. et al., 2008. The neglected tropical diseases of Latin America and the Caribbean: a review of disease burden and distribution and a roadmap for control and elimination. *PLoS Neglected Tropical Diseases,* 2(9).

Huang, P.-S., Boyken, S. & Baker, D., 2016. The coming of age of de novo protein design. *Nature,* 537(7620), pp. 320-327.

Hudak, J. E., Canham, S. M. & Bertozzi, C. R., 2014. Glycocalyx engineering reveals a Siglec-based mechanism for NK cell immunoevasion. *Nature Chemical Biology,* 10(1), pp. 69-75.

Huerta-Cepas, J., Serra, F. & Bork, P., 2016. ETE 3: Reconstruction, Analysis, and Visualization of Phylogenomic Data. *Molecular Biology and Evolution,* 33(6), pp. 1635-1638.

Idone, V. et al., 2008. Repair of injured plasma membrane by rapid Ca^{2+}-dependent endocytosis. *Journal of Cell Biology,* 180(5), pp. 905-914.

IQVIA, 2025. *Tip of the Iceberg: Economic and Environmental Impact of the Vaccine Cold Chain,* s.l.: s.n.

Jacobs, T., Erdmann, H. & Fleischer, B., 2010. Molecular interaction of Siglecs (sialic acid-binding Ig-like lectins) with sialylated ligands on *Trypanosoma cruzi*. *European Journal of Cell Biology,* 89(1), pp. 113-116.

Jayawardhana, S. et al., 2023. *Trypanosoma cruzi* persisters that survive benznidazole treatment in vitro and in vivo are in a transient non-replicative state. *bioRxiv.*

Jumper, J. et al., 2021. Highly accurate protein structure prediction with AlphaFold. *Nature,* 596(7873), pp. 583-589.

Koo, S. et al., 2016. Macrophages Promote Oxidative Metabolism to Drive Nitric Oxide Generation in Response to *Trypanosoma cruzi*. *Infection and Immunity,* 84(12), pp. 3527-3541.

Koo, S.-j.et al., 2018. Pentose phosphate shunt modulates reactive oxygen species and nitric oxide production controlling *Trypanosoma cruzi* in macrophages. *Frontiers in Immunology,* Volume 9.

Krafts, K., Hempelmann, E. & Oleksyn, B., 2011. In search of the malarial parasite: Biographical sketches of the blood stain contributors. *Parasitology Research,* 109(3), pp. 521 - 529.

Kryshtafovych, A. et al., 2021. Critical assessment of methods of protein structure prediction (CASP)—Round XIV. *Proteins,* 89(12), pp. 1607-1617.

Kryshtafovych, A. et al., 2023. Critical Assessment of Methods of Protein Structure Prediction (CASP) – Round XV. *bioRxiv.*

Laboratorios Liconsa, S.A, 2021. *Benznidazole tablets – Prescribing information.* [Online] Available at: https://dailymed.nlm.nih.gov/dailymed/fda/fdaDrugXsl.cfm?setid=8983d6a0-f63f-4f8e-bba4-38223f39e29b
[Accessed 17 May 2025].

Laranja, F., Dias, E., Nobrega, G. & Miranda, A., 1956. Chagas' disease: A clinical, epidemiologic, and pathologic study. *Circulation,* 14(6), pp. 1035-1060.

Lee, C., Su, B.-H. & Tseng, Y. J., 2022. Comparative studies of AlphaFold, RoseTTAFold and Modeller: a case study involving the use of G-protein-coupled receptors. *Briefings in Bioinformatics,* 23(5), pp. 1-7.

Lewis, M. et al., 2011. Recent, independent and anthropogenic origins of *Trypanosoma cruzi* hybrids. *PLoS Neglected Tropical Diseases,* 5(10).

Lopez-Albizu, C. et al., 2023. Laboratory diagnosis of *Trypanosoma cruzi* infection: a narrative review. *Frontiers in Parasitology,* Volume 2.

Lu, S., 2009. Heterologous prime-boost vaccination. *Current Opinion in Immunology,* 21(3), pp. 346-351.

Marcili, A. et al., 2009. A new genotype of *Trypanosoma cruzi* associated with bats evidenced by phylogenetic analyses using SSU rDNA, cytochrome b and Histone H2B genes and genotyping based on ITS1 rDNA. *Parasitology,* 136(6), pp. 641-655.

Maric, D. et al., 2011. Molecular determinants of the axoneme association and flagellar targeting of the *Trypanosoma cruzi* flagellar calcium-binding protein FCaBP. *Journal of Biological Chemistry,* 286(36), pp. 33109-33117.

Martín-Escolano, J. et al., 2022. An Updated View on the *Trypanosoma cruzi* Life Cycle: Intervention Points for an Effective Treatment. *Infectious Diseases,* Volume 8, pp. 1107-1115.

Martinez-Campos, V. et al., 2015. Expression, purification, immunogenicity, and protective efficacy of a recombinant Tc24 antigen as a vaccine against *Trypanosoma cruzi* infection in mice. *Human Vaccines & Immunotherapeutics,* 11(8), pp. 2148-2153.

Massachusetts Institute of Technology, 2024. *Boltz-1: Thermodynamically accurate protein structure prediction using deep learning.* [Online]
Available at: https://jclinic.mit.edu/boltz-1
[Accessed 10 June 2025].

Melvin, M., 1962. *Young Panamanian girl with Romaña's sign due to acute Chagas disease – PHIL Image ID 15815.* [Online]
Available at: https://phil.cdc.gov/Details.aspx?pid=15815

Meng, Y. et al., 2025. Protein structure prediction via deep learning: an in-depth review. *Frontiers in Pharmacology,* Volume 16.

Messenger, L. A., Miles, M. A. & Bern, C., 2015. Between a bug and a hard place: *Trypanosoma cruzi* genetic diversity and the clinical outcomes of Chagas disease. *Expert Review of Anti-infective Therapy,* 13(8), pp. 995-1029.

Morillo, C. A. et al., 2015. Randomized Trial of Benznidazole for Chronic Chagas' Cardiomyopathy. *Randomized Trial of Benznidazole for Chronic Chagas' Cardiomyopathy,* 373(14), pp. 1295-1306.

Muzammil, M. et al., 2024. Muzammil, M.A.; Javid, S.; Afridi, A.K.; Siddineni, R.; Shahabi, M.; Haseeb, M.; Fariha, F.N.U.; Kumar, S.; Zaveri, S.; Nashwan, A.J.. *Journal of Electrocardiology,* 83(Mar-Apr), pp. 30-40.

Olawade, D. et al., 2024. Leveraging artificial intelligence in vaccine development: A narrative review. *Journal of Microbiological Methods,* Volume 224.

Oliveira, T. D. et al., 2017. *Trypanosoma cruzi* I genotype among isolates from patients with chronic Chagas disease followed at the Evandro Chagas National Institute of Infectious Diseases (FIOCRUZ, Brazil). *Revista da Sociedade Brasileira de Medicina Tropical,* 50(1), pp. 35 - 43.

Onofre, T. S. et al., 2022. Gp35/50 mucin molecules of *Trypanosoma cruzi* metacyclic forms that mediate host cell invasion interact with annexin A2. *PLOS Neglected Tropical Diseases,* 16(10).

Ouaissi, A. et al., 1992. Characterization of major surface and excretory-secretory immunogens of *Trypanosoma cruzi* trypomastigotes and identification of potential protective antigens. *Biology of the Cell,* 74(1-2), pp. 15-23.

Pacesa, M. et al., 2024. BindCraft: a differentiable AlphaFold-guided pipeline for de novo binder design. *bioRxiv,* April.

PAHO, 2023. *The Elimination Initiative: A Platform to Accelerate the Elimination of More Than 30 Communicable Diseases and Related Conditions in the Americas.* [Online]

Available at: https://www.paho.org/en/elimination-initiative

[Accessed 26 May 2025].

PAHO, 2025. *Chagas Disease.* [Online]

Available at: https://www.paho.org/en/topics/chagas-disease

Pech-Canul, Á. d. l. C., Monteón, V. & Solís-Oviedo, R.-L., 2017. A Brief View of the Surface Membrane Proteins from *Trypanosoma cruzi*. *Journal of Parasitology Research,* Volume 2017, pp. 1-13.

Potter, S. et al., 2024. The EMBL-EBI Job Dispatcher sequence analysis tools framework in 2024. *Nucleic Acids Research.*

Previato, J. et al., 1990. Structural analysis of glycosylphosphatidylinositol-anchored mucins from *Trypanosoma cruzi* epimastigotes and trypomastigotes. *Journal of Biological Chemistry,* 265(33), p. 19371–19377.

Previato, J. O. et al., 1995. Structural Characterization of the Major Glycosylphosphatidylinositol Membrane-anchored Glycoprotein from Epimastigote Forms of *Trypanosoma cruzi* Y-strain. *Journal of Biological Chemistry,* 270(13), pp. 7241-7250.

Rajão, M. A. et al., 2014. Unveiling benznidazole's mechanism of action through overexpression of DNA repair proteins in *Trypanosoma cruzi*. *Environmental and Molecular Mutagenesis,* 55(4), pp. 309-321.

Ramírez, J. D. et al., 2014. First Report of Human *Trypanosoma cruzi* Infection Attributed to TcBat Genotype. *Zoonoses and Public Health,* 61(7), pp. 535-543.

Ramírez, J. et al., 2010. Chagas cardiomyopathy manifestations and *Trypanosoma cruzi* genotypes circulating in chronic chagasic patients.. *PLOS Neglected Tropical Diseases,* 4(11).

Rodrigues, M., Oliveira, A. & Bellio, M., 2012. The Immune Response to *Trypanosoma cruzi*: Role of Toll-Like Receptors and Perspectives for Vaccine Development. *Journal of Parasitology Research.*

Rosypal, A. et al., 2007. Serological survey of *Leishmania infantum* and *Trypanosoma cruzi* in dogs from urban areas of Brazil and Colombia. *Veterinary Parasitology,* 149(3-4), pp. 172-177.

Sánchez-Valdéz, F. et al., 2018. Spontaneous dormancy protects *Trypanosoma cruzi* during extended drug exposure. *eLife,* Volume 7.

Schijman, A., 2018. Molecular diagnosis of *Trypanosoma cruzi* infection: A 2018 update. *Acta Tropica,* Volume 184, pp. 59-66.

Soares, R. P. et al., 2012. Intraspecies Variation in *Trypanosoma cruzi* GPI-Mucins: Biological Activities and Differential Expression of α-Galactosyl Residues. *American Journal of Tropical Medicine and Hygiene,* 87(1), pp. 87-96.

Strout, R. G., 1962. A method for concentrating hemoflagellates. *The Journal of Parasitology,* 48(1), p. 100.

Tardieux, I. et al., 1992. Lysosome recruitment and fusion are early events required for trypanosome invasion of mammalian cells. *Cell,* 71(7), pp. 1117-1130.

Teixeira, T. L., Cruz, L., Mortara, R. A. & Da Silva, C. V., 2015. Revealing Annexin A2 and ARF-6 enrollment during *Trypanosoma cruzi* extracellular amastigote-host cell interaction. *Parasites & Vectors,* 8(493).

Torrico, F. et al., 2021. New regimens of benznidazole monotherapy and in combination with fosravuconazole for treatment of Chagas disease (BENDITA): a phase 2, double-blind, randomised trial. *The Lancet Infectious Diseases,* 21(8), pp. 1129 - 1140.

U.S. Food and Drug Administration; Pharmacology, 2017. *Pharmacology/Toxicology Review NDA 209570 – Benznidazole Tablets, 100 mg,* s.l.: Center for Drug Evaluation and Research (CDER).

Vázquez Torres, S. et al., 2025. De novo designed proteins neutralize lethal snake venom toxins. *Nature,* Volume 639, pp. 225-231.

Versteeg, L. et al., 2021. Location and expression kinetics of Tc24 in different life stages of *Trypanosoma cruzi*. *PLoS Neglected Tropical Diseases,* 15(9).

Villanueva-Lizama, L. et al., 2018. *Trypanosoma cruzi* vaccine candidate antigens Tc24 and TSA-1 recall memory immune response associated with HLA-A and -B supertypes in Chagasic chronic patients from Mexico. *PLoS Neglected Tropical Diseases,* 12(7).

Watson, J. L. et al., 2023. De novo design of protein structure and function with RFdiffusion. *Nature,* 620(7976), pp. 1089-1100.

Wingard, J. et al., 2008. Structures of the calcium-sensing, flagellar calcium-binding protein (FCaBP) from *Trypanosoma cruzi*. *Journal of Biological Chemistry,* 283(42), pp. 29135-29146.

Wohlwend, J. et al., 2024. Boltz-1: Democratizing Biomolecular Interaction Modeling. *bioRxiv.*

World Health Organization, 2023. *Chagas disease (American trypanosomiasis) – Fact Sheet.* [Online]

Available at: https://www.who.int/news-room/fact-sheets/detail/chagas-disease-(american-trypanosomiasis)
[Accessed 18 May 2025].

Wu, X. et al., 2025. Interaction between interleukin-12 (IL-12) and its receptor (IL-12Rβ2) mediates $CD4^+$ T cell subsets activation in flounder (*Paralichthys olivaceus*). *International Journal of Biological Macromolecules,* Volume 293.

Yoshida, N. & Cortez, M., 2008. *Trypanosoma cruzi*: Entry into Mammalian Host Cells and Parasitophorous Vacuole Formation. *Cell Microbiology,* 10(4), pp. 705-714.

Zingales, B. et al., 2012. The revised *Trypanosoma cruzi* subspecific nomenclature: rationale, epidemiological relevance and research applications. *Infection, Genetics and Evolution,* 12(2), pp. 240-253.

Expression, Purification and Biophysical Characterisation of *de novo* binders designed against the Flagellar Calcium Binding Protein, Tc24

Thesis submitted to the University of Nottingham in part fulfilment
for the degree of Masters of Research

September 2025

Alicia Richardson, BSc
School of Biosciences
University of Nottingham

Supervisors:
Dr Ivan Campeotto – University of Nottingham
Professor Stephen Harding – University of Nottingham

Word count: 6896

ACKNOWLEDGEMENTS

I would like to thank Dr. Ivan Campeotto for giving me the opportunity to carry out my research project in his group. His guidance, encouragement, and expertise have been invaluable, and I am very grateful for the support he has provided throughout this project.

I would also like to thank Chris Waugh, Sam Skinner, and Oliver Boakye for helping me feel welcome at BABS and for making me feel part of the team. Their support, kindness and endless cups of coffee have created such a positive and collaborative environment that I am delighted to be continuing with them for another four years as I pursue my PhD.

I am grateful to the University of Nottingham for providing the facilities and resources that enabled this work to be carried out as part of my MRes degree.

Finally, I wish to extend heartfelt thanks to my family for their constant encouragement, understanding, and support during this degree. Their patience and belief in me have been a source of motivation throughout this journey.

ABSTRACT

Chagas disease, caused by the protozoan parasite *Trypanosoma cruzi*, remains one of the most neglected tropical diseases, disproportionately effecting affecting socioeconomically impoverished regions across Latin America. Despite over a century of research since its discovery, there is still no effective vaccine, and current therapies rely on the usage of nifurtimox and benznidazole which have been linked to severe side effects. Tc24, a highly conserved flagellar calcium binding protein remains an attractive vaccine candidate.

This study experimentally evaluated six RFdiffusion designed binders against Tc24. Although no functional binders were identified, these results highlight limitations of current binder design pipelines and emphasise the need for incorporating solubility parameters in future Tc24 binder development.

TABLE OF CONTENTS

ABBREVIATIONS

°C	Degrees Celsius
2xYT	2 x Yeast-Tryptone Broth
4 x LB	4 x Laemmli Buffer
A	Ampere
AI	Artificial Intelligence
amp	ampicillin
BirA	Biotin Ligase
BLI	Bio-Layer Interferometry
CD	Chagas Disease
CV	Column Volume
Da	Dalton
E	Elution
E. coli	*Escherichia coli*
ECL	Enhanced Chemiluminescence
EDTA	Ethylenediaminetetraacetic acid
FT	Flow-Through
g	gravity
IMAC	Immobilised Metal Affinity Chromatography
IPTG	Isopropyl β-D-1-thiogalactopyranoside
LB	Luria-Bertani
LY	Lysate
mg	milli grams
min	minute
MW	Molecular Weight
Ni^{2+}	Nickel Ion
nm	Nano meter
NTA	Nitrilotriacetic acid
NTD	Neglected Tropical Disease
OD	Optical Density
ORF	Open Reading Frame
P	Pellet
PBS	Phosphate – Buffered Saline
PBS-T	Phosphate – Buffered Saline, containing 0.05 % Tween-20

PDB	Protein Data Bank
PVDF	Polyvinylidene Fluoride
SDS-PAGE	Sodium Dodecyl Sulphate polyacrylamide gel
SEC	Size Exclusion Chromatography
SN	Supernatant
SOC	Super Optimal broth with Catabolite repression
Tc24	Trypanosoma cruzi 24 kDa flagellar calcium-binding protein
Tx71	Full-length Tc24 variant + HisTag
Tx77	Full-length Tc24 variant with C-terminal AviTag
UV	Ultraviolet
V	Volt
Vr	Retention Volume
W	Wash
µg	Micro gram

Chapter 1

Introduction

1.1. Chagas Disease: Global Burden and Transmission

Chagas disease (CD) is a chronic and often life-threatening condition caused by the hemoflagellate protozoan parasite, *Trypanosoma cruzi,* first identified in 1909 by Carlos Chagas (Chagas, 1909). More than a century later, it continues to pose a major public health burden, primarily affecting socioeconomically impoverished regions across 21 Latin American countries (Perez-Molina & Molina, 2018). Current estimates suggest 6–8 million people are infected worldwide, with around 30,000 new cases and 12,000 deaths occurring annually (PAHO, 2025). In recent years, migration and climate change have contributed to the rising number of reported cases in non-endemic regions, including parts of North America and Europe (Figure 1), broadening the disease's geographic impact (Klein et al., 2012; Medone et al., 2015).

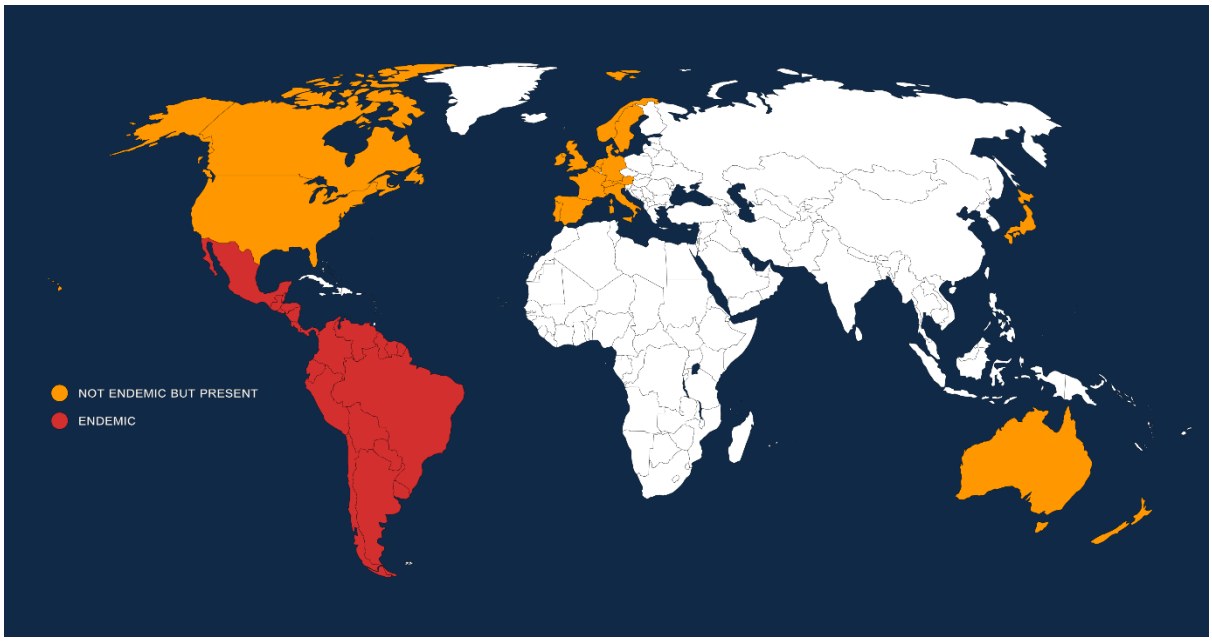

Figure 1. Global distribution of Chagas Disease. Adapted from (DNDi, 2025)

In recognition of this growing public health challenge, the World Health Organisation (WHO) officially designated Chagas disease as a neglected tropical disease (NTD) in 2005 (WHO, 2023), prompting numerous organisations to launch initiatives aimed at its control and eventual elimination (PAHO, 2023; WHO, 2020).

Central to these efforts is understanding how the parasite is transmitted. Transmission occurs primarily when an infected triatomine bug contaminates the bite wound or mucosal membranes with its infective faeces containing metacyclic trypomastigotes (Figure 2). Other routes of transmission include congenital infection, blood transfusion, and foodborne exposure (Coura & Dias, 2009). These diverse transmission routes make prevention difficult and emphasise the need for prophylactic treatments.

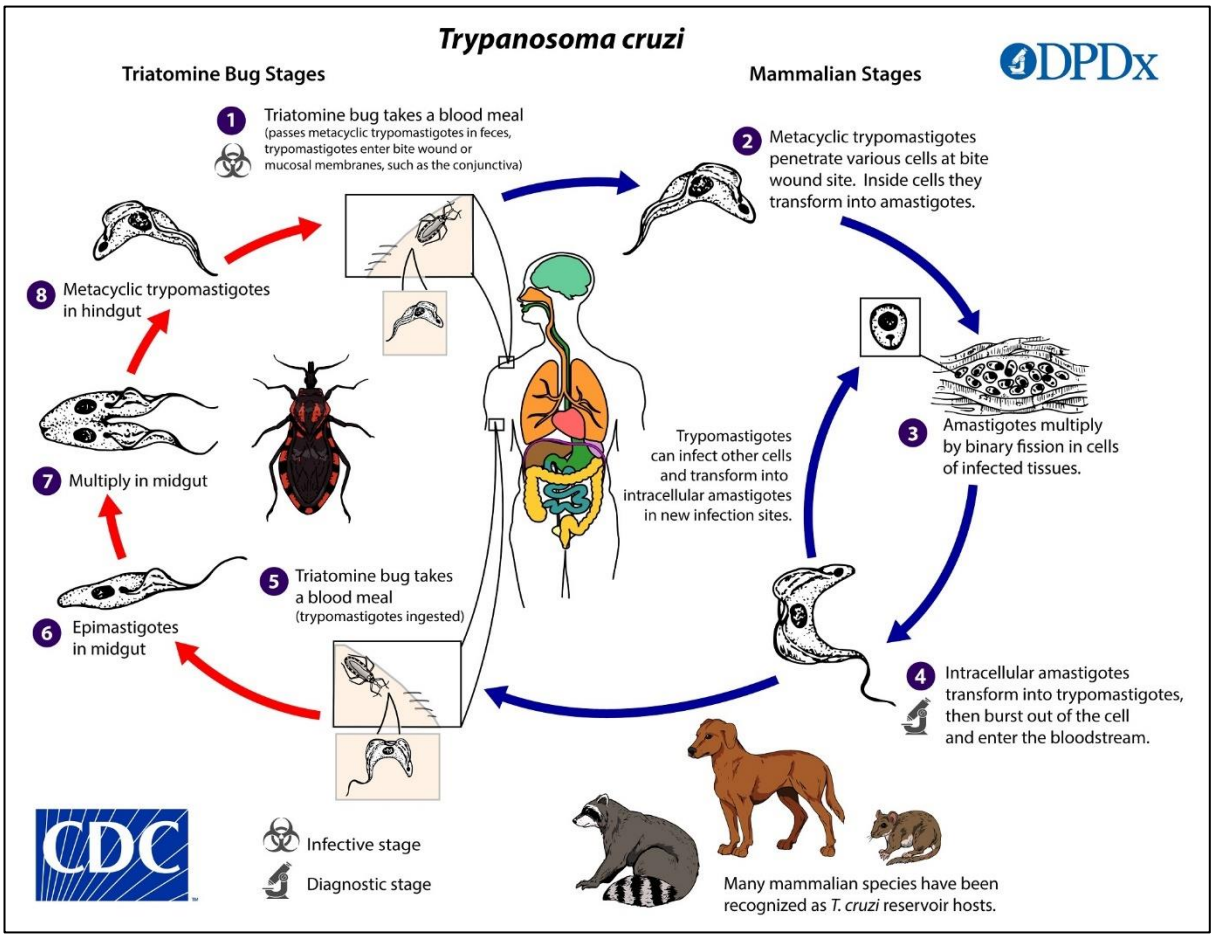

Figure 2. A complete overview of the *T. cruzi* transmission cycle from vector to humans. *Image source: CDC, DPDx, (2021).*

1.2. Diagnostic Challenges and Therapeutic Limitations

Despite international recognition, CD remains profoundly underdiagnosed and undertreated, with fewer than 10% of infected individuals ever receiving a formal clinical diagnosis (Lopez-Albizu et al., 2023; Perez-Molina and Molina, 2018). This is largely attributed to the acute stage, which develops 4 – 8 weeks post-infection and is typically asymptomatic (Bern, 2011). Consequently, most infections remain undetected until the chronic phase, when irreversible cardiac or gastrointestinal complications may already have developed (Rassi et al., 2010).

The chronic phase is divided into indeterminate and determinate phases. During the indeterminate stage, parasitaemia falls below detectable levels, and patients remain seropositive but asymptomatic; this stage can often persist for decades (Bern, 2011). In 30–40% of cases, infection progresses to the determinate stage, where chronic inflammation and tissue damage caused by *T. cruzi* invasion leads to severe complications, most notably Chagas cardiomyopathy, the leading cause of death in CD (Laranja et al., 1956; PAHO, 2025).

Despite the severe pathogenesis of Chagas disease, there is still nworking no vaccine, and treatment options are limited to two drugs: benznidazole and nifurtimox, both introduced over 50 years ago. These drugs, while effective during the acute stage, have limited efficacy during the chronic stages where parasite dormancy presents a major challenge for successful treatment (Jayawardhana, et al., 2023). Both drugs are associated with high risks of adverse effects, including neurological and gastrointestinal symptoms, resulting in treatment discontinuation in 15–20% of patients (Torrico et al., 2021; Aldasoro et al., 2018).

Moreover, the BENEFIT trial further demonstrated that while benznidazole can reduce circulating parasite load, it does not prevent disease progression or improve long-term survival in patients with established cardiomyopathy (Morillo et al., 2015).

Despite these limitations, no new drugs have been approved in the past five decades, reflecting the limited pharmaceutical interest in a disease concentrated among low-income populations (Farani et al., 2024).

Progress has been further complicated by the genomic plasticity of *T. cruzi*, which is divided into six discrete typing units (TcI–TcVI) (Figure 3), each with distinct geographical distributions and clinical associations (Brenière et al., 2016; Messenger et al., 2015; Ramírez et al., 2010). These genetic and regional differences present challenges for therapeutic development, as antigenic variations may impact their effectiveness. Collectively, these barriers highlight the urgent need for improved treatments that can offer both prophylactic and therapeutic benefits.

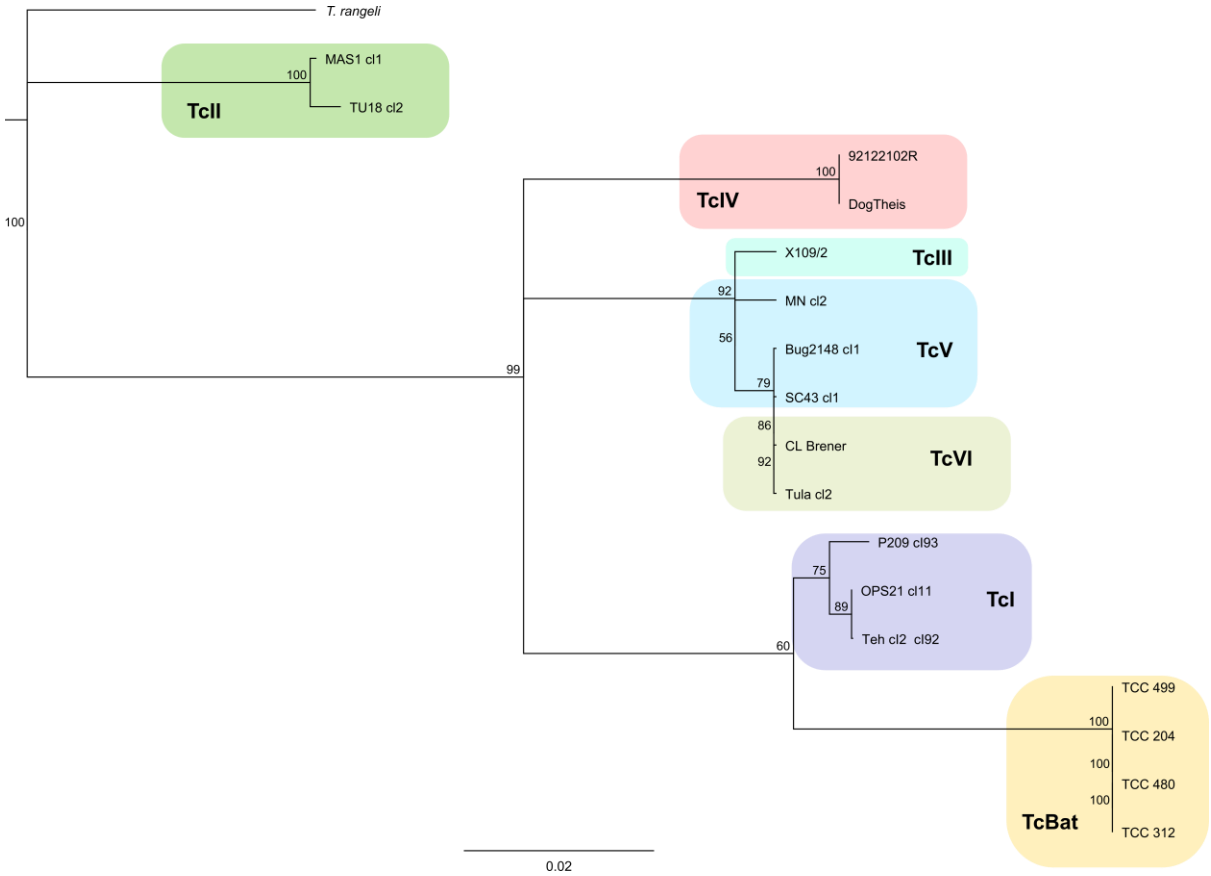

Figure 3. Phylogenetic tree of Trypanosoma cruzi based on cytochrome B sequences from 17 isolates (TcI – TcVI, and TcBat). The tree was constructed using Geneious Prime. The tree is rooted with *T. rangeli* as the output, and isolates are colour-coded by DTU. TcI (purple), TcII (dark green), TcIII (cyan), TcIV (red), TcV (blue), TcVI (light green), and TcBat (yellow). Full metadata and GenBank accession numbers for all strains are listed in

1.3. Flagellar Calcium Binding Protein, Tc24: A Therapeutic Target

Among the numerous *T. cruzi* proteins investigated as a therapeutic target, the 24 kDa flagellar calcium-binding protein (FCaBP), also known as Tc24 has consistently emerged as a promising candidate. This is largely due to its high conservation (~ 98%) across all *T. cruzi* DTUs and its prevalence in each morphological stage of the parasite life cycle, making it a valuable target for both the acute and chronic phases of infection (Garg and Tarleton, 1998; Versteeg et al.,

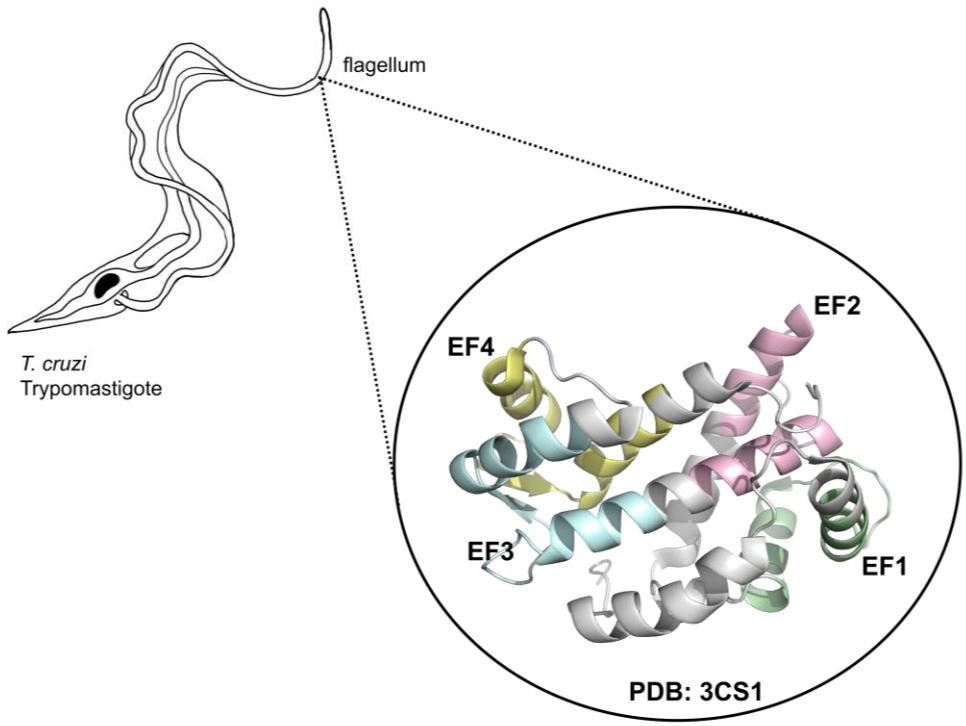

Figure 4. Schematic representation of the *T. cruzi* trypomastigote highlighting the flagellum, where the flagellar calcium-binding protein Tc24 is localised. The crystal structure of Tc24 (PDB: 3CS1) is shown with its four EF-hand motifs EF1 (green), EF2 (pink), EF3 (cyan) and EF4 (yellow). *Figure drawn by author.*

2021).

Although the precise biological role of Tc24 is not fully understood, it is thought to contribute to calcium-dependent processes such as parasite motility via the flagellum (Figure 4) (Versteeg et al., 2021). Additionally, Tc24 has been described as a B-cell superantigen that may facilitate immune evasion by deleting whole subsets of naïve B cells and thereby creating gaps in the antibody repertoire (Gunter et al., 2016). Therefore, inhibiting Tc24 could block the ability of

the parasite to evade the immune system while simultaneously interfering with the parasites motility, making it less able to infect and escape host cells.

Furthermore, Tc24 has been shown to be highly immunogenic and capable of inducing strong T-cell responses (Villanueva-Lizama et al., 2018). This is particularly significant given the ability of *T. cruzi* to cycle into dormant states; by promoting long-term immune surveillance, Tc24 could enable rapid T-cell activation upon the parasite 'reawakening'. Thus, impairing the parasite before it can re-establish high levels of parasitaemia.

1.4. Artificial Intelligence in Protein Design

To address the limitations of current therapies and the challenges of vaccine development, *de novo* driven protein design has emerged as a powerful new strategy. The word *"de novo"* is derived from Latin, meaning "anew" or "from the beginning", and in the context of protein design it means to generate entirly novel proteins that do not exist in nature.

Recently, Vázquez Torres et al., (2025) demonstrated that *de novo* proteins designed with RFdiffusion could successfully neutralise snake venom toxins. RFdiffusion is a deep-learning based model developed by Prof. Baker's laboratory at the University of Washington (USA). *De novo* binders are designed against a chosen target by dispersing a cloud of random unstructured residues "noise" near the target epitope. This 'noise' is gradually refined until a physically realistic and compact structure that fits the target epitope is designed (Watson et al., 2023). This structure then samples amino acids used ProteinMPNN (Dauparas et al., 2022) until a sequence that best fits the structure has been designed (Figure 5).

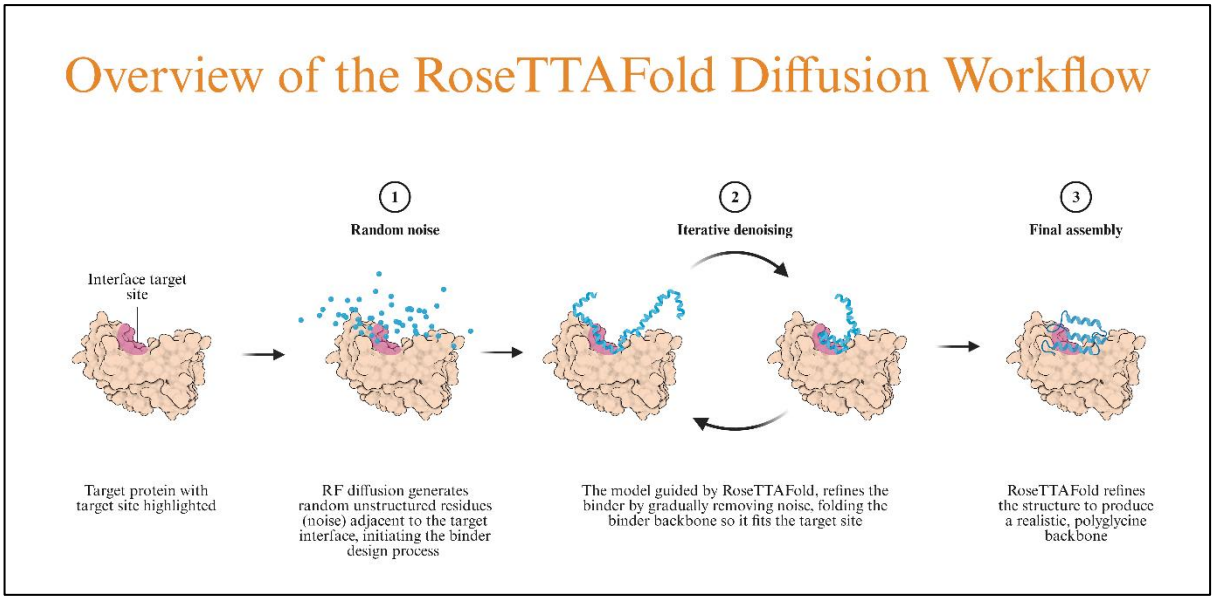

Figure 5. A schematic of the RF diffusion process to design de novo binders to a target protein. Figure generated using (BioRender, 2024).

These findings highlight the potential advantages of *de novo* approaches over traditional methods of therapeutic devlopment. In particular, *de novo* design eliminates the need for animal immunisation and the computational design aspect would allow the rapid, cost-effective generation of large libraries of candidate proteins that could be targeted to specific epitopes on a target antigen (Fox et al., 2025).

For these reasons we employed the use of RFdiffusion to design a panel of protein binders targeted t Tc24. This approach highlights the opportunity to apply deep-learning binder design to conserved antigens such as Tc24, where conventional methods of therapeutic design have so far been limited.

1.5. Scope of Thesis

This project investigates whether *de novo* binders designed using RFdiffusion can experimentally target Tc24, a highly conserved and immunogenic protein of *T. cruzi*. By combining deep learning methods with a recognised therapeutic candidate, this study seeks to explore a cost-effective approach to therapeutic design that could be applied to NTDs such as Chagas disease.

Specifically, the aim of this project is to assess whether a panel of six *de novo* binders designed by Dr Tim Jenkings, a collaborator of Campeotto's group at the Department of Biotechnology and Biomedicine at the Technical University of Denmark can be successfully expressed and shown to bind to Tc24.

Chapter 2

Materials and Methods

2.1. Materials

2.1.1. Bacterial strains

E. coli BL21(DE3) {F⁻*ompT hsdS*$_B$ (r_B^- m_B^-) *gal dcm* (DE3)} (Novagen) were used for the expression of AI binders (1 – 6) and Tc24 variant, Tx71 (full-length Tc24+His-tag).

E. coli BL21(DE3)-R3-pRARE2-BirA, a phage resistant derivative of BL21(DE3) carrying the pRARE2-BirA plasmid, which carries seven rare codon tRNAs and a BirA ligase were used for expression of Tc24 variant, Tx77 (full-length Tc24+AviTag).

2.1.2. Mammalian Cell Lines

Expi293F™ cells (ThermoFisher) human-derived embryonic kidney cell lines were used for transient transfection with plasmids encoding the nanobody and Tc24-Short (3CS1) see Section 2.3.3.

2.1.3. Expression Vectors

Codon–optimised sequences encoding the *de novo* protein binders (AI-1 to 6) and Tc24 variant Tx71 were synthesised and cloned by Twist Bioscience into the pET-15b expression vector (Novagen) and inserted between the *NdeI* and *BamHI* restriction sites (Table 1 and Table 3).

The NeuroBind nanobody was cloned into pHL-sec, between *AgeI* and *KpnI* (Aricescu et al., 2006). While Tc24-short(3CS1) was cloned into pET28a(+) expression vector. Cloning and DNA synthesis were performed by Twist Bioscience and a summary of the mammalian constructs provided in Table 2.

The pCDF-BirA plasmid (Keates et al., 2012) was used for co-transformation with pET15b-Tx77 into BL21(DE3)-R3-pRARE2-BirA (Table 3).

Table 1. Summary of RFdiffusion-designed AI binder constructs

Construct	Vector Backbone	Host System	Insert Length (bp)	Construct Length (bp)	N-terminal tag	Theoretical Protein	
						MW (Da)	pI
AI-1	pET-15b	*E. coli* BL21(DE3)	330	6021	6×His	12,903	4.50
AI-2	pET-15b	*E. coli* BL21(DE3)	363	6054	6×His	14,005	4.89
AI-3	pET-15b	*E. coli* BL21(DE3)	306	5997	6×His	12,222	5.13
AI-4	pET-15b	*E. coli* BL21(DE3)	306	5997	6×His	12,134	5.55
AI-5	pET-15b	*E. coli* BL21(DE3)	324	6015	6×His	12,285	5.24
AI-6	pET-15b	*E. coli* BL21(DE3)	336	6027	6×His	13,274	5.01

Table 2. Summary of mammalian expression constructs (nanobody and Tc24)

Construct	Vector Backbone	Host System	Insert Length (bp)	Construct Length (bp)	N-terminal tag	Theoretical Protein	
						MW (Da)	pI
pHL-sec-nAb-Neuro	pHL-sec	Expi293F™	711	7339	6×His	24,445	7.68
pET28-Tc24-Short(3CS1)	pET-28a(+)	Expi293F™	624	5993	6×His	24,896	5.30

Table 3. Tc24 variants and biotinylation system

Construct	Vector Backbone	Host System	Insert	N-terminal Tag	C-terminal Tag
pET15b-Tx71	pET-15b	*E. coli* BL21 (DE3)	Tx71	6×His	—
pET15b-Tx77 + pCDF-BirA + pRARE2-BirA	pET15b + pCDF-BirA + pRARE2	*E. coli* BL21(DE3)-R3-pRARE2-BirA	Tx77 + BirA	6×His	AviTag

2.2. In Silico Methods

2.2.1. De novo binder design using RFdiffusion

A panel comprising six *de novo* binders targeting Tc24 (PDB: 3CS1), were generated prior to this project by Dr Tim Jenkings, a collaborator of Campeotto's group at the Department of Biotechnology and Biomedicine at the University of Denmark, using RFdiffusion (Watson et al., 2023) in a two-step refinement.

In the first stage, RFdiffusion generated 1,200 backbone structures targeting Tc24. For each of these backbones, ProteinMPNN (Dauparas et al., 2022) generated two sequences per structure, yielding a total of 2,400 structural models. The resulting models were evaluated using AlphaFold2 (Jumper et al., 2021) and candidates filtered (pLDDT $\geq$ 90, interface PAE $\leq$ 11 Å) Based on these criteria, the top-ranking six binders were selected for re-sampling.

In the second stage, partial diffusion was employed to improve interface packing and overall structural stability. For each of the preliminary binders, 100 backbone conformations per binder were resampled, yielding 1,200 structural models. These were re-evaluated with AlphaFold2 under stricter criteria (pLDDT $\geq$ 90, and interface PAE $\leq$ 7 Å).

Based on these thresholds the top six candidates (AI-1to AI-6) were selected for subsequent downstream analysis as outlined within this thesis.

2.2.2. Multiple Sequence Alignment (MSA) and Clustering

A MSA of the top 50 *de novo* candidates were constructed in Geneious Prime (Biomatters, 2025) using MUSCLE (Edgar, 2004).

2.2.3. Dendrogram Generation

The MSA (Section 2.2.2) was used to build a Neighbour-Joining dendrogram without bootstrap resampling (Saitou & Nei, 1987). Tree images were produced directly in Geneious Prime.

2.2.4. Protein binding energy prediction (PRODIGY)

PRODIGY (Xue et al., 2016) was used to predict the binding affinity between the *de novo* binders (AI-1 to AI-6) and Tc24, using the AlphaFold2 structure. Interfacial contacts were defined as residues within a 5.5 Å distance cut-off.

2.3. Recombinant Protein Expression

2.3.1. Cell Transformation

Competent cells were thawed on ice before addition of plasmid DNA and incubated on ice for 30 minutes. The cells were heat shocked (42°C, 40 seconds) and immediately returned to ice for 2 minutes. After chilling, 180 μL of SOC medium was added and the cells allowed to recover (37°C, 1 hour, 180 rpm).

Cells were plated onto LB agar plates containing the required antibiotics (Table 4 and Table 5) and incubated overnight at 37°C. Plates exhibiting colony growth were stored at 4°C and used within 3 weeks. For co-transformation experiments, BL21(DE3)-R3-pRARE2-BirA cells were transformed simultaneously with pET15b-Tx77 and pCDF-BirA following the same procedure (Table 5).

Table 4. Summary of AI (1 – 6) plasmid transformations

Plasmid	*E. coli* Strain	Competent Cells (µL)	Plasmid DNA (ng)	Selection Plate
pET15b-AI-1	BL21(DE3)	20	2.45	LB + Ampicillin (100 µg/mL)
pET15b-AI-2	BL21(DE3)	20	3.25	LB + Ampicillin (100 µg/mL)
pET15b-AI-3	BL21(DE3)	20	4.6	LB + Ampicillin (100 µg/mL)
pET15b-AI-4	BL21(DE3)	20	5.6	LB + Ampicillin (100 µg/mL)
pET15b-AI-5	BL21(DE3)	20	65	LB + Ampicillin (100 µg/mL)
pET15b-AI-6	BL21(DE3)	20	77	LB + Ampicillin (100 µg/mL)

Table 5. Summary of Tx 77 co-transformation

Plasmid	*E. coli* Strain	Competent Cells (µL)	Plasmid DNA (ng)	Selection Plate
pCDF-BirA + pET15b-Tx77	BL21(DE3)-R3-pRARE2-BirA	25	pCDF-BirA: 100 pET15b-Tx77: 563	LB + Ampicillin (50 µg/mL) + Spectinomycin (50 µg/mL) + Chloramphenicol (34 µg/mL)

2.3.2. Bacterial Expression

For expression of the *de novo* binders and biotinylated constructs a single colony from transformation plates (Table 4 or Table 5) were inoculated into 20 mL of 2xYT media (Melford) supplemented with ampicillin (100 µg/mL) for *de novo* binders and (ampicillin 50 µg/mL, spectinomycin 50 µg/mL, and chloramphenicol 34 µg/mL) for co-transformations, and incubated overnight (37 °C, 180 rpm). Glycerol stocks were prepared by adding 0.5 mL of overnight cultures to 0.5 mL sterile glycerol and flash frozen in liquid nitrogen before storage at -80 °C.

For large-scale expression, 750 mL 2xYT containing ampicillin (100 µg/mL) for *de novo* binders and ampicillin 50 µg/mL and spectinomycin 50 µg/mL, for co-transformations was inoculated 1:50 with overnight culture and grown (37 °C, 180 rpm) until OD_{600nm} reached 0.6 – 0.9. Protein expression was induced with 0.5 mM IPTG, and incubated overnight (18 °C, 180 rpm). For biotinylated constructs, cultures were supplemented with biotin (0.4 mM) alongside IPTG.

Cells were harvested by centrifugation (5,000 × g, 15 min, 4 °C) and cell pellets lysed in 5 mL/g of wet pellet BugBuster® Protein Extraction Reagent (Merck), supplemented with cOmplete™ Protease Inhibitor cocktail, EDTA-free (Roche) and incubated at room temperature for 30 min with gentle agitation. Lysates were clarified by centrifugation (15,000 × g, 30 min, 4 °C) and the supernatant filtered through a 0.45 µm syringe filter (Merck).

2.3.3. Mammalian Expression

1 mL of Expi293F™ cells were thawed at room temperature and added to 25 mL Expi293F™ Expression Medium (Gibco™, ThermoFisher Scientific) in a 125 mL Erlenmeyer flask with 0.2 µm vented caps (Corning®, ThermoFisher Scientific), yielding a cell density of 0.5×10^6 cells/mL with > 98 % viability as determined by trypan blue staining. The cultures were propagated at 37 °C, in a 130 rpm, 5 % CO_2 humidified incubator. These conditions were maintained throughout the cell culturing process. Following 96 hours of growth, cells were reseeded into 75 mL of fresh expression medium and expanded until ~ 3.0 $x10^6$ cells/mL was reached. The expanded culture was split into two 125 mL Erlenmeyer flasks, 50 mL, dedicated for pHL-sec-nAb-Neuro expression and 40 mL for pET28-Tc24-Short(3CS1) expression.

In addition, a negative control containing just Expi293F™ cells in Expi293F™ Expression Medium were grown under identical conditions without plasmid transfection.

The propagated cells were transfected with 50 ng of plasmid DNA using ExpiFectamine™ 293 Reagent (ThermoFisher) in Opti-MEM™ Reduced Serum Medium, and complexes prepared according to the manufacturer's protocol. At 16–18 h post-transfection, Enhancers 1 and 2 were added, and cultures incubated for 7 days.

Supernatants containing the secreted protein were harvested by centrifuged (1,000 × g, 20 min, 4 °C) and 0.22 μm filtered and purified (See 2.4.1). Cell pellets and supernatant were collected for Day 4 and 7 post transfection and analysed via SDS-PAGE (See 2.5.1).

2.4. Protein Extraction and Purification

2.4.1. Ni^{2+} affinity purification

Prokaryotic or eukaryotic supernatants were loaded onto a pre-charged Ni^{2+}-NTA agarose resin pre-equilibrated with 10 CVs of Milli-Q water followed by 10 CVs 1× PBS, pH 7.4. The resin was incubated with the supernatant for 1 hour at 4°C with continuous mixing to allow binding of His-tagged proteins. After incubation, the resin was transferred back to the column, and the flow-through containing unbound proteins collected as (FT). The resin was washed with 10 CVs of wash buffer (1× PBS, pH 7.4, 35 mM imidazole), and the wash fractions collected as (W). Bound His-tagged proteins were eluted with 5 CVs of elution buffer (1× PBS, pH 7.4, 500 mM imidazole). The elution buffer was allowed to stand on the column for 10 minutes prior to collection as (E).

The protein was dialysed overnight at 4°C using a SnakeSkin™ dialysis membrane (Thermo Scientific) against 1 × PBS pH 7.4 at a protein: target buffer ratio of 1:100. Dialysed proteins were concentrated by centrifugation (3000 × *g*, 4 °C) to 300 µL for de novo binders (MWCO 3.5 kDa) or 2.5 mL for Tc24 variants (MWCO 10 kDa) using Amicon Ultra-15 Centrifugal Filter Units (Merck).

2.4.2. Size Exclusion Chromatography

Concentrated proteins were injected onto a Superdex™ S200 10/300 for *de novo* binders or S75 16/600 column (Cytiva) for Tc24 variants. The column was pre-equilibrated with 1× PBS, pH 7.4, mounted on an ÄKTA Purifier (Amersham Biosciences), which was operated at a flowrate of 0.5 mL/min with 0.5 mL fraction collections.

Elution was monitored by UV absorbance at 280 nm, and fractions corresponding to the main monomeric protein peak, collected and analysed by SDS-PAGE. Fractions confirmed to contain the target protein were pooled and concentrated to ~500 µL using an Amicon® Ultra-15 Centrifugal Filter (Merck) using the same MWCO in (section 2.4.2)

2.5. Protein Characterisation

2.5.1. SDS-PAGE

Protein samples were diluted in 1× PBS pH 7.4 and added to 4× Laemmli buffer (1:4). Samples were heated at 95°C for 5 minutes prior to gel loading. Gel electrophoresis was performed using a Bolt™ 4–12% Bis-Tris gel (Invitrogen™) with 20× Bolt™ MES SDS Running Buffer (Invitrogen™) diluted to 1×, at 180 V. Proteins were visualised using Quick Coomassie Stain (NeoBiotech) overnight, before destaining in Milli-Q water. Gels were imaged using an iBright™ Imaging System (Thermo Scientific).

2.5.2. Western Blot

Western blotting was performed according to the manufacturer's instructions using the Trans-Blot Turbo RTA Mini 0.2 µm Nitrocellulose Transfer Kit (Bio-Rad) to detect and confirm the presence of His-tagged proteins. Protein samples were resolved by SDS-PAGE (Section 2.5.1), with Maltose-binding protein fused to a C-terminal Spy-ag and 6×His-tag (MBP-Spy-His) was

used as a positive control. The transfer was run at 1.3 A, 25 V for 10 minutes using the Bio-Rad Trans-Blot® Turbo™ Transfer System.

After transfer, the PVDF membrane was blocked with 10 mL of blocking solution [5 % (w/v) skimmed milk powder, 1× PBS-T] and incubated for 1 hour at room temperature with gentle agitation. The solution was replaced with 10 mL fresh blocking solution supplemented with 1:3000 (v/v) dilution of anti-Penta-His HRP-conjugated antibody (Qiagen) and incubated for 1 hour on an orbital shaker.

Following antibody probing, the membrane was washed with 1× PBS-T (5 mL, 5 min) ×3. Excess buffer was removed, before the membrane was incubated for 5 minutes at room temperature with Pierce™ ECL Substrate (ThermoFisher) prepared according to the manufacturer's instructions. Protein bands were visualised using the iBright Imaging System (ThermoFisher).

2.6. Biophysical Assays

2.6.1. Bio-Layer Interferometry (BLI)

Kinetic binding measurements were performed on an Octet® R4 instrument (Sartorius). Prior to experiments, streptavidin biosensors (Sartorius) were hydrated in assay buffer [1× Kinetics Buffer, Sartorius] for at least 10 min. All measurements were carried out in a polypropylene 96-well plate (200 µL per well) at 30 °C with shaking at 1000 rpm.

The assay sequence was as follows: an initial baseline was established for 600 s in assay buffer, followed by ligand loading with 30 nM biotinylated Tc24 (Tx77) for 600 s. A short baseline was then measured for 60 s, followed by a second baseline of 30 s in assay buffer. Association and Dissociation with analytes were then monitored for 600 s at concentrations ranging from 0 nM to 1000 nM. Reference subtractions were performed using parallel biosensors incubated in buffer alone.

Chapter 3

Results

3.1. Computational Characterisation of AI-designed Tc24 Binders

3.1.1. Sequence diversity & representative selection (dendrogram)

RFdiffusion generated a diverse panel of *de novo* binders targeting Tc24. To assess how related the binder sequences were, a dendrogram was constructed. The six binders selected for expression and characterisation (AI-1 to AI-6, shown in blue) were distributed across multiple clusters rather than forming a single group, reflecting their underlying sequence diversity Figure 6.

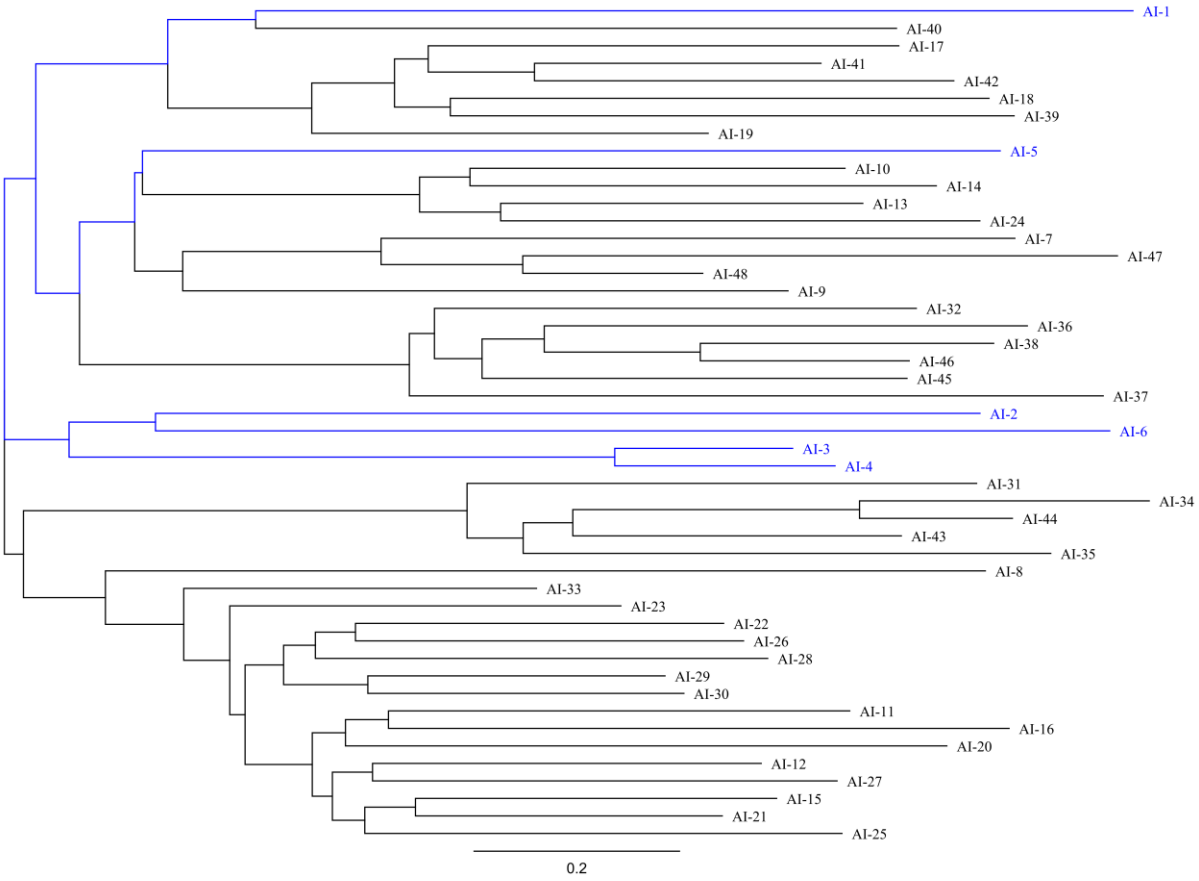

Figure 6. Dendrogram of *de novo* protein binders (AI-1 to AI-48) . Binders taken forward for expression and characterisation (AI-1 to AI-6) shown in blue.

3.2. AlphaFold2 Predicted structures

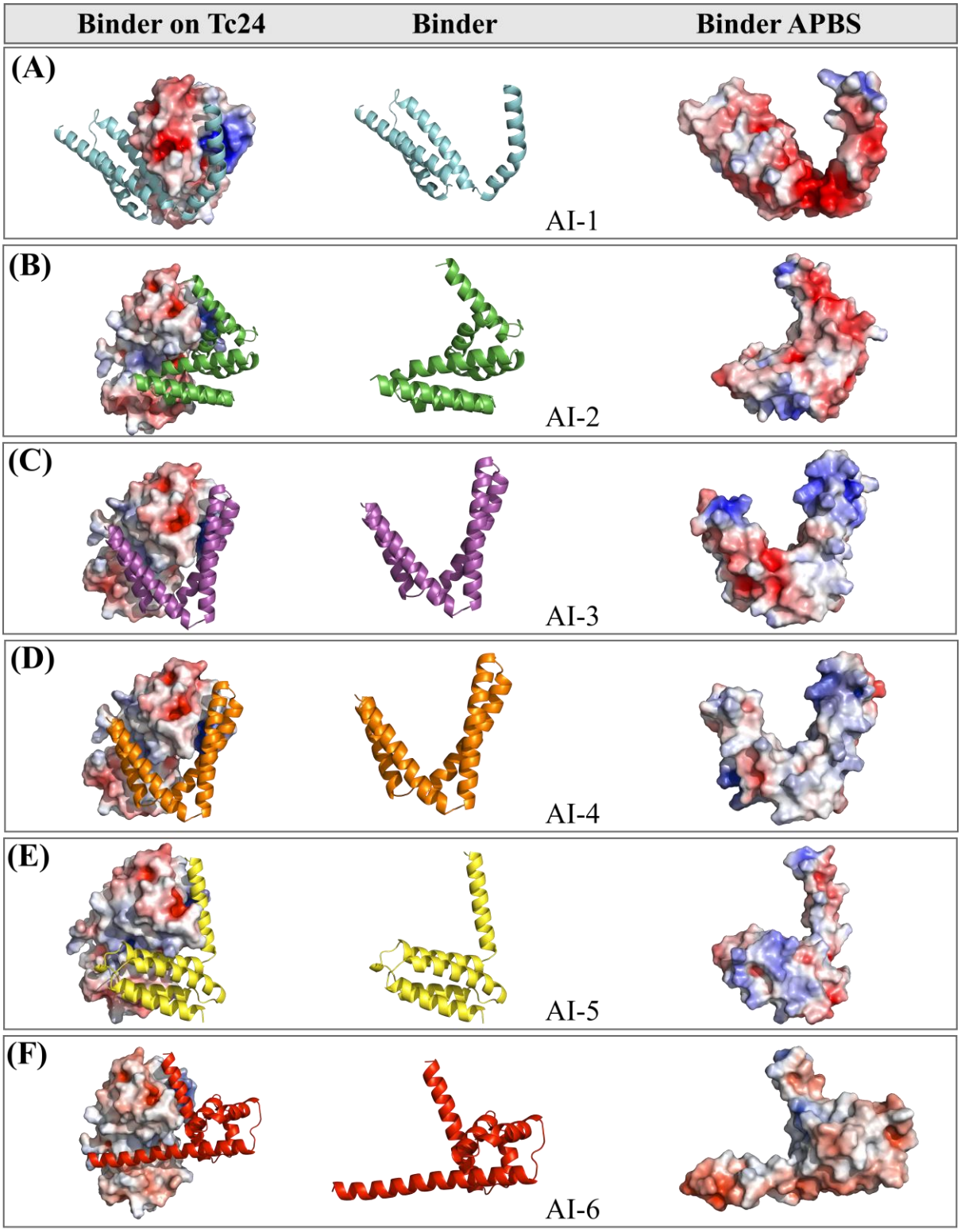

Figure 7. AlphaFold2 predicted structural models of *de novo* binders (AI-1 to AI-6) targeting Tc24.

Each row shows: (left) the binder docked on Tc24 (APBS surface representation), (middle) the binder (cartoon), and (right) the binder electrostatic surface (APBS –5 kT/e, red = negative, blue = positive). Binders are coloured consistently across views: **(A)** AI-1, **(B)** AI-2, **(C)** AI-3, **(D)** AI-4, **(E)** AI-5, **(F)** AI-6.

The AlphaFold2 modelling revealed that all six binders adopted open, extended conformations which resemble a 'clamp' (Figure 7). This structural architecture appears to enable each of the binders to partially envelop Tc24 and maximise interface contacts. Additionally, APBS electrostatic surfaces mapping of each of the binders further revealed differences in charge distribution, with AI-1 to AI-3 displaying large, positively charged patches which may indicate how RFdiffusion designed the binders to bind Tc24.

3.2.1. Hydrophobic Surface Analysis

Given that large exposed hydrophobic surfaces are often associated with poor solubility and aggregation in recombinant proteins, the surface hydrophobicity of each binder was analysed in Figure 8 using Kyte–Doolittle hydropathy mapping (Kyte & Doolittle, 1982). In all six binders, the largest hydrophobic patches (circled in red) were located within the predicted binding sites, indicating that the patches may contribute to Tc24/binder complex formation.

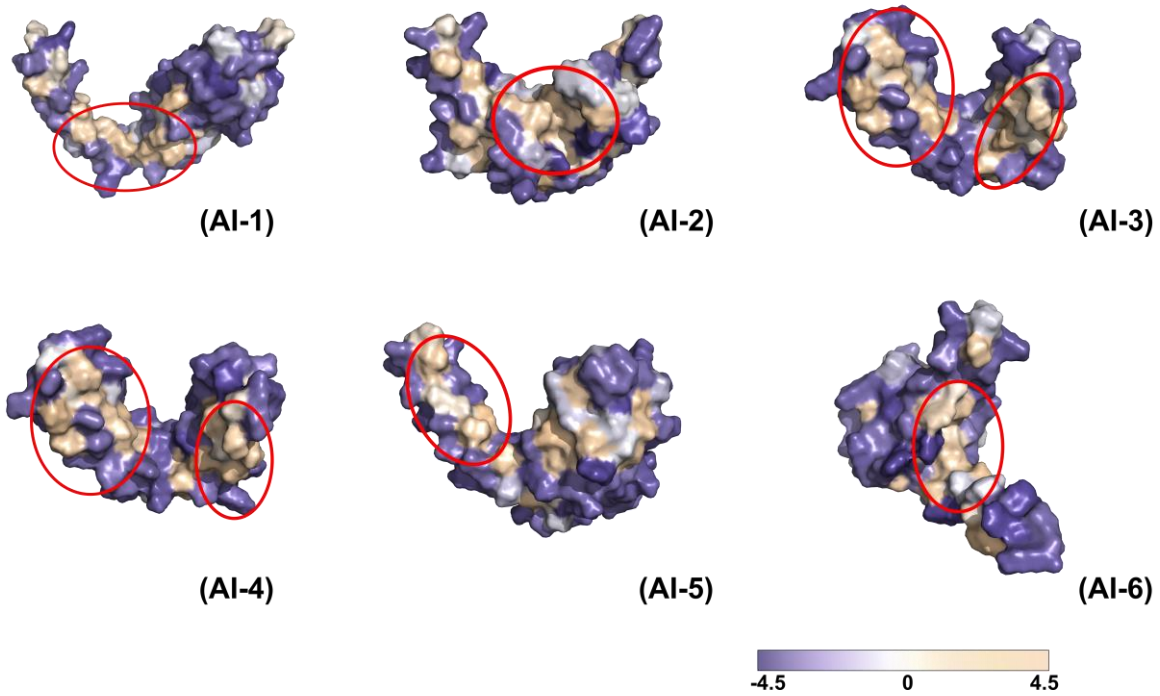

Figure 8. Kyte–Doolittle hydropathy surface maps of *de novo* binders AI-1 to AI-6. Surfaces are coloured according to the Kyte-Doolittle hydropathy index (-4.5, purple = most hydrophilic; 4.5, beige = most hydrophobic) The largest exposed hydrophobic patches for each binder are highlighted with red circles.

Surface Accessible Solvent Area (SASA) analysis revealed that the proportion of surface exposed hydrophobic residues ranged from 17–31% across the six binders (Table 6). AI-1, 3 and 4 exhibited the largest contiguous hydrophobic patches, accounting for ~8 % of their total SASA, whereas AI-5 revealed smaller patches. These findings were consistent with Kyte–Doolittle surface maps (Figure 8), which highlighted extended exposed hydrophobic regions in AI-3 and AI-4 compared to the more diffuse patches seen in AI-5 and AI-6.

Table 6. Surface Accessible Solvent Area (SASA) of Hydrophobic regions across *de novo* binders

Binder	Total SASA (Å^2)	Total Hydrophobic SASA (Å^2)	Total Hydrophobic Surface (%)	Largest Visualised Hydrophobic Patch SASA (Å^2)	Largest Patch % (of Total SASA)
AI-1	8,283	2,569	31.0	676	8.2
AI-2	8,106	1,925	23.7	501	6.2
AI-3	8,069	1,455	18.0	680	8.4
AI-4	8,042	1,419	17.6	690	8.6
AI-5	7,788	1,840	23.6	206	2.6
AI-6	8,280	1,782	21.5	415	5.0

3.3. Predicted AI binder Tc24 Binder Interface

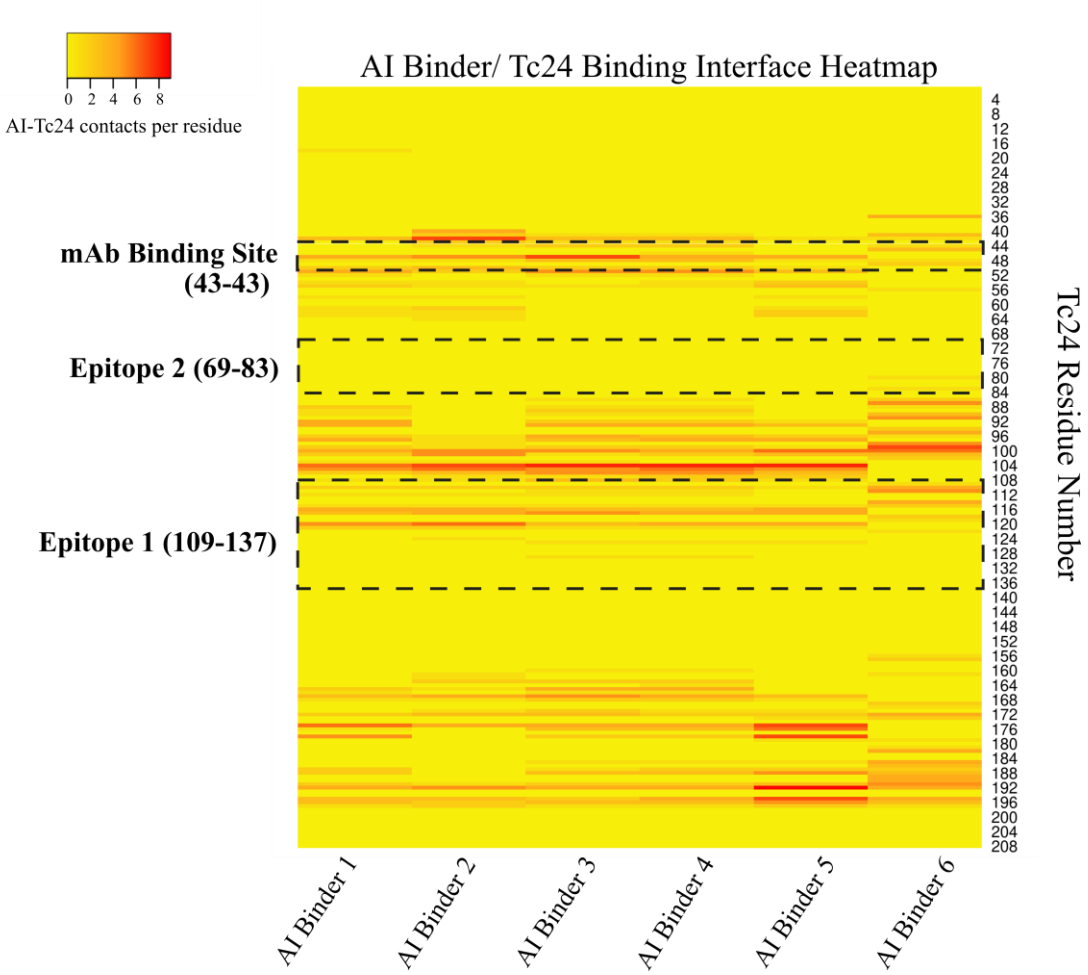

Figure 9. Heatmap showing the predicted binding interface between AI-designed binders (AI-1 to AI-6) and Tc24. The colour scale represents the number of AI binder–Tc24 residue contacts per position (yellow = few contacts, red = multiple contacts). Black dashed lines indicate key functional regions on Tc24, including the mapped monoclonal antibody (mAb) binding site (residues 43 – 49) and two known epitopes (Epitope 2, residues 69–83; Epitope 1, residues 109–137) (Dumonteil & Herrera, 2025).

To predict binding interfaces between Tc24 and the six *de novo* binders, PRODIGY was used to calculate residue–residue contacts at each complex interface (see 2.2.4). Tc24 contact residues were visualised for each binder using Heatmapper (Babicki et al., 2016) and compared with reported Tc24 epitopes, epitope 1 (residues 109–137) and epitope 2 (residues 69–83) (Dumonteil & Herrera, 2025). The binders predominantly targeted epitope 1 (Figure 9).

In addition to Tc24 epitopes, the mAb binding site (residues 43-39) (Versteeg et al., 2021) was also targeted by the binders, suggesting that the binders may compete with mAb binding. This overlap indicates the potential for the binders to be used in diagnostic applications.

3.4. Expression and purification of RFdiffusion designed *de novo* binders

3.4.1. Expression and Ni^{2+} Affinity Purification

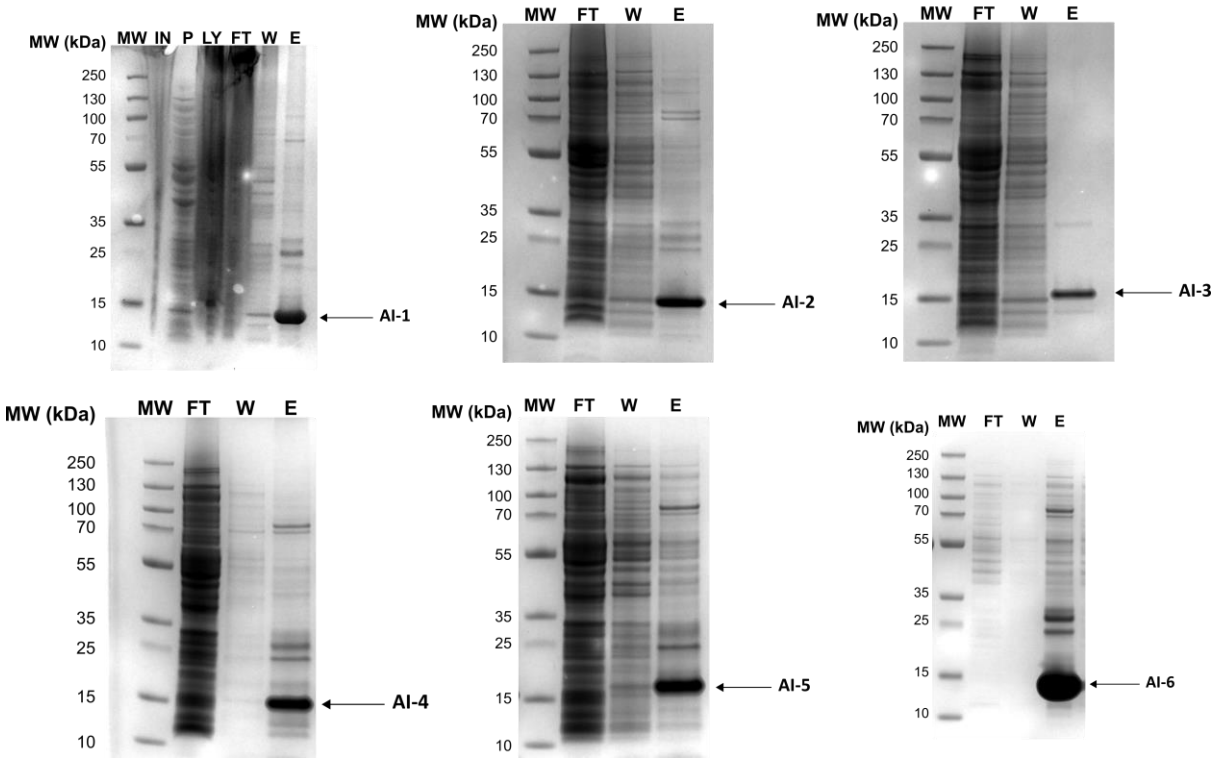

Figure 10. Ni^{2+} affinity purification of RFdiffusion-designed binders.

SDS-PAGE analysis of elution fractions from Ni^{2+} affinity chromatography of AI-2, AI-3, AI-4, AI-5, and AI-6 (lanes as labelled). A band at the expected molecular weight (~15 kDa) was observed for each construct, confirming successful expression and capture. Although the intensity of the bands varied, all binders could be recovered in soluble form.

All six binders (AI-1 to AI-6) were successfully expressed in *E. coli* BL21(DE3) and purified by Ni^{2+} affinity chromatography (see 2.3). SDS-PAGE confirmed a band at the expected molecular weight (~15 kDa) for all constructs, indicating successful expression and capture of His-tagged protein (Figure 10).

3.4.2. Gel Filtration

Following affinity purification, the *de novo* binders were further purified by SEC following the method outlined in section 1.1.1.

3.4.2.1. AI-1

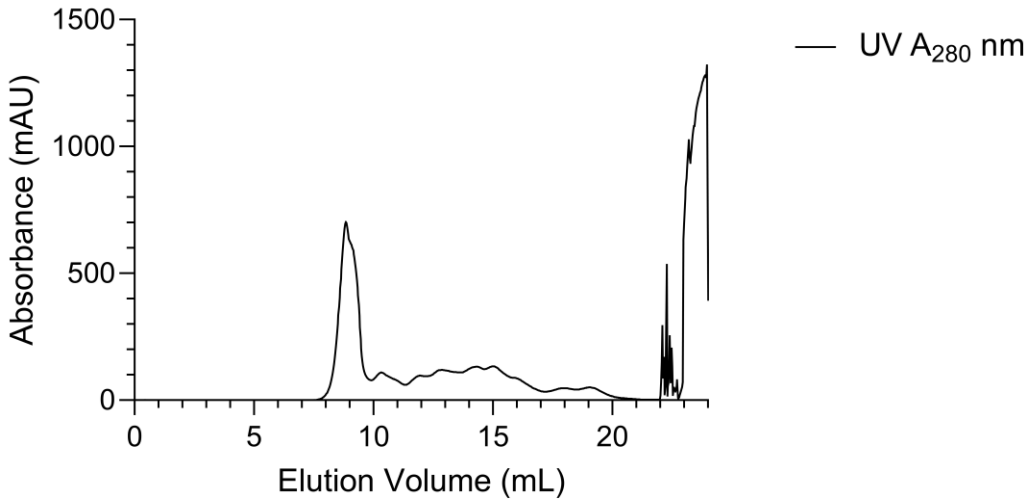

Figure 11. Size-exclusion chromatography of AI-1 on a Superdex 200 10/300 GL column. Elution was monitored by absorbance at 280_{nm}.

AI-1 affinity purified eluate was loaded onto the S200 10/300 GL at 0.861 mg (2.87 mg/mL at 300 µL). The chromatogram showed a dominant peak eluting at 9 mL, followed by a broad distribution of unresolved peaks (Figure 11). As the protein eluted close to the void volume, 8 mL, this suggests that AI-1 formed aggregates larger than the pore exclusion limit of the resin (~600 kDa). As a result, fractions were not collected, and AI-1 was not pursued for downstream characterisation.

3.4.2.2. AI-2

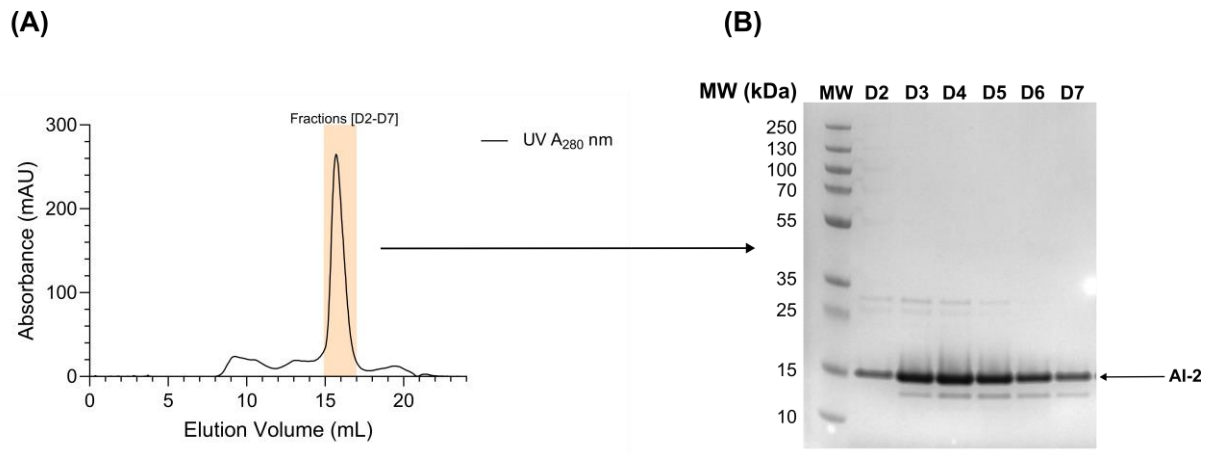

Figure 12. (A) Chromatogram of the purification of AI-2 by size-exclusion (Superdex 200 10/300 GL) showing a monodisperse peak at 15.5 mL. The shaded region (orange) indicates the pooled peak fractions (D2-D7) **(B)** SDS-PAGE gel of fractions D2- D7. The black arrow in the SDS-PAGE indicates the position of AI-2 at a molecular weight of ~15 kDa.

AI-2 affinity purified eluate was loaded onto the S200 10/300 GL at 1.695 mg (5.65 mg/mL at 300 µL). The chromatogram showed a monodisperse peak with a retention volume (V_r) of 15.5 mL (Figure 12A). Fractions spanning the peak were collected and analysed by SDS-PAGE, which revealed a prominent band at ~15 kDa, consistent with the expected size of AI-2 (Figure 12B).

However, while the bands correspond to the molecular weight of the binder, the retention volume of the peak was earlier than expected for a 15 kDa protein, with the manufacturer reporting an elution volume of ~19 – 20 mL for proteins of this size.

3.4.2.3. AI-3

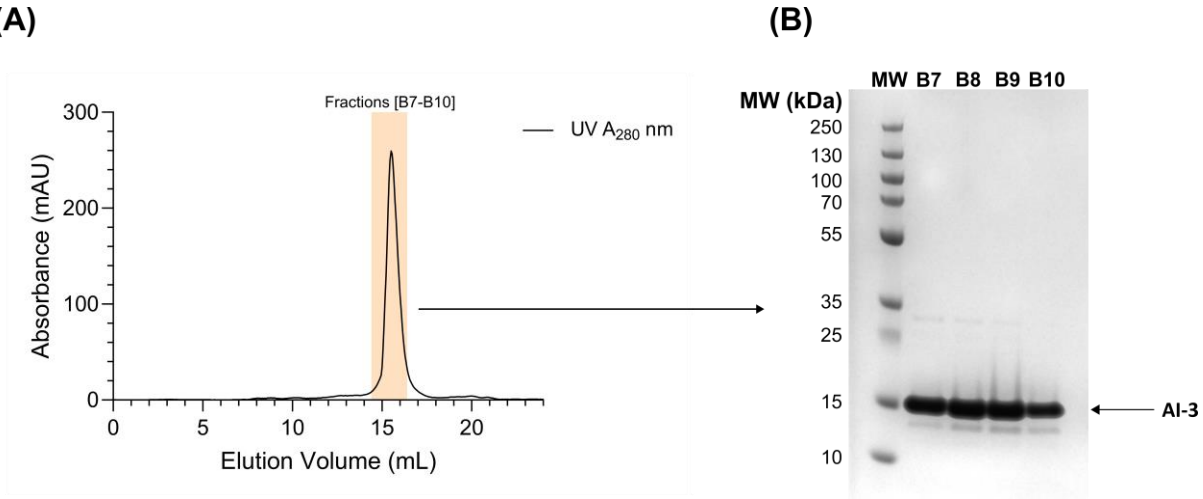

Figure 13. (A) Chromatogram of the purification of AI-3 by size-exclusion (Superdex 200 10/300 GL) showing a monodisperse peak at 15.5 mL. The shaded region (orange) indicates the pooled peak fractions (B7-B10) **(B)** SDS-PAGE gel of fractions B7 – B10. The black arrow in the SDS-PAGE indicates the position of AI-3 at a molecular weight of ~15 kDa.

AI-3 affinity purified eluate was loaded onto the S200 10/300 GL at 1.221 mg (4.07 mg/mL at 300 µL) and eluted as a single monodisperse peak with a V_r of 15.5 mL (Figure 13A). As observed for AI-2 (Figure 12A), the protein eluted earlier than expected for its size.

The fractions spanning the peak were analysed by SDS-PAGE for presence of the target protein (Figure 13B), which showed a band at 15 kDa which corresponded to the molecular weight of AI-3. Fractions B7-B10 were pooled and concentrated to ~11 mg/mL for subsequent characterisation and binding studies.

3.4.2.4. AI-4

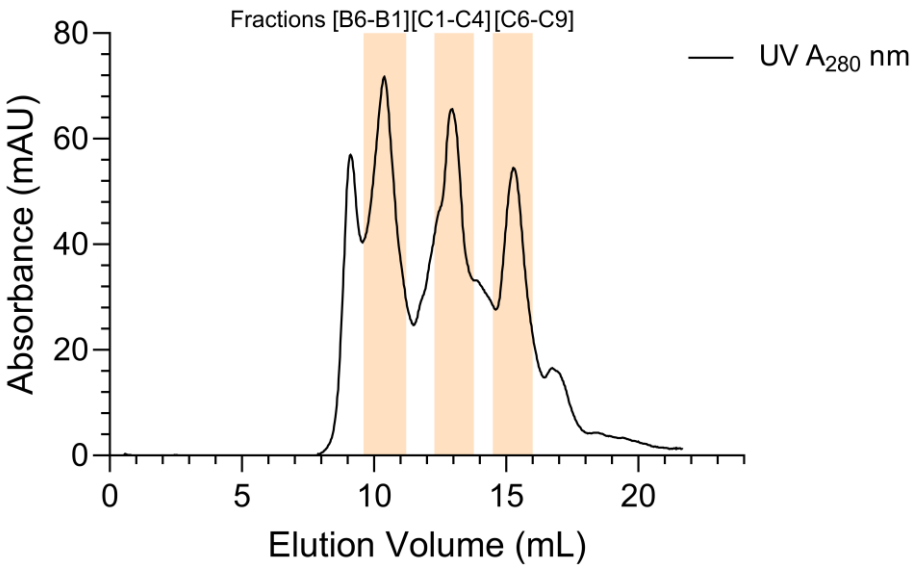

Figure 14. Chromatogram of the purification of AI-3 by size-exclusion (Superdex 200 10/300 GL) showing a monodisperse peak at 15.5 mL. The shaded region (orange) indicates the pooled peak fractions (B7-B10)

AI-4 affinity purified eluate was loaded onto the S200 10/300 GL at 0.984 mg (3.28 mg/mL, 300 µL). The chromatogram (Figure 14) showed the presence of multiple heterogeneous species within the sample. Fractions were taken from the three main peaks (highlighted in orange) for characterisation by SDS-PAGE and western blot to assess whether they corresponded to different oligomeric states of AI-4 (Figure 15).

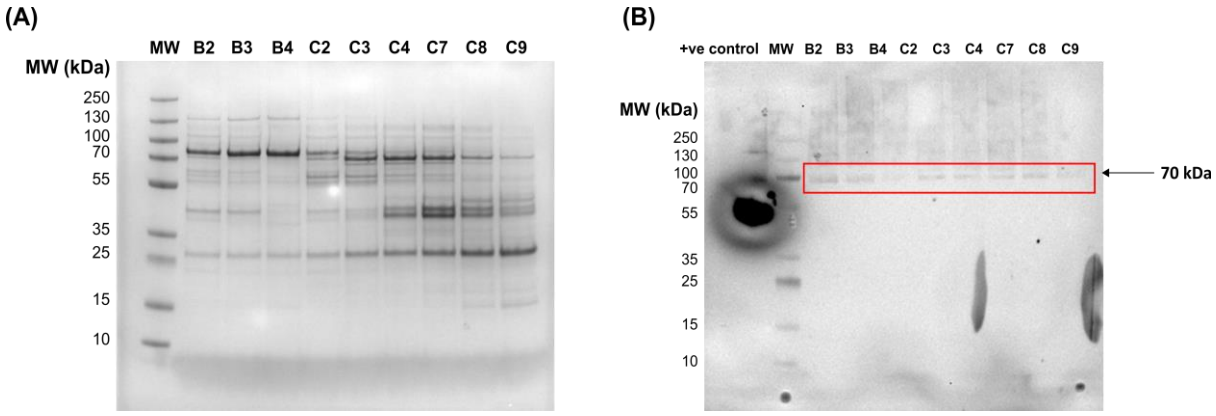

Figure 15. (A) SDS-PAGE of AI-4 peak fractions from peak 1 (B6 – B11), peak 2 (C2 – C4) and peak 3 (C7 – C9). **(B)** Western blot analysis of the same fractions as (A) show the presence of a 70 kDa (highlighted in red) in each of the fractions. MBP-Spy-His (55 kDa) was included as a positive control and the blot exposed for 5 minutes.

SDS-PAGE of the three peaks revealed the presence of multiple species of differing molecular weights (Figure 15A). Notably, there were no detectable bands at 15 kDa, which would correspond to the expected molecular weight of AI-4. Instead, prominent bands were observed between 30 - 80 kDa which suggest that AI-4 may have aggregated or formed higher order species.

To assess whether any his-tagged proteins were present, the same fractions were run on a western blot. Figure 15B showed the presence of a single band in each of the peak fractions at 70 kDa suggesting that AI-4 may have formed an oligomer, likely driven by its large exposed hydrophobic regions.

3.4.2.5. AI-5

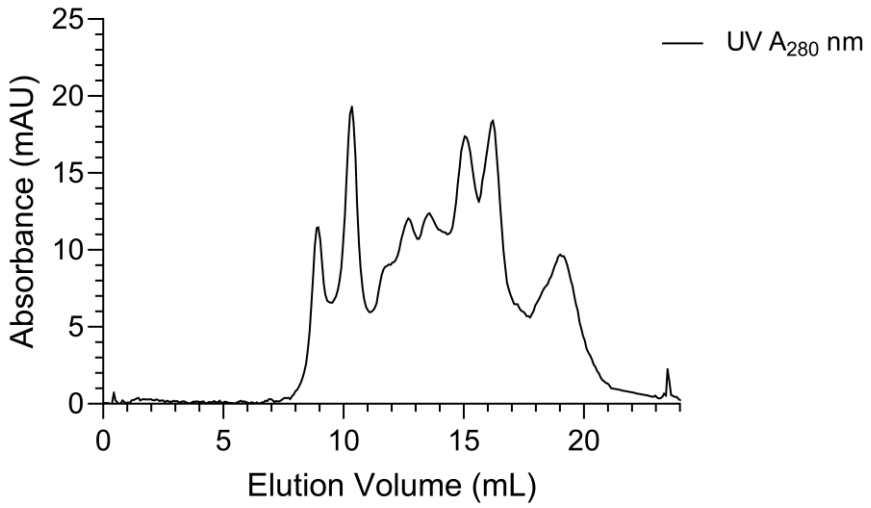

Figure 16. Chromatogram of AI-5 by SEC on a S200 10/300 GL column.

AI-5 affinity purified eluate was injected onto the (S200 10/300 GL) column at 0.69 mg (2.3 mg/mL, 300 µL). The chromatogram (Figure 16) showed the presence of multiple heterogeneous species within the sample. Due to the low absorbance at 280_{nm} collected fractions were of insufficient concentration to assess on an SDS-PAGE gel.

3.4.2.6. AI-6

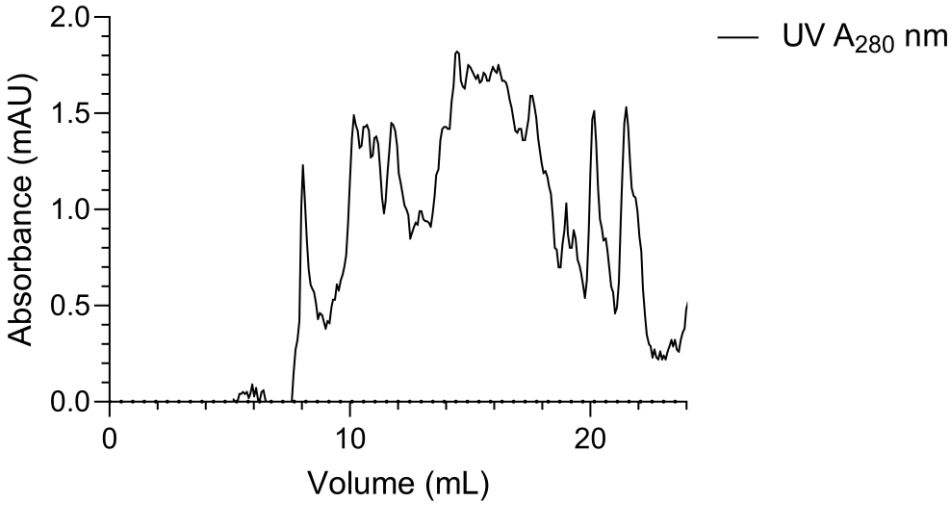

Figure 17. Chromatogram of AI-5 by SEC on a S200 10/300 GL column.

AI-6 affinity-purified eluate was loaded onto the Superdex 200 10/300 GL column at 0.696 mg total protein (2.32 mg/mL, 300 µL injection volume). The chromatogram (Figure 17) showed multiple overlapping peaks with no clear monodisperse species, indicating that AI-6 was present in a heterogeneous mixture. Compared to AI-5, the absorbance profile of AI-6 was low, with peak intensities not exceeding 2 mAU. As with AI-5, the collected fractions were too dilute to permit further analysis by SDS-PAGE.

3.5. Expression and Purification of Tc24 Variants

3.5.1. Expression and Purification of Tx77 (Full-length Tc24 with AviTag)

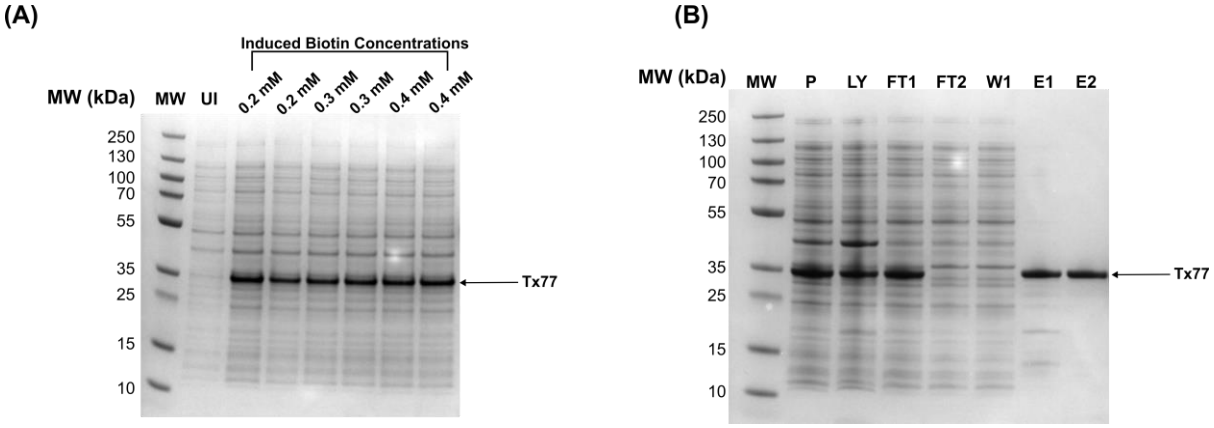

Figure 18. (A) SDS-PAGE gel of Tx77 expression at varying biotin concentrations (0.2 mM – 0.4 mM). The arrow indicates the position of Tx77 at ~ 35 kDa present in all samples but absent in the uninduced (UI) control. **(B)** SDS-PAGE analysis of 0.4 mM biotinylated Tx77 following Ni^{2+}-NTA purification. Lanes show pellet (P) and lysate (LY) after cell lysis and centrifugation, flowthrough (FT1, FT2), wash fractions (W1), and elution fractions (E1, E2). Tx77 is visible in the elution fractions at ~30 kDa (arrow).

An initial batch of Tx77 supplemented with 0.5 mM biotin resulted in culture loss, prompting expression trials at lower biotin concentrations (0.2 – 0.4 mM) (Figure 18A). As expression was consistent across 0.2 – 0.4 mM biotin, 0.4 mM biotinylated Tx77 was selected for subsequent purification. The highest biotin concentration was selected as it provided the best chance of achieving sufficient biotinylation of Tx77, since biotinylation levels were not directly quantified.

SDS-PAGE analysis of Ni^{2+}-NTA purification of 0.4 mM biotinylated Tx77 confirmed the presence of the protein at ~35 kDa in the elution fractions (E1 and E2) in Figure 18B. The elution fractions were pooled and concentrated to 8.77 mg/mL.

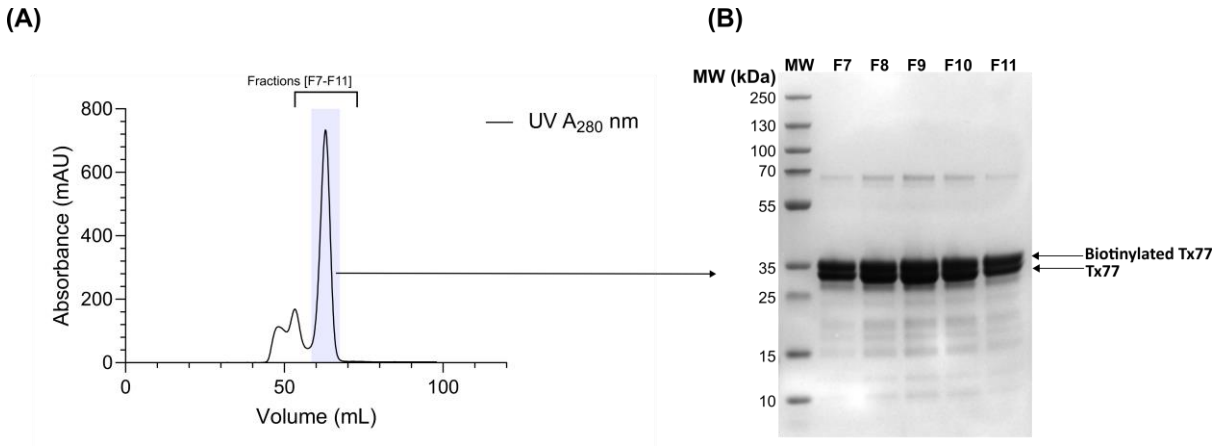

Figure 19. (A) Size-exclusion chromatogram of Tx77 purification (S75 16/600 GL) showing a dominant species at V_r 63 mL **(B)** SDS-PAGE gel of the elution fractions (F7-F11) spanning the monodisperse peak shaded in purple as seen in the chromatogram. The black arrow on the SDS-PAGE gel indicates the position of two bands in close proximity representing corresponding to Tx77 and its biotinylated form at an approximate molecular weight of 35 kDa.

2.2 mL of the protein at 8.77 mg/ mL (19.3 mg total protein) was injected onto the SEC column. Tx77 eluted as a monodisperse peak with a V_r of 63 mL (Figure 19A). SDS-PAGE confirmed the presence of Tx77 at ~35 kDa within the peak fractions (Figure 19B). The main peak fractions (F7 – F11) were pooled together and concentrated to 15.77 mg/mL for binding characterisation by bio-layer interferometry with the *de novo* proteins (AI-1 to AI-6).

3.5.2. Expression and Purification of Tx71 (Full-length Tc24 with His-Tag)

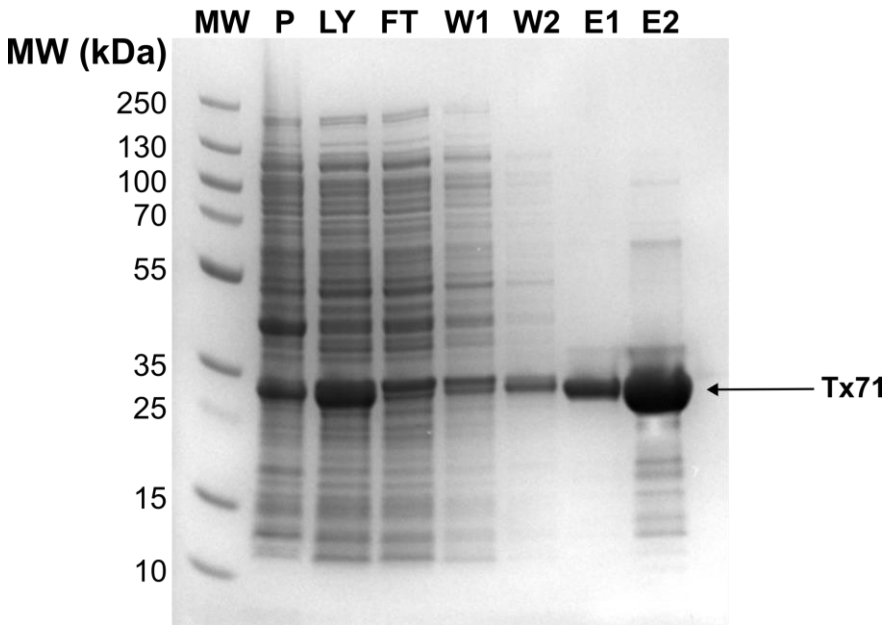

Figure 20. SDS-PAGE showing the purification of Tx71 by Ni^{2+}-NTA. A sample of the Pellet (P) and Lysate (LY) after cell lysis and centrifugation, flow-through (FT) of unbound proteins by Ni^{2+}-NTA, two washing steps of the resin (W1 and W2), and first and second elution steps (E1 and E2) were loaded. The black arrow indicates the position of Tx71, at an approximate molecular weight of 30 kDa.

Tx71 was expressed as a His-tagged protein and purified by Ni^{2+} affinity chromatography followed by size-exclusion (see 2.3.2). Aliquots of the insoluble pellet and soluble supernatant after centrifugation, as well as the flowthrough, wash, and elution fractions, were analysed by SDS-PAGE (Figure 20). A band at ~30 kDa, corresponds to Tx71 was identified in the elution fractions (E1 and E2), confirming successful capture of Tx71. The eluted protein was pooled and concentrated to 14 mg/ mL.

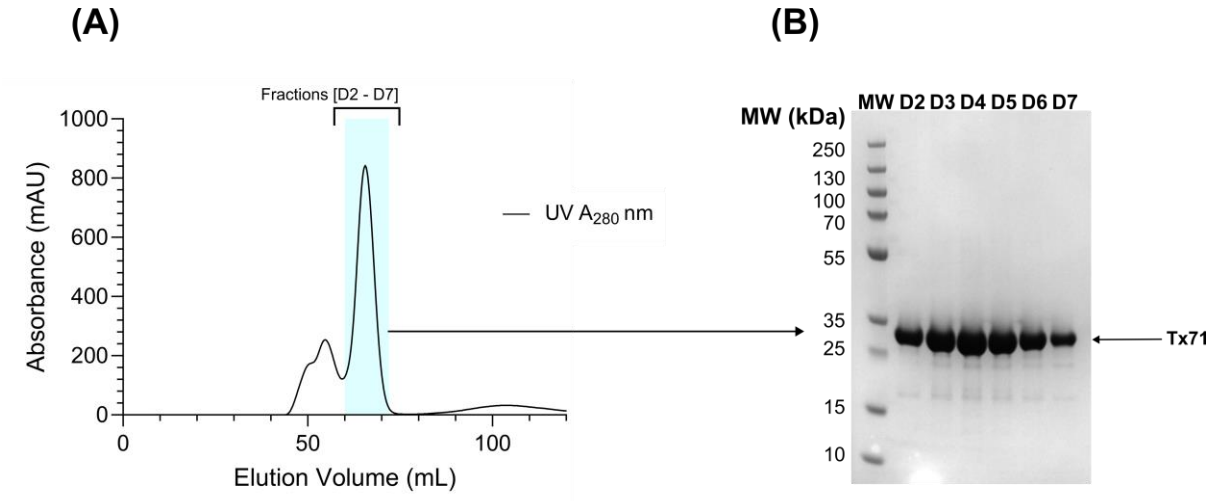

Figure 21. (A) Size-exclusion chromatogram of Tx71 purification (S75 16/600 GL) showing a dominant species at V_r 55 mL **(B)** SDS-PAGE gel of the elution fractions (D2-D7) spanning the monodisperse peak shaded in blue as seen in the chromatogram. The black arrow in the SDS-PAGE gel indicates the position of Tx71 at an approximate molecular weight of 30 kDa.

2.5 mL of the protein at 14 mg/ mL (35 mg total protein) was injected onto the SEC column. Tx71 eluted as a monodisperse peak with a V_r of 55 mL (Figure 21A). SDS-PAGE confirmed the presence of Tx71 at ~30 kDa within the peak fractions (Figure 21B). The main peak fractions (D2-D7) were pooled together and concentrated to 2.27 mg/mL for binding characterisation studies with the de novo proteins (AI-1 to AI-6).

3.6. Binding characterisation between de novo binders and Tc24

3.6.1. SEC evaluation of AI-2 and Tx71 complex formation

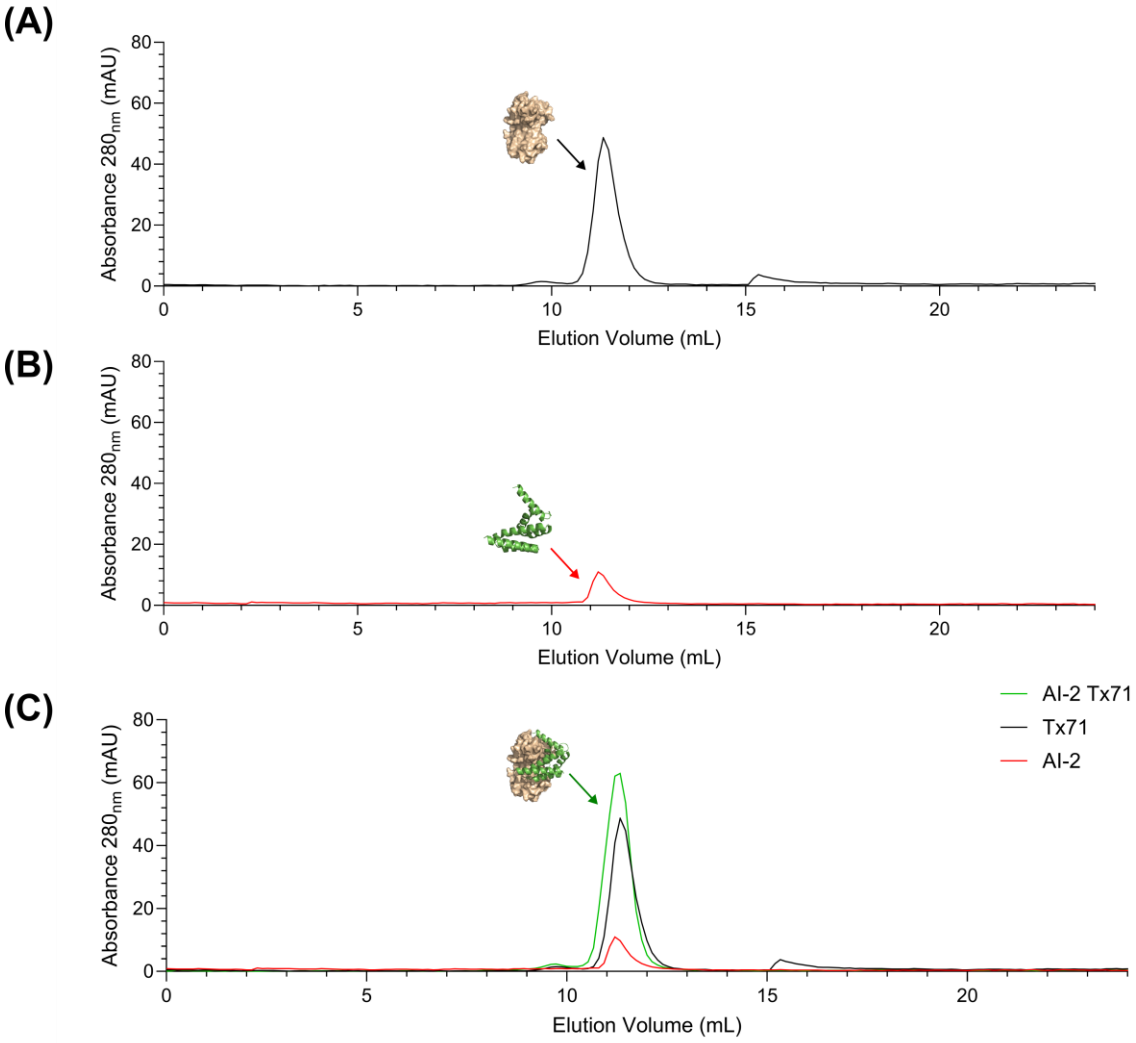

Figure 22. SEC profiles of **(A)** Tx71, **(B)** AI-2, and **(C)** Overlay of AI-2 incubated at 1:1 stoichiometry with Tx71 (green), AI-2 (red) and Tx71 (black). Cartoon of binder, antigen and binder-antigen complexes are shown on top of each peak.

To assess whether AI-2 forms a stable complex with Tx71, the two proteins were incubated for 30 minutes at equimolar concentrations of 20 µM (1:1 stoichiometry) prior to injection on a SEC column (S75 10/300 GL). For comparison, Tx71 and AI-2 were each analysed individually under the same conditions as shown in Figure 22A and B respectively.

Tx71 alone eluted as a single peak at ~11.5 mL (Figure 22A), while AI-2 alone also a smaller, lower intensity peak at ~11.5 mL (Figure 22B). The similarity in V_r between AI-2 (~15 kDa) and Tx71 (~30 kDa) was unexpected as SEC separates molecules based on size and shape this indicates that AI-2 may dimerise or have a larger than expected hydrodynamic radius (r_h).

Following pre-incubation, the AI-2 + Tx71 mixture eluted as a single peak that overlapped with Tx71 and AI-2 alone (Figure 22C). As there was no detectable shift in V_r, it indicates that AI-2 did not form a stable complex with Tx71 under the conditions tested.

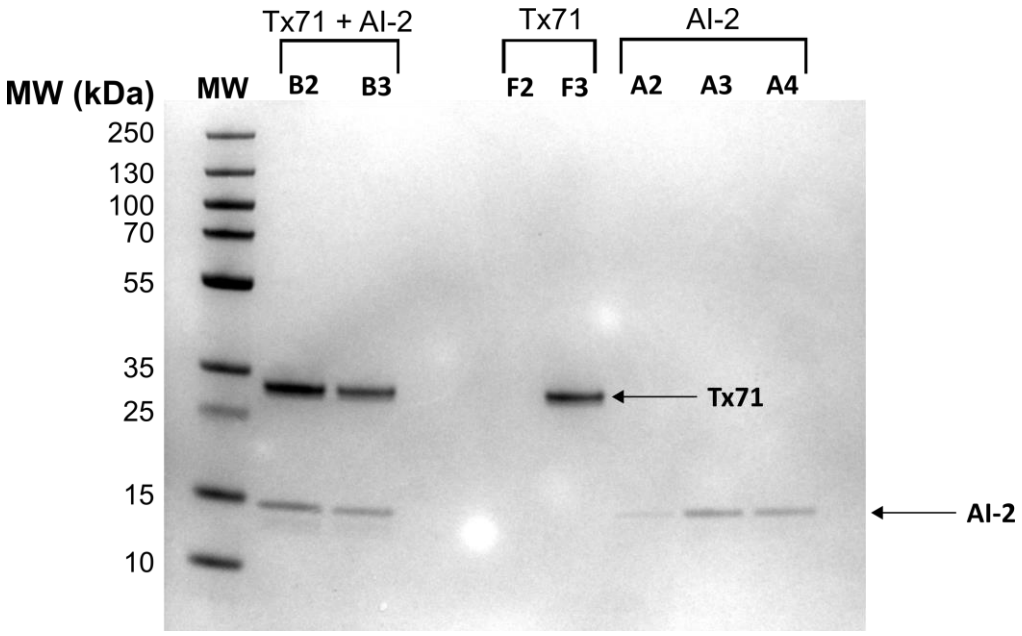

Figure 23. SDS-PAGE of peak fractions (AI-2, Tx71 and AI-2/Tx71 complex) from Figure **22**C. Two observable bands are at ~30 kDa and 15 kDa, which correspond to Tx71 and AI-2 respectively as indicated by the black arrows.

The collected fractions for each peak in Figure 22C were assessed by SDS-PAGE. The gel verified that the SEC peaks contained Tx71 (30 kDa) and AI-2 (15 kDa). Notably, the fractioned peak for AI-2 alone, showed a single band at its expected MW, further supporting that it may dimerise.

3.6.2. SEC evaluation of AI-3 and Tx71 complex formation

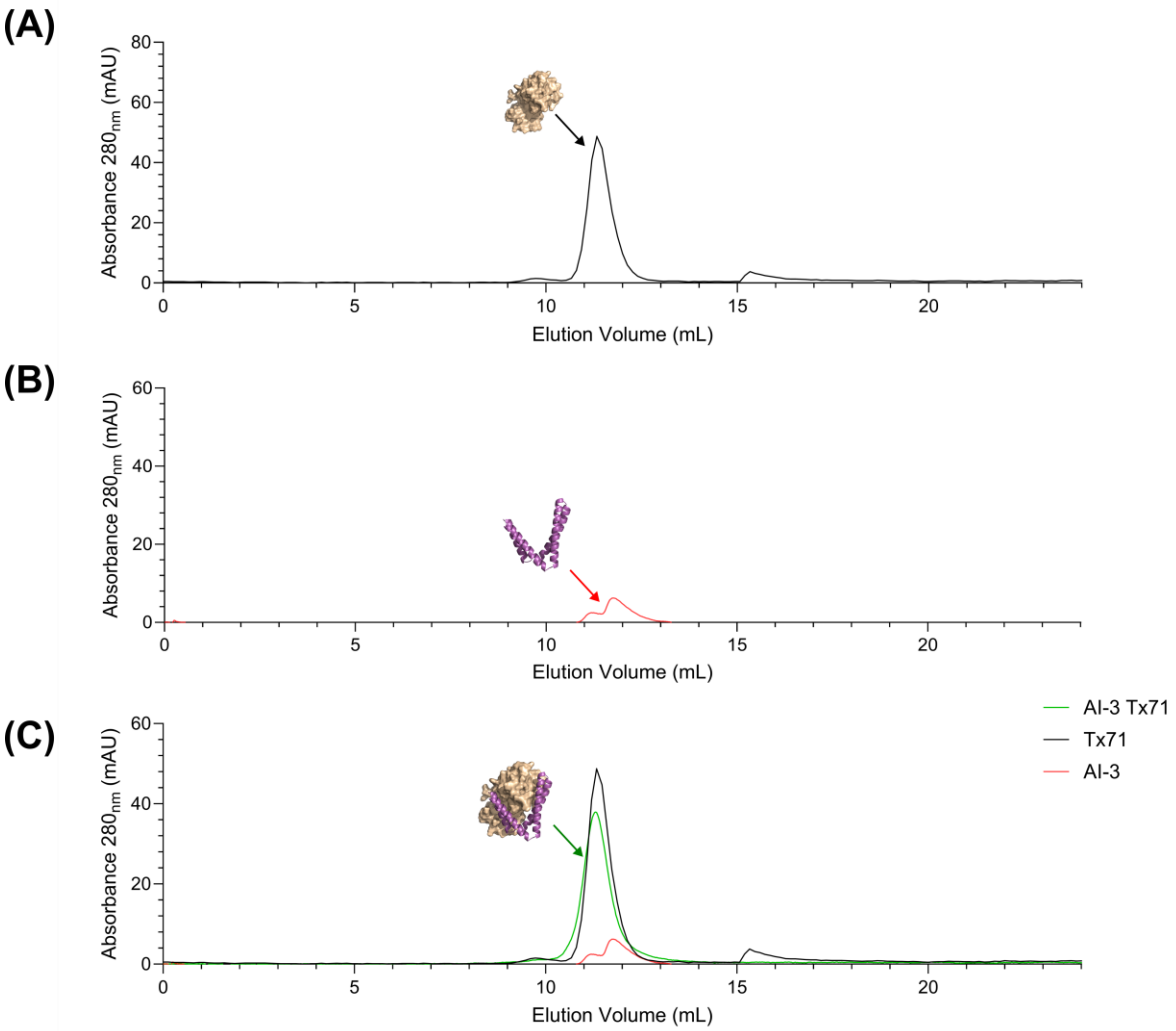

Figure 24. SEC profiles of **(A)** Tx71, **(B)** AI-3, and **(C)** Overlay of AI-3 incubated at 1:1 stoichiometry with Tx71 (green), AI-3 (red) and Tx71 (black). Cartoon of binder, antigen and binder-antigen complexes are shown on top of each peak.

SEC analysis showed that Tx71 alone eluted as a single peak at ~11.5 mL (Figure 24A), while AI-3 eluted later at ~12 mL (Figure 24B). When pre-incubated together, the AI-3 + Tx71 mixture produced a peak that overlapped with Tx71 alone (Figure 24C), indicating no significant shift in V_r and therefore no ascertainable evidence of stable complex formation between AI-3 and Tx71. Unlike AI-2, which eluted at a similar volume to Tx71 despite its smaller MW, AI-3 displayed a distinct elution profile at ~12 mL, suggesting that it does not self-associate or exhibit an enlarged r_h.

3.7. Kinetic binding analysis of AI-2 and AI-3 with Tx77 (full-length Tc24-AviTag)

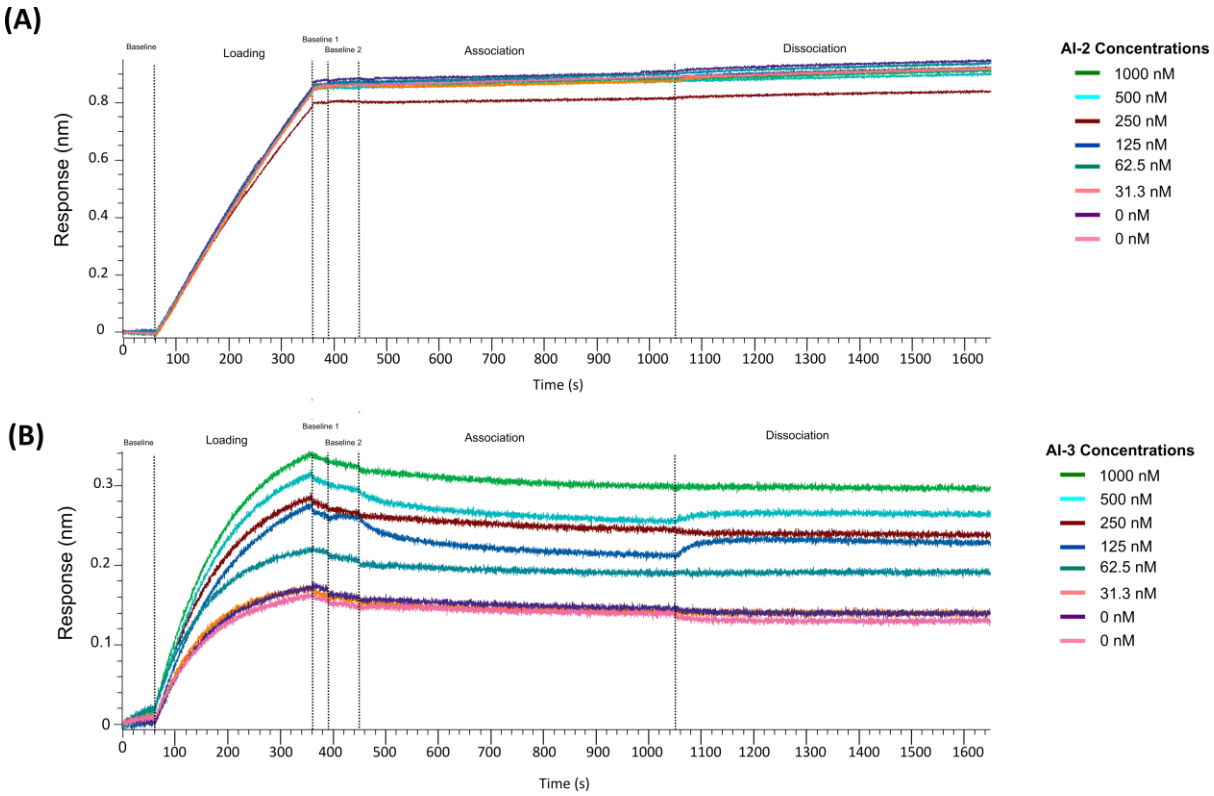

Figure 25. BLI of AI-2 and AI-3 serial dilutions (31.2 – 1000 nM) to 30 nM load of biotinylated Tx77 on **streptavidin biosensors (A)** Binding response of AI-2 to Tx77 **(B)** binding response of AI-3 to Tx77

To assess the binding of AI-2 and AI-3 to Tx77, BLI experiments were performed to quantify whether AI-2 and AI-3 bind to Tx77 and how strongly they associate and dissociate with it. For both AI-2 (Figure 25A) and AI-3 (Figure 25B) minimal change in response (nm) was observed during the association and dissociation phases. The absence of concentration-dependent binding signals indicates that neither AI-2 nor AI-3 exhibited any measurable interaction with Tx77 under the concentrations tested.

The incomplete saturation of the sensors during the loading step and minor variation in loading responses between AI-2 and AI-3 was observed, however, this doesn't affect the overall conclusion that no binding was observed.

3.8. Expression and purification of a NeuroBind-designed nanobody in mammalian cells

In addition to the RFdiffusion designed *de novo* binders, a nanobody was designed using NeuroBind to target an alternative face of Tc24 to assess whether a different epitope could be exploited for binding.

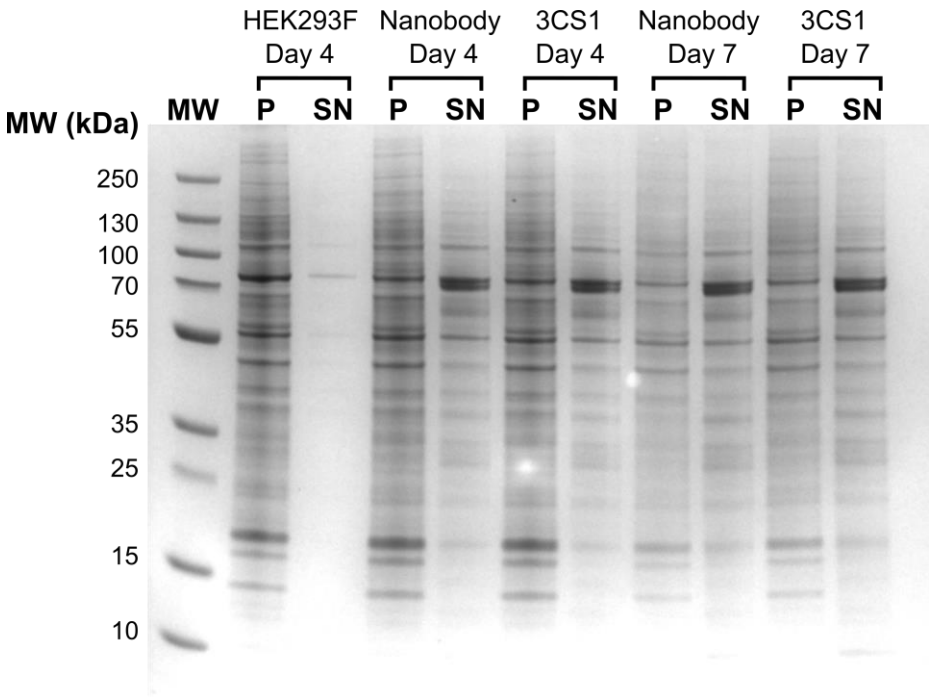

Figure 26. SDS-PAGE of pellets (P) and supernatant (SN) for negative control, Expi293F™ cells (HEK293F), and nanobody and 3CS1 (Tc24) on Day 4 and 7 post-transfection.

Both the nanobody and 3CS1 didn't show any distinct band corresponding to the expected molecular weight of the nanobody or 3CS1 (24 kDa) in either soluble or insoluble fractions.

The supernatant for 3CS1 and nanobody at 7 days post transfection were purified by Ni^{2+}-NTA as outlined in section 2.4.1 and assessed via SDS-PAGE (Figure 27).

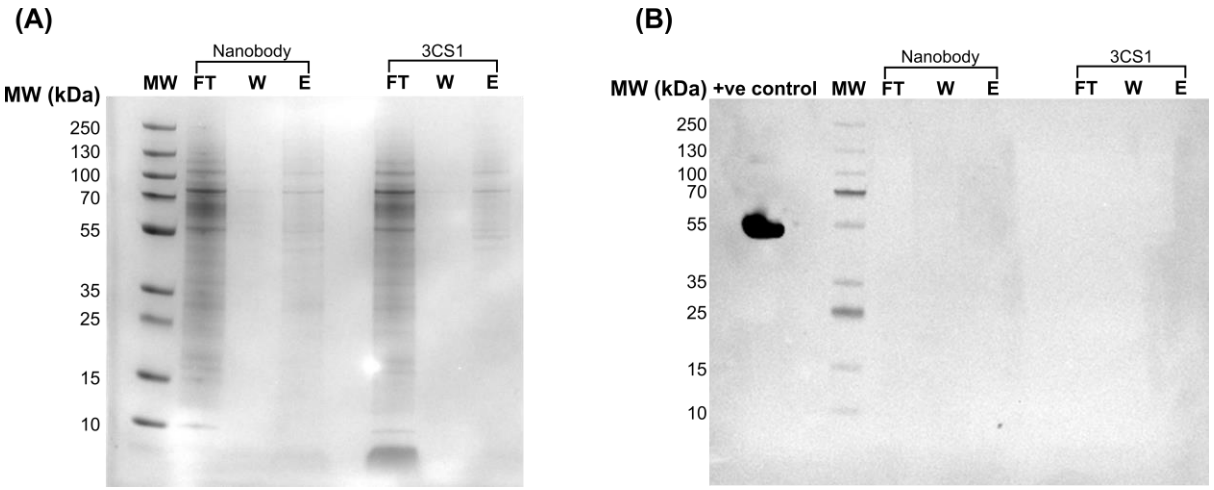

Figure 27. (A) SDS-PAGE analysis of Ni^{2+}-affinity purified nanobody and Tc24 (3CS1). Fractions shown are flow-through (FT), wash (W), and elution (E). **(B)** Western blot of the same samples using an anti-His antibody. The positive control is MBP-Spy-His is observed at 5 kDa. No clear band corresponding to the expected size of the nanobody or Tc24 (24 kDa) was detected in the elution fractions, indicating unsuccessful transfcetion of cells.

To assess whether the NeuroBind-designed nanobody and Tc24 (3CS1) were successfully expressed and purified, Ni^{2+}-affinity chromatography was performed on culture supernatants harvested seven days post-transfection. SDS-PAGE analysis of the flow-through, wash, and elution fractions revealed no distinct band at the expected molecular weights of the nanobody (~24 kDa) or Tc24 (~20 kDa) (Figure 27A). Western blotting with an anti-His antibody confirmed the absence of detectable signal in the elution fractions, while the positive control was successfully detected (Figure 27B). These results indicate that neither construct was expressed or secreted at detectable levels under the conditions tested.

Chapter 4

Discussion

4.1. RFdiffusion Binders

The aim of this project was to experimentally validate a panel of six de novo binders designed using RFdiffusion against Tc24, a highly conserved therapeutic target of *Trypanosoma cruzi*. While all six binders were successfully expressed in *E. coli* only AI-2 and AI-3 could be recovered as a monodisperse species for downstream analysis. These two candidates expressed well and displayed minimal aggregation during purification; however, neither demonstrated measurable binding to Tc24 in SEC, (Figure 22 and Figure 24) or BLI (Figure 25). While these findings were not the expected outcome, several explanations can be considered.

4.2. AI-2

SEC analysis of AI-2 (Figure 22) revealed that, despite its relatively small molecular weight (15 kDa), it unusually eluted at the same retention volume as Tx71, a 30 kDa Tc24 variant. SDS-PAGE of the corresponding fractions (Figure 23) confirmed that AI-2 was present at its expected MW, suggesting that AI-2 may self-associate in solution, thereby increasing its hydrodynamic radius and eluting earlier.

This interpretation is consistent with Kyte–Doolittle hydropathy analysis (Figure 8), which identified two large contiguous hydrophobic surface patches spanning the binding interface on AI-2. Such surface exposed hydrophobic regions are known drivers of self-association and may provide a plausible explanation for the discrepancies in elution profiles.

4.3. AI-3

AI-3 displayed similar elution behaviour to AI-2. Despite also being a 15 kDa protein it eluted at the same retention volume as AI-2 and Tx71 (Figure 24). Structural analysis of the predicted AI-3 structures showed comparable hydrophobic patches to AI-2 (Figure 8), supporting the hypothesis that AI-3 may also self-associate. A logical next step to confirm whether AI-2 and AI-3 are forming oligomers would be to perform analytical ultracentrifugation (AUC)**,** which allows direct measurement of molecular weight and sedimentation behaviour in native conditions. This would confirm whether AI-2 and AI-3 exist as monomers, dimers, or a mixture of oligomeric states, and would therefore clarify whether the anomalous SEC profiles reflect self-association or whether the binders have a larger than expected hydrodynamic radius.

4.4. Other binders: AI-1, AI-4, AI-5, and AI-6

The remaining binders were not suitable for downstream analysis due to instability and aggregation AI-1 eluted in the column void volume (Figure 11), consistent with very large aggregates, and could not be recovered as a defined species. Surface electrostatic mapping of AI-1 in Figure 7 showed that there are large regions of positively charged residues which may be influencing aggregation.

AI-4 produced multiple overlapping peaks, and while SDS-PAGE revealed protein species between 30 and 80 kDa, no band was present at the expected 15 kDa size (Figure 15). Western blotting further detected a consistent ~70 kDa band across all fractions, strongly suggesting that AI-4 formed higher-order oligomers rather than existing as a monomer. AI-5 and AI-6, meanwhile, yielded weak chromatograms with broad, low-intensity peaks, and the resulting fractions were too dilute to analyse by SDS-PAGE. These results indicate that problems of aggregation and poor solubility were not limited to AI-2 and AI-3 but were widespread across the binder panel.

Notably, none of the six binders contained cysteine residues, ruling out the possibility of intermolecular disulfide bonds contributing to oligomerisation. The observed aggregation and anomalous SEC behaviour are therefore more likely to be driven by solvent-exposed hydrophobic patches.

4.5. Limitations of RFdiffusion Pipeline

The behaviour of AI-2 and AI-4 highlight a potential limitation of the RFdiffusion pipeline. All of the six *de novo* binders displayed large surface exposed hydrophobic patches at the binding interface. While these patches may help strengthen binder/target interface binding, it also promotes non-ideal behaviour in solution as observed with AI-2 and AI-3.

At present, the RFdiffusion workflow has no parameter to account for solubility or penalise unfavourable surface properties, meaning that many designs have extensive hydrophobic. This was particularly problematic for the small 15 kDa binders, where a single hydrophobic patch represented a disproportionately large fraction of the total surface area and strongly predisposed the proteins to aggregation as observed in AI-1 to AI-6.

A second limitation was epitope convergence. PRODIGY predictions (Figure 9) showed that all six binders targeted the same Tc24 epitope (residues 109–137), overlapping with the known monoclonal antibody (mAb) binding site (residues 43-49). The lack of diversity between the binders was further reinforced by the dendrogram analysis (Figure 6), which revealed binders AI-2, AI-3, AI-4 and AI-6 had high sequence similarity. The lack of epitope and sequence diversity meant the binders were vulnerable to failing in the same way.

4.6. Limitations of this study

Due to time constraints, buffer optimisation trials couldn't be conducted across all six binders. Figure 7 highlighted that AI-1 and AI-2 possessed large positively charged regions which may

have attributed to the aggregation observed during SEC (Figure 11). By increasing the ionic strength of the buffers, the electrostatic charges could have been shieled and such optimisation might have improved protein solubility and reduced aggregation which would have allowed more of the binders to have been tested to see if they bind Tc24.

Additionally, the NeuroBind-designed nanobody expressed in mammalian cells was not successfully recovered. Due to no observable protein expression (Figure 27) it appears that the amount of plasmid DNA used to transfect the cells was too low, and due to time constraints this couldn't be repeated to see if the nanobody and 3CS1 could be successfully expressed in mammalian cultures.

Chapter 5

Conclusion

This project aimed to experimentally validate six RFdiffusion designed binders against Tc24. While all *de novo* binders were successfully expressed in *E. coli*, only AI-2 and AI-3 could be purified as monomeric species and neither demonstrated any measurable interaction with Tc24 by SEC or BLI.

Future work should focus on clarifying the reasons for this lack of binding. Whether it was due to too insufficient concentration of binders with Tc24, whether the binders are self-association or whether they simply don't bind, before they are ruled out as a potential therapeutic.

Addressing these questions will employ the use of different biophysical and structural techniques. SEC-MALS and SEC-SAXS would be useful to determine absolute molecular weight and define the hydrodynamic radius, while NMR and DLS would provide complementary data on oligomerisation state. Molecular dynamics simulations could assess conformational stability of predicted complexes, and crystallography of binders with Tc24 would allow direct comparison of predicted and experimental structures.

However, the most critical test will be functional cell invasion assays to determine whether the binders can inhibit T. cruzi entry. Together, these approaches will provide a clearer framework for advancing current designs and highlight key issues to address in future binder development campaigns.

References

Aldasoro, E. et al., 2018. What to expect and when: benznidazole toxicity in chronic Chagas' disease treatment. *Journal of Antimicrobial Chemotherapy,* 73(4), pp. 1060-1067.

Aricescu, A., Lu, W. & Jones, E., 2006. A time- and cost-efficient system for high-level protein production in mammalian cells. *Acta Crystallographica Section D: Biological Crystallography.,* 62(10), pp. 1243-1250.

Ascanio, L., Carroll, S., Paniz-Mondolfi, A. & Ramírez, J., 2024. In vitro diagnostic methods of Chagas disease in the clinical laboratory: a scoping review. *Frontiers in Microbiology,* Volume 15.

Babicki, S. et al., 2016. Heatmapper: web-enabled heat mapping for all. *Nucleic Acids Research,* Volume 44, pp. 147-153.

Ballesteros-Rodea, G., Martínez Cuevas, T., Jiménez-Ramos, B. & Antonio-Campos, A., 2018. Chagas disease: an overview of diagnosis. *Journal of Microbiology & Experimentation,* 6(3), pp. 151-157.

Bayer HealthCare Pharmaceuticals Inc., 2023. *Lampit (nifurtimox) tablets – Prescribing Information,* s.l.: FDA.

Bern, C., 2011. Antitrypanosomal Therapy for Chronic Chagas' Disease. *New England Journal of Medicine,* 364(26), pp. 2527-2534.

Biomatters, 2025. *Geneious version 2025.2.* [Online]
Available at: https://www.geneious.com

BioRender, 2024. *BioRender – Science Illustration Tool.* [Online]
Available at: https://BioRender.com

Brenière, S., Waleckx, E. & Barnabé, C., 2016. Over six thousand Trypanosoma cruzi strains classified into Discrete Typing Units (DTUs): Attempt at an inventory. *PLOS Neglected Tropical Diseases,* 10(8).

Castro, J. A., Montalto de Mecca, M. & Bartel, L. C., 2006. Toxic Side Effects of Drugs Used to Treat Chagas' Disease (American Trypanosomiasis). *Human & Experimental Toxicology,* Volume 25, pp. 471-479.

Centers for Disease Control and Prevention (CDC), DPDx, 2021. *American Trypanosomiasis (also known as Chagas Disease).* [Online]
Available at: https://www.cdc.gov/dpdx/trypanosomiasisamerican/index.html
[Accessed 09 June 2025].

Chagas, C., 1909. Nova tripanozomiaze humana: Estudos sobre a morfolojia e o ciclo evolutivo do Schizotrypanum cruzi n. gen., n. sp., ajente etiolojico de nova entidade morbida do homem. *Memorias Do Instituo Oswaldo Cruz,* Volume 1, pp. 159-218.

Coura, J. & Dias, J., 2009. Epidemiology, control and surveillance of Chagas disease: 100 years after its discovery. *Memórias do Instituto Oswaldo Cruz,* Volume 104, pp. 31-40.

Dauparas, J., Anishchenko, I. & Baker, D., 2022. Robust deep learning–based protein sequence design using ProteinMPNN. *Science,* 378(6615), pp. 49-56.

DNDi, 2025. *Chagas Disease: Facts.* [Online]
Available at: https://dndi.org/diseases/chagas/facts/
[Accessed 12 May 2025].

Dumonteil, E. & Herrera, C., 2025. Epitope mapping of vaccine antigens Tc24 and TSA1 with antibodies from Trypanosoma cruzi infected patients. *Research Square.*

Edgar, R. C., 2004. MUSCLE: multiple sequence alignment with high accuracy and high throughput. *Nucleic Acids Research,* 32(5), pp. 1792-1797.

Farani, P., Jones, K. & Poveda, C., 2024. Treatments and the Perspectives of Developing a Vaccine for Chagas Disease. *Vaccines,* 12(5), p. 577.

Fox, D. R. et al., 2025. Code to complex: AI-driven de novo binder design. *Structure.*

Inoue, H., Nojima, H. & Okayama, H., 1990. High efficiency transformation of Escherichia coli with plasmids. *Gene,* Volume 96, pp. 23-28.

Jayawardhana, S. et al., 2023. Trypanosoma cruzi persisters that survive benznidazole treatment in vitro and in vivo are in a transient non-replicative state. *bioRxiv.*

Jumper, J. et al., 2021. Highly accurate protein structure prediction with AlphaFold. *Nature,* 596(7873), pp. 583-589.

Keates, T. et al., 2012. Expressing the human proteome for affinity proteomics: optimising expression of soluble protein domains and in vivo biotinylation. *New Biotechnology,* 29(5), pp. 515-525.

Klein, N., Hurwitz, I. & Durvasula, R., 2012. Globalization of Chagas Disease: A Growing Concern in Nonendemic Countries. *Epidemiology Research International.*

Kyte, J. & Doolittle, R. F., 1982. A Simple Method for Displaying the Hydropathic Character of a Protein. *Journal of Molecular Biology,* 157(1), pp. 105-132.

Laboratorios Liconsa, S.A, 2021. *Benznidazole tablets – Prescribing information.* [Online]
Available at: https://dailymed.nlm.nih.gov/dailymed/fda/fdaDrugXsl.cfm?setid=8983d6a0-f63f-4f8e-bba4-38223f39e29b
[Accessed 17 May 2025].

Laranja, F., Dias, E., Nobrega, G. & Miranda, A., 1956. Chagas' disease: A clinical, epidemiologic, and pathologic study. *Circulation,* 14(6), pp. 1035-1060.

Lopez-Albizu, C. et al., 2023. Laboratory diagnosis of Trypanosoma cruzi infection: a narrative review. *Frontiers in Parasitology,* Volume 2.

Medone, P. et al., 2015. The impact of climate change on the geographical distribution of two vectors of Chagas disease: implications for the force of infection. *Philosophical Transactions of the Royal Society,* Volume 370.

Messenger, L. A., Miles, M. A. & Bern, C., 2015. Between a bug and a hard place: Trypanosoma cruzi genetic diversity and the clinical outcomes of Chagas disease. *Expert Review of Anti-infective Therapy,* 13(8), pp. 995-1029.

Morillo, C. A. et al., 2015. Randomized Trial of Benznidazole for Chronic Chagas' Cardiomyopathy. *Randomized Trial of Benznidazole for Chronic Chagas' Cardiomyopathy,* 373(14), pp. 1295-1306.

Pan American Health Organiastion (PAHO), 2025. *Chagas Disease.* [Online]
Available at: https://www.paho.org/en/topics/chagas-disease

Pan American Health Organisation (PAHO), 2023. *The Elimination Initiative: A Platform to Accelerate the Elimination of More Than 30 Communicable Diseases and Related Conditions in the Americas.* [Online]
Available at: https://www.paho.org/en/elimination-initiative
[Accessed 26 May 2025].

Perez-Molina, J. & Molina, I., 2018. Chagas disease. *The Lancet,* 391(10115), p. 82–94.

Ramírez, J. et al., 2010. Chagas cardiomyopathy manifestations and Trypanosoma cruzi genotypes circulating in chronic chagasic patients.. *PLOS Neglected Tropical Diseases,* 4(11).

Rassi, A. J., Rassi, A. & Marin-Neto, J. A., 2010. Chagas disease. *The Lancet,* 375(9723), pp. 1388-1402.

Saitou, N. & Nei, M., 1987. The neighbor-joining method: a new method for reconstructing phylogenetic trees. *Molecular Biology and Evolution,* 4(4), pp. 406-425.

Torrico, F. et al., 2021. New regimens of benznidazole monotherapy and in combination with fosravuconazole for treatment of Chagas disease (BENDITA): a phase 2, double-blind, randomised trial. *The Lancet Infectious Diseases,* 21(8), pp. 1129 - 1140.

Vázquez Torres, S. et al., 2025. De novo designed proteins neutralize lethal snake venom toxins. *Nature,* Volume 639, pp. 225-231.

Versteeg, L. et al., 2021. Location and expression kinetics of Tc24 in different life stages of Trypanosoma cruzi. *PLOS Neglected Tropical Diseases,* 15(9).

Watson, J. et al., 2023. De novo design of protein structure and function with RFdiffusion. *Nature,* 620(7976), pp. 1089-1100.

World Health Organisation (WHO), 2020. *Ending the neglect to attain the sustainable development goals: a road map for neglected tropical diseases 2021-2030,* s.l.: s.n.

World Health Organisation (WHO), 2023. *Chagas disease (American trypanosomiasis). WHO Newsroom Fact Sheets,* s.l.: s.n.

Xue, L. C. et al., 2016. PRODIGY: a web server for predicting the binding affinity of protein–protein complexes. *Structural Bioinformatics,* 32(23), pp. 3676-3678.